

**CONTINUOUS-FLOW ELECTROHYDRAULIC PLASMA DISCHARGE
FOR DEGRADATION OF ORGANIC CONTAMINANTS IN WATER**

A Dissertation

Presented in Partial Fulfillment of the Requirements for the

Degree of Doctor of Philosophy

with a

Major in Environmental Science

in the

College of Graduate Studies

University of Idaho

by

Anilkumar Krosuri

Approved by

Major Professor: Sarah (Xiao) Wu, Ph.D.

Committee Members: Inna Popova, Ph.D.

Krishnan Raja, Ph.D.

You Qiang, Ph.D.

Department Administrator: Lee Vierling, Ph.D.

December 2021

ABSTRACT

The water quality has been deteriorated with the introduction of aromatic organic compounds such as azo dyes and phenolic pollutants due to the poor water management by industries. These pollutants end up into potable water supplies and can pose serious threat to human health even at low concentrations, as conventional wastewater treatment technologies are often incapable of eliminating them from treated water. Therefore, the development of novel and greener oxidation technologies has become a main challenge to degrade a variety of hazardous organic pollutants in wastewater. In this research, a continuous-flow electrohydraulic plasma discharge (EHPD) process and a photocatalyst was developed and evaluated for its potential to treat organic pollutants such as methylene blue (MB) and p-Nitrophenol (p-NP).

In Chapter 2, visible-light driven bismuth oxyiodide modification by carbon-boron nitride quantum dots (BiOI/C-BNQDs) was prepared and characterized as a photocatalyst for degradation and mineralization of p-Nitrophenol. C-BNQDs was synthesized using a microwave process and crosslinked with BiOI using a facile method. The structure, functional bonds, composition and morphology of the catalyst were investigated through series of characterization such as XRD, FTIR, XPS, SEM and TEM, and it was found that the photocatalytic activity of the BiOI/C-BNQDs against the p-NP degradation achieved the highest reaction rate of 0.0173 min^{-1} , which was 2.83 higher than the reaction rate constant of BiOI. From the active species trapping experiment, the reactive $\cdot\text{O}_2^-$ plays the major role followed by holes and hydroxyl radicals in the p-NP degradation. The probable photo degradation mechanism was discussed.

In Chapter 3, the continuous-flow electrohydraulic plasma discharge (EHPD) process characteristic of establishing a stable discharge through the conducting channel in the center orifice of a dielectric plate was developed and investigated to degrade methylene blue (MB) in water. The effect of three operating parameters, i.e., liquid flow rate (37–94 mL/min), air flow rate (1–4 L/min), and initial dye concentration (10–100 mg/L), on the MB degradation efficiency was evaluated. Complete degradation of MB was achieved within 10 min of treatment for all MB concentrations tested. The optimum liquid and air flow rates were 68 mL/min and 3 L/min, respectively, for the EHPD process to remove MB in a circular flow operation. The energy yield for different operating parameters was in the range of between

0.16 g/kWh and 0.81 g/kWh at 50% conversion. Reaction kinetics and the possible MB degradation pathway was analyzed and proposed. Hydroxyl radicals were found to be the dominant reactive species responsible for the MB degradation. Mineralization of MB was demonstrated by a 92.5% COD removal within 10 min treatment for an initial MB concentration of 100 mg/L.

Chapter 4 initiated the optimization and modeling of argon activated EHPD process for efficient removal of p-NP from water. First, the reactor was designed with two dielectric plates to initiate better plasma discharge through the conducting channel in the center orifice. Second, the effects of four operating variables including argon flow rate, pH, applied power and persulfate dosage on the p-NP degradation efficiency and energy yield were investigated to screen the significant factors using a fractional factorial design (FFD). Argon flow rate and applied power were found as significant factors, which were further optimized with response surface methodology (RSM) and the optimal operating condition was found to be 2.73 L/min and 128.6 W for argon flow rate and applied power, respectively. Under the optimal condition, 10-min treatment of 50 mg/L p-NP showed a degradation efficiency of 94.23%, first-order reaction rate constant of 0.2956 min^{-1} and an energy efficiency of 0.22 g/kWh. OES, TOC, radical scavengers, ion chromatography and UPLC-MS/MS were used to investigate and propose the reaction mechanism and pathway for degradation of p-NP on exposure of EHPD.

Coupling the BiOI/C-BNQDs catalyst prepared in Chapter 2 with EHPD process for effective and efficient degradation and mineralization of p-NP was studied in Chapter 5. Under the optimum operating condition determined in Chapter 4, the addition of BiOI/C-BNQDs (3 mL) in EHPD process improved the system in terms of degradation, H_2O_2 concentration, TOC removal and energy yield within 10 min of treatment for 50 mg/L p-NP concentration, as compared to the sole EHPD process. The OES spectra identified $\cdot\text{OH}$, $\cdot\text{O}$, and H as the reactive species involved in the EHPD/BiCBN-3 treatment and radical scavenging experiment confirmed $\cdot\text{OH}$ radicals as the main active species for p-NP degradation. Finally, the synergistic mechanism and degradation pathway of p-NP by EHPD/BiCBN-3 system was proposed.

In summary, the novel continuous-flow EHPD process developed in this research is robust, highly effective, and energy efficient for degradation and mineralization of MB and

p-NP and serves a potential technology that can overcome the limitations of advanced oxidation processes for wastewater treatment. The EHPD or EHPD-catalyst system could also be a promising remediation methodology for emerging contaminants that are recalcitrant to biodegradation and existing advanced oxidation processes.

ACKNOWLEDGMENTS

I would like to first convey my sincere appreciation to my advisor, Dr. Sarah Wu, for all the support and encouragement she has given me. Her extensive interests, guidance, patience and suggestions throughout the Ph.D has helped me acquire and develop the skills and details of independent researcher. She has been and will always be my best source of inspiration.

I own my profound gratitude to all my committee members, Dr. Krishnan Raja, Dr. You Qiang and Dr. Inna Popova for their invaluable help and suggestions, which incited me to broaden my research.

I would like to sincerely acknowledge the assistance of Dr. Lee Deobald for UPLC-MS/MS analysis, Dr. Inna Popova for the Ion Chromatography analysis and Dr. Thomas Williams for XRD and SEM.

To my lab mates, thanks for the fun and support. I wish to sincerely thank Muhammad Aamir Bashir and Robinson Jr for giving continuous support and sharing valuable resources to my research. Without their help, the work might not have come to fruition.

I want to acknowledge Dr. Ilkeun Lee and Dr. Krassimir Bozhilov from University of California Riverside for their input in XPS and HRTEM.

Finally, I would like to thank my parents and my brother for their continuous encouragement and support.

TABLE OF CONTENTS

ABSTRACT.....	II
ACKNOWLEDGMENTS	V
TABLE OF CONTENTS.....	VI
LIST OF FIGURES	IX
LIST OF TABLES	XI
LIST OF ACRONYMS	XII
CHAPTER 1 INTRODUCTION	1
1.1 BACKGROUND AND PROBLEM STATEMENT	1
1.2 LITERATURE REVIEW	3
1.2.1 Photocatalysis.....	3
1.2.2 Role of Nanomaterials in Photocatalysis.....	4
1.2.3 Semiconductor Photocatalysis and its Mechanism.....	5
1.2.4 Boron Nitride	7
1.2.5 Bismuth Oxyiodide	8
1.2.6 Plasma Catalysis.....	8
1.3 RESEARCH OBJECTIVES	13
CHAPTER 2 VISIBLE-LIGHT DRIVEN BISMUTH OXYIODIDE MODIFIED BY CARBON- BORON NITRIDE QUANTUM DOTS (BIOI/C-BNQDs) FOR DEGRADATION AND MINERALIZATION OF P-NITROPHENOL.....	14
2.1 INTRODUCTION	14
2.2 MATERIALS AND METHODS	16
2.2.1 Chemicals.....	16
2.2.2 Synthesis of C-BNQDs	16
2.2.3 Synthesis of Bismuth oxyiodide (BiOI) and BiOI/C-BNQDs.....	16
2.2.4 Characterization of materials.....	17
2.2.5 Photocatalytic activity	18
2.2.6 Sample analysis	19
2.2.7 Radical trapping experiment	19
2.3 RESULTS AND DISCUSSION	19
2.3.1 XRD analysis	19
2.3.2 FTIR spectroscopy	20

2.3.3	XPS analysis.....	21
2.3.4	SEM and TEM analysis.....	26
2.3.5	Photocatalytic Degradation Study	28
2.3.6	Reusability of photocatalyst	31
2.3.7	Radical trapping experiment	32
2.3.8	Possible photocatalytic mechanism.....	33
2.4	CONCLUSIONS.....	34
CHAPTER 3 REMEDIATION OF METHYLENE BLUE BY CONTINUOUS-FLOW		
ELECTROHYDRAULIC PLASMA DISCHARGE..... 35		
3.1	INTRODUCTION	35
3.2	METHODS AND MATERIALS	36
3.2.1	Materials.....	36
3.2.2	Experimental setup.....	37
3.2.3	Experimental design.....	38
3.2.4	Radical scavenging experiments	40
3.2.5	Sample analysis	40
3.3	RESULTS AND DISCUSSION	41
3.3.1	Effects of process operating parameters on the MB degradation	41
3.3.2	Mineralization of MB and water quality change during EHPD process	45
3.3.3	Methylene blue degradation kinetics.....	50
3.3.4	Role of reactive species produced in electrohydraulic plasma for MB degradation	52
3.3.5	Energy yield of the MB degradation by EHPD.....	53
3.3.6	Degradation mechanism of methylene blue by EHPD.....	55
3.4	CONCLUSIONS	58
CHAPTER 4 OPTIMIZATION AND MODELING OF ARGON ACTIVATED		
ELECTROHYDRAULIC PLASMA DISCHARGE PROCESS FOR P-NITROPHENOL		
DEGRADATION 60		
4.1	INTRODUCTION	60
4.2	METHODS AND MATERIALS	61
4.2.1	Materials.....	61
4.2.2	Experimental setup.....	61
4.2.3	Design of Experiments (DOE)	63
4.2.4	Experimental procedure	63
4.2.5	Radical scavenging experiments	65

4.2.6	Analytical methods.....	65
4.3	RESULTS AND DISCUSSION	66
4.3.1	2 ⁴⁻¹ fractional factorial design.....	66
4.3.2	Central composite design	71
4.3.3	Degradation efficiency and Energy yield model.....	73
4.3.4	Graphical interpretation and optimization of operating parameters	77
4.3.5	Emission spectra of EHPD process	80
4.3.6	Effects of initial concentration	81
4.3.7	Radical scavenging experiment.....	83
4.3.8	TOC removal, Energy yield, pH and conductivity change.....	86
4.3.9	UPLC-MS/MS and Ion chromatography analysis.....	88
4.4	CONCLUSIONS.....	90
CHAPTER 5 BIOI/C-BNQDs CATALYST ASSISTED ELECTROHYDRAULIC PLASMA DISCHARGE PROCESS FOR P-NITROPHENOL DEGRADATION.....		92
5.1	INTRODUCTION	92
5.2	MATERIALS AND METHODS	94
5.2.1	Chemicals.....	94
5.2.2	Synthesis of C-BNQDs	95
5.2.3	Synthesis of Bismuth oxyiodide (BiOI) and BiOI/C-BNQDs nanocomposites	95
5.2.4	Experimental set up.....	95
5.2.5	Experimental procedures.....	97
5.2.6	Radical scavenging experiments	98
5.2.7	Analytical methods.....	99
5.3	RESULTS AND DISCUSSION.....	99
5.3.1	Effect of various catalysts in EHPD system.....	99
5.3.2	Effect of catalyst dosage	102
5.3.3	Effect of initial p-NP concentration in EHPD-catalysis system.....	104
5.3.4	Energy yield, TOC, pH, conductivity and H ₂ O ₂	106
5.3.5	Role of reactive species produced in EHPD/BiCBN-3 system	108
5.3.6	Synergistic effects of EHPD/BiCBN-3 system	110
5.3.7	Degradation pathway of p-NP using EHPD/BiCBN-3 system	111
5.4	CONCLUSIONS.....	114
CHAPTER 6 SUMMARY AND FUTURE PERSPECTIVES		116

LIST OF FIGURES

Figure 1.1. Nanoarchitecture A: composition of functional sites B: ordering level of sites; C: functional properties of material	5
Figure 1.2. Mechanism of semiconductor photocatalysis	6
Figure 2.1. Recirculating photoreactor.....	18
Figure 2.2. XRD patterns of C-BNQDs, BiOI and BiOI/C-BNQDsX (X= 1, 3 and 5 mL).....	20
Figure 2.3. FTIR spectra of C-BNQDs, BiOI and BiOI/C-BNQDsX (X= 1, 3 and 5 mL).....	21
Figure 2.4. (a) XPS Survey of C-BNQDs and BiOI/C-BNQDs (3 mL); (b) Bi 4f; (c) O 1s; (d) I 3d; (e) C 1s; (f) B 1s; and (g) N 1s.....	26
Figure 2.5. (a, b) SEM images of BiOI; (c, d) HRTEM images of C-BNQDs; (e, f) TEM images of BiOI/C-BNQDs (3 mL); (g) HRTEM image of BiOI/C-BNQDs (3 mL).....	28
Figure 2.6. Degradation efficiency of BiOI and BiOI/C-BNQDsX (X=1, 3 and 5 mL).....	29
Figure 2.7. First order kinetics for p-NP degradation by BiOI and BiOI/C-BNQDsX (X= 1, 3 and 5 mL).....	30
Figure 2.8. TOC removal efficiency for p-NP degradation by BiOI/C- BNQDs (3 mL)	31
Figure 2.9. Reusability of BiOI/C- BNQDs (3 mL) for the degradation of p-NP.....	32
Figure 2.10. Photodegradation efficiencies of p-NP with different quenchers	33
Figure 3.1. Schematic of the novel electrohydraulic discharge reactor system; $\delta = 3.2$ mm, $\varphi = 0.8$ mm..	38
Figure 3.2. Degradation efficiency of MB (20 mg/L) using plasma at different liquid flow rates	42
Figure 3.3. Degradation efficiency of MB (20 mg/L) by EHPD at different air flow rates.....	44
Figure 3.4. Degradation efficiency by EHPD at different initial concentrations under 68 mL/min and 3 L/min.....	45
Figure 3.5. Changes of COD, H ₂ O ₂ and inorganic ions during 10 min EHPD treatment time (liquid flow rate = 68 ml/min, and air flowrate = 3 L/min)	48
Figure 3.6. Final pH and conductivity at (a) different liquid flow rates; (b) different air flow rates; and (c) different initial MB concentrations after 10-minute treatment	49
Figure 3.7. First order kinetics of MB degradation (a) at different liquid flow rates; (b) at different air flow rates; and (c) at different initial MB concentrations	52
Figure 3.8. Role of active species by EHPD at 20 mg/L MB initial concentration under 68 ml/min and 3 L/min.....	53
Figure 3.9. Total ion chromatogram (TIC) of MB degradation at different treatment times ($C_0 = 20$ mg/L, liquid flow rate = 68 ml/min, and air flowrate = 3 L/min).....	56
Figure 3.10. Degradation pathway of MB molecule.....	58
Figure 4.1. Schematic of the novel electrohydraulic discharge reactor system; $\delta = 3.2$ mm, $\varphi = 0.8$ mm...	63
Figure 4.2. Pareto charts of the standardized effects based on (a) response degradation efficiency and (b) based on energy yield (Minitab)	69

Figure 4.3. FFE predicted values vs actual values of (a) degradation efficiency and (b) energy yield.....	70
Figure 4.4. Four main effects plots for (a) degradation efficiency and (b) energy yield	71
Figure 4.5. CCD predicted values vs actual values of (a) degradation efficiency and (b) energy yield	75
Figure 4.6. Normality plots for the regression model (a) degradation efficiency and (b) energy yield	76
Figure 4.7. Contour plots of (a) degradation efficiency and (b) energy yield.....	78
Figure 4.8. Surface plots of (a) degradation efficiency and (b) energy yield.....	79
Figure 4.9. Optimization of EHPD process	80
Figure 4.10. Optical emission spectra of argon activated EHPD process.....	81
Figure 4.11. Degradation efficiency of different initial concentrations of p-NP by EHPD.....	82
Figure 4.12. First order kinetics of different initial concentrations of p-NP degradation.....	83
Figure 4.13. Radical scavenging experiment of EHPD process for p-NP degradation (50 mg/L).....	85
Figure 4.14. H ₂ O ₂ concentration of EHPD process for p-NP degradation (50 mg/L).....	85
Figure 4.15. pH and conductivity for EHPD process at different initial p-NP concentration.....	88
Figure 4.16. Total ion chromatogram (TIC) of p-NP degradation intermediates	89
Figure 4.17. Degradation pathway of p-NP by EHPD.....	90
Figure 5.1. Schematic of the electrohydraulic discharge reactor system	96
Figure 5.2. (a) Degradation efficiency of p-NP with BiOI and BiOI/C-BNQDsX (X =1, 3 and 5 mL) catalysts in EHPD system, (b) First order kinetics of p-NP degradation with BiOI and BiOI/C-BNQDsX (X =1, 3 and 5 mL) catalysts in EHPD system	101
Figure 5.3. (a) Degradation efficiency of p-NP with different catalyst dosage of BiOI/C-BNQDs (3 mL) in EHPD system, (b) First order kinetics of BiOI/C-BNQDs (3 mL) catalyst dosage in EHPD system	103
Figure 5.4. (a) Effect of initial p-NP concentrations degradation in EHPD/BiCBN-3 system, (b) First order kinetics of initial p-NP concentrations degradation in EHPD/BiCBN-3 system	105
Figure 5.5. pH and conductivity for EHPD/BiCBN-3 system at different initial p-NP concentrations.....	107
Figure 5.6. H ₂ O ₂ concentration in EHPD/BiCBN-3 system at 50 mg/L p-NP concentration.....	108
Figure 5.7. OES spectra of EHPD/BiCBN-3 system	109
Figure 5.8. Role of active species by EHPD/BiCBN-3 at 50 mg/L p-NP initial concentration under 2.73 L/min and 128.6 W	110
Figure 5.9. (a) Total ion chromatogram (TIC) of initial p-NP concentration 50 mg/L and (b) p-NP after 10 min treatment in EHPD/BiCBN-3 system.	113
Figure 5.10. Degradation pathway of EHPD/BiCBN-3 system.....	114

LIST OF TABLES

Table 1.1. Synergetic effects of plasma catalysis	9
Table 1.2. Comparison of homogeneous and heterogeneous catalysts assisted plasma processes with plasma alone for degradation of pollutants	11
Table 2.1. Relative atomic surface compositions (%) of C-BNQDs and BiOI/C-BNQDs (3 mL).....	22
Table 2.2. Rate constant (K) and R squared values of photocatalytic degradation study.	30
Table 3.1. First order kinetic constant of MB degradation at different operational parameters.....	50
Table 3.2. Energy yield at 50% MB degradation for different operational parameters of EHPD system....	54
Table 3.3. Comparison of the novel EHPD on MB degradation with other nonthermal plasma processes.	54
Table 4.1. The 2^{4-1} fractional factorial experimental design matrix with responses.....	67
Table 4.2. Analysis of variance for the factorial model	68
Table 4.3. Central composite design matrix of the two independent variables in real units with experimental responses for degradation efficiency (%) and energy yield (g/kWh).....	72
Table 4.4. ANOVA for quadratic model of degradation efficiency and energy yield	74
Table 4.5. First order kinetic constant for degradation of p-NP at different initial concentrations.....	83
Table 4.6. Comparison of the Argon activated EHPD on p-NP degradation with other plasma processes.	87

LIST OF ACRONYMS

EHPD: Electrohydraulic plasma discharge
CFEHPD: Continuous-flow electrohydraulic plasma discharge
MB: Methylene blue
p-NP: p-Nitrophenol
BiOI: Bismuth oxyiodide
BN: Boron nitride
BNQDs: Boron nitride quantum dots
C-BNQDs: Carbon-boron nitride quantum dots
XRD: X-ray diffraction
FTIR: Fourier transform infrared spectroscopy
XPS: X-ray photoelectron spectroscopy
SEM: Scanning electron microscopy
TEM: Transmission electron microscopy
COD: Chemical oxygen demand
FFD: Fractional factorial design
RSM: Response surface methodology
CCD: Central composite design
OES: Optical emission spectroscopy
TOC: Total organic carbon
UPLC-MS/MS: Liquid chromatography- mass spectrometry
IC: Ion chromatography
H₂O₂: Hydrogen peroxide
AFFF: Aqueous film forming foams
O₃: Ozone
·O₂⁻: Superoxide anion
·OH: Hydroxyl radical
AOPs: Advanced oxidation processes
DBD: Dielectric barrier discharge
MO: Methyl orange
RB: Rhodamine-B
PCB77: 3,3',4,4'- tetrachlorobiphenyl
He-DBD: Helium dielectric barrier discharge
O₂- DBD: Oxygen dielectric barrier discharge
SPD: Self-pulsing streamer discharge

PFOA: Perfluorooctanoic acid
p-CH₃: p-methyl phenol
PFAS: Per- and polyfluoroalkyl substances
e⁻/h⁺: Electron-hole pair
e⁻: Electrons
h⁺: Holes
UV-vis: Ultraviolet-visible
CO₂: Carbon dioxide
hν: Photon
TiO₂: Titanium dioxide
eV- Electron volt
h-BN: Hexagonal boron nitride
CR: Congo red
BY: Basic yellow 1
Cu: Copper
BNO: Oxygen rich mesoporous boron nitride
NaBH₄: Sodium borohydride
ZnO: Zinc oxide
BiOX: Bismuth oxyhalides
BiOCl: Bismuth oxychloride
BiOBr: Bismuth oxybromide
BiOF: Bismuth oxyfluoride
CeO₂: Cerium oxide
Fe₂O₃: Ferric oxide
ZrO₂: Zirconium oxide
g-C₃N₄: Graphitic carbon nitride
Fe²⁺: Ferrous ion
rGO: Reduced graphene oxide
PS: Persulfate
Ar: Argon
N₂: Nitrogen
GAD: Gliding arc discharge
UPCN: Ultrathin porous graphitic carbon nitride
SMZ- Sulfamethazine
Bi (NO₃)₃. 5H₂O: Bismuth nitrate pentahydrate

KI: Potassium iodide

HNO₃: Nitric acid

KOH: Potassium hydroxide

AO: Ammonium oxalate

IPA: Isopropanol

AA: Ascorbic acid

NTP: Non-thermal plasma

e⁻_{aq}: aqueous electron

TIC: Total ion chromatogram

NaNO₃: Sodium nitrate

PDPTC- Pulsed discharge plasma-TiO₂ catalytic technique

CB-Conduction band

VB-Valence Band

BiCBN-3: BiOI/C-BNQDs (3 mL)

CHAPTER 1 INTRODUCTION

1.1 Background and Problem Statement

In recent years, the sources of clean water have been deteriorated worldwide. The only possible way is to treat and reuse the wastewater from a variety of sources. However, this reclaimed water has been contaminated by a wide range of environmental pollutants due to rapid growth in industrialization. Today, industrial wastewater poses a potential threat to the entire natural water system. Industrial effluents contain complex chemicals including organic and inorganic compounds from textile dyes, pharmaceuticals, food packaging, surfactants, aqueous film forming foams (AFFF), metal plating, electronics, semiconductors, cosmetics, petrochemicals, oil/mining, and pesticides [1-6]. A major class of these hazardous chemicals in wastewater is aromatic organic compounds such as azo dyes and phenolic substances [7, 8]. These azo dye residues and phenolic pollutants are highly persistent and resistant to breakdown and can easily accumulate over time in the environment, most of which are highly toxic even at low concentrations [9, 10].

Wastewater containing azo dyes poses a serious threat to the natural environment and humans due to their color and potential toxicity [11]. For instance, due to the organic nature and toxicity, it is the source for the eutrophication and aesthetic pollution in the aquatic environment [12, 13]. Among the azo dyes, methylene blue (MB) is a heterocyclic cationic dye that has wide industrial applications such as in textiles, pharmaceuticals, and personal care products. MB is highly toxic, potential carcinogenic and can degrade to form harmful by-products, which can be easily accumulated and difficult to degrade in the environment [14, 15]. Among the phenolic substances, p-Nitrophenol (p-NP/4-NP) is identified as the most common toxic organic pollutant from industrial wastewater. p-NP is widely used in the production of chemical intermediates, explosives, pharmaceuticals, fungicides, insecticides, synthetic dyes and pesticides [16, 17]. Due to its wide applications, p-NP is easily accumulated into air, soil, and groundwater interfaces and can be easily transported to the surface waters. Even at low concentrations, p-NP is highly toxic and can lead to serious health effects such as methemoglobin, respiratory tract, liver and kidney damage [18, 19]. This stable and water soluble compound poses serious threat to humans and the ecological system, which thus has been classified as “Priority Pollutants” by the U. S. Environmental Protection Agency (U.S. EPA) [20].

Currently, the wastewater treatment plants remain a challenge for these compounds as it cannot be removed by conventional treatments. And the effluent may have an increasing concentration of MB and p-NP than the influent because they can transform into undesired by-products, which cannot be further biodegradable. Multiple conventional methodologies such as adsorption, biological degradation, electro-coagulation and nano-filtration have been used for the treatment of wastewater, containing MB and p-NP [21, 22]. However, these techniques prove to be ineffective due to the organic loaded adsorbents and incomplete mineralization to form simple inorganic compounds [23, 24]. Advanced oxidation processes (AOPs) such as UV/H₂O₂, Fenton reaction, zero-valent iron, sonolysis, photochemical, photocatalysis and electrochemical oxidation seem to be very effective for the removal of organic pollutants [25-29]. However, the results associated with these techniques suffer from a few limitations such as longer degradation time, slower mineralization, and lack of knowledge on the potential degradation products. Therefore, it is necessary to develop novel water treatment technologies for the complete removal of organic pollutants in water.

Recently, non-thermal plasma-based technologies has gained attention for the treatment of toxic organic compounds in water. Similar to AOPs, this method makes use of highly reactive species (O₃, H₂O₂, [•]O, [•]OH), UV irradiation, and shockwaves, etc., without any chemical inputs to degrade organic pollutants in water [30-37]. Different types of reactor configurations such as dielectric barrier discharge (DBD), corona discharge, pulsed discharge, gliding arc discharge, jet plasma, microwave discharge and radio frequency plasma can be used to generate non-thermal plasma discharge [38]. For instance, A.S. Bansode et al. [39] reported atmospheric nonthermal plasma torch with helium-air feed gas for the decomposition of the methylene blue (MB), methyl orange (MO) and rhodamine-B (RB) in water. It took 10 min for the complete degradation of an initial conc. of 10⁻⁴M for all the organic pollutants. Huang. Q., and Fang. C. [40] employed a helium, air and oxygen non-thermal dielectric barrier discharge to degrade 3,3',4,4'-tetrachlorobiphenyl (PCB77) in aqueous solution. Compared to all working gases, He-DBD showed highest degradation efficiency of 80% for PCB77 within 2 min of treatment, followed by O₂-DBD (75%) and Air-DBD (70%). They found that hydroxyl radical plays the dominant role in the PCB77 degradation with He-DBD and plasma-produced ozone contribution to the removal of PCB77 with O₂-DBD. In another recent study reported by Saleem et al. [42], three plasma reactors

were investigated. The reactor with a pin-to-ring self-pulsing streamer discharge (SPD) over the liquid surface outperformed the other two, one using a wires-to-plate DC- corona discharge, the other producing plasma in gas bubbles through the application of an AC streamer discharge. The best results were obtained using argon for plasma inception and perfluorooctanoic acid (PFOA) solutions in tap water: the energy yield and fluoride recovery were 561 mg/kWh and 47%, respectively. J. Wang et al. [41] achieved a complete p-methyl phenol (p-CH₃) degradation within 32 min and the highest energy yield was about 3.5 g/kWh using a dielectric barrier discharge plasma reactor with water flowing like a waterfall. The efficiency of this type of technology primary depends upon the design of the plasma reactor and operational parameters. Even though non-thermal plasma has shown great potential in wastewater treatment, there is always a comparison between the energy and conversion efficiency in plasma-alone process. So, in order to further improve the degradation efficiency while maintaining high-energy efficiency, a hybrid, combination of plasma with a photocatalyst can be a great and promising approach.

1.2 Literature Review

1.2.1 Photocatalysis

Photocatalysis is a part of AOPs and has been the focus of environmental catalysis community due to its utilization of solar energy in addressing problems related to the environment. Integration of photocatalysis with plasma would be great and promising technique to achieve high-rate degradation and mineralization of organic pollutants. In recent years, the development of novel photocatalytic materials and technologies has addressed many environmental issues such as degradation of air and water pollutants, soil remediation, biomass valorization and hydrogen production, etc..[42]. In general, photocatalysis is described as the acceleration of chemical reactions irradiated by an UV-visible light source in presence of a photocatalyst. The main difference between a thermal and photocatalysis is, catalyst is activated by photons rather than by heat [43, 44].

Photocatalysis can either be homogeneous or heterogeneous photocatalytic processes. In the homogeneous photocatalytic process, reactants and catalysts exists in the same phase, the process takes place in bulk solution and various oxidants such as H₂O₂, O₃, Fenton reagents and many others are used in the presence of strong UV light to degrade the polluted

water. Whereas, in the heterogeneous process, reactions occur on the surface of a semiconductor material by means of an electron-hole pair (e^-/h^+) generation by a suitable light source. In comparison, heterogeneous photocatalysts are easy to recover and recycle than homogeneous photocatalysts. But they suffer from few limitations like mass transfer problems [45-47].

1.2.2 Role of Nanomaterials in Photocatalysis

With the development of nanotechnology, nanomaterials have emerged as a field with intriguing properties to improve photocatalytic efficiencies, where reduction in particle size results in high surface area and possibly quantum size effects. Nanocatalysts benefit photocatalytic processes with high stability, high selectivity, and efficiency, and with easy recovery and recyclability. Properties like specific reactivity can also be expected due to the nanoscale, which cannot be achieved with non-nano/regular materials [48, 49]. At nanoscale, thermodynamic laws of macroscopic level no longer apply, the high surface area-to-volume ratio will impact the thermodynamic behavior of the nanomaterials. In addition, atomic interaction at the surface of nanomaterials will be different from that of bulk materials. It helps in bringing the difference in the mechanical properties of nanomaterials compared to the bulk [50-52].

Moreover, nanoscale effects can not only change the physical properties but also the chemical properties. In fact, catalytic activity at nanoscale is influenced by the polarization changes in the bond to the adsorbate and the surface reactivity is highly size dependent. Moreover, the quantum size effects help enhance catalytic activity in nanomaterials. In metal or semiconductor nanomaterials electrons are delocalized extensively, then electron states combine to extended band structure. Here the particles become pseudo-atoms and the electron states are quantized, which helps in improving the electron affinities of nanomaterials compared to bulk and micro level [49, 52].

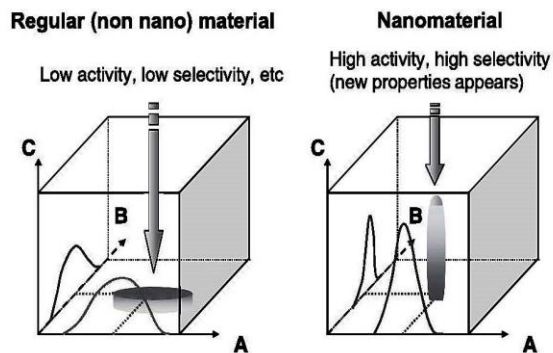


Figure 1.1. Nanoarchitecture A: composition of functional sites B: ordering level of sites; C: functional properties of material [49]

1.2.3 Semiconductor Photocatalysis and its Mechanism

In heterogenous photocatalysis, semiconductor materials are used for degrading refractory organic pollutants and mineralized them to CO_2 and water. Semiconductor materials have a unique electronic structure with a filled valence band and an empty conduction band, which make them capable of acting as photosensitizers for redox reactions. In general, a catalyst is activated by light, when a photon of energy ($h\nu$) equal to or greater than that of bandgap occurs. This makes electrons (e^-) move from the valence band into the conduction band, leaving behind the holes (h^+). These excited electron-holes can recombine and release energy as heat, which is not favorable and leads to an inefficient photocatalyst. So, the main objective of the process is to make excited electrons and holes to react with oxidants and reductants at the semiconductor surface to generate hydroxyl radical ($\cdot\text{OH}$) and other reactive radicals/species [53-55]. The advantages of heterogeneous photocatalysis include low operating costs, temperature, and complete mineralization of pollutants and their intermediates without any secondary by-products [56, 57].

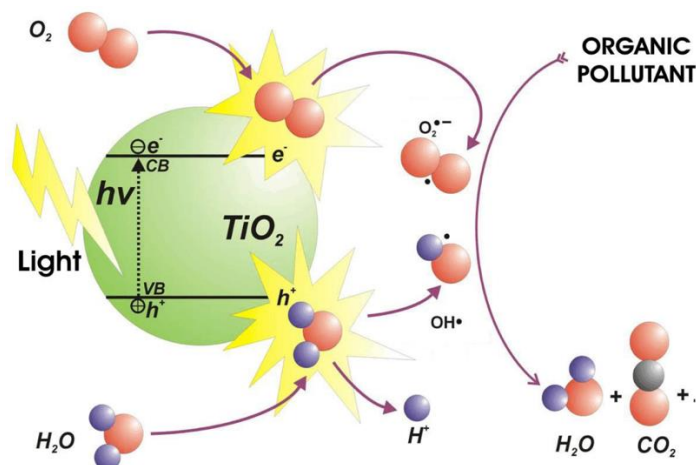


Figure 1.2. Mechanism of semiconductor photocatalysis [58]

For instance, titanium dioxide (TiO₂) have been widely studied semiconductor photocatalyst due to their high stability, high photocatalytic activity, low cost, non-toxicity and high chemical inertness [59]. They are excellent semiconductor materials used in variety of applications, including catalysis, energy conversion, environmental remediation, photochemical storage, cosmetics, biomedical diagnosis and therapy and antireflection coating [60, 61]. However, the application of TiO₂ is limited by its UV activation requirement. The major shortcoming of the pure nano-TiO₂ crystal is the utilization of visible light. The TiO₂ wide band gap energy ($\sim 3\text{--}3.2$ eV) limits harvesting of solar energy in the visible wavelength region [59]. To better utilize the solar energy and eliminate new emerging contaminants from water, the development of novel catalysts with visible light response are much needed [62].

Over the years, many semiconductor nanomaterials have been developed for photocatalysis. However, it proved to be inefficient as the single photocatalyst has the problem of rapid combination of electrons and holes occurring before migrating to the surface. In order to prevent the recombination of electron-hole pairs, combining two different semiconductor materials will be a promising approach as it has several benefits such as 1) new established p–n junction generated heterostructures, 2) extensive light absorption range, 3) increase in the rate of charge transfer and 4) enhanced individual redox potentials [63].

1.2.4 Boron Nitride

A new nanomaterial has emerged recently called boron nitride (BN), an analog of graphene. This material has distinctive structures and properties like wider band gap (5.5-5.9 eV), high surface area and high thermal conductivity (600W/m/k). These unique properties have attracted them to many applications like photocatalysis, optoelectronics, Li-ion batteries, sensors, and many others. Hexagonal boron nitride (h-BN) has lattice parameters similar to that of graphene structure. Each layer is composed of equal number of boron and nitrogen atoms arranged alternatively in a plane dimension to form SP^2 hybrid form linked by strong covalent bond and van der Waals heterojunctions existing between the layers [64-66]. Lei et al. [67] investigated the porous BN nanosheets for the removal of congo red (CR), methylene blue (MB) and basic yellow 1 (BY) dyes. BN nanosheets showed much higher sorption capacity for CR (782 mg/g) than BY (556 mg/g) and MB (313 mg/g). Duan et al. [64] reported boron nitride for degradation of PFOA and GenX. Besides having a large band gap, BN was able to degrade PFOA photocatalytically via hole-initiated reaction pathway. 100% degradation was achieved within 240 min for 50 mg/L PFOA initial concentration and 52% of total initial fluorine was released. BN degradation rate was 4 times more active than TiO_2 and was reused for three cycles without decrease in activity. Many researchers reported BN based composite can achieve high photocatalytic activity compared to single photocatalytic due to their surface properties. Jiang. X et al. [68], reported Cu nanoparticles supported on oxygen-rich mesoporous boron nitride (BNO) using an adsorption-reduction technique for the reduction of p-NP in the presence of $NaBH_4$. Cu/BNO catalyst showed excellent catalytic activity of p-NP reduction with the reaction rate constant of 0.692 min^{-1} and the catalyst efficiency was undamaged within five cycles. Fu et al. [69] reported that introduction of ZnO with BN showed improved ZnO photocatalytic reduction ability. Sheng et al. [70] reported h-BN/ TiO_2 photocatalyst showed excellent degradation efficiency with decrease in recombination efficiency and increase charge transfer rates for methylene blue and rhodamine-B respectively.

Moreover, the composite photocatalyst were stable and recyclable. The combination of BN can reduce the recombination rate of electron/hole pairs [66, 70-73]. In particular, reducing the size of boron nitride to the quantum dots can attract separation of photogenerated electron/hole pairs more effectively because of the negatively charged

oxygen groups present on the boron nitride quantum dots (BNQDs) [74]. Thus, the integration of BNQDs into nanocomposite could be a potential photocatalyst with enhanced visible light-responsive performance for degradation of organic pollutants. Moreover, BNQDs have excellent chemical stability, biocompatibility, dispersibility and fluorescence properties, favorable in applications such as bioimaging, fluorescence sensing and photocatalysis [75, 76].

1.2.5 Bismuth Oxyiodide

Among the considerations for making a heterostructure composite, ternary oxide semiconductor; bismuth oxyhalides (BiOX) such as BiOCl, BiOBr, BiOF and BiOI would be promising choices as it has shown enhanced photocatalytic activities compared to TiO₂. These materials have unique layered structure, high stability, indirect transition band gap characteristics and strong absorption in visible light region [77]. A layer structured of bismuth oxyhalides consists of [Bi₂O₂]²⁺ sheets inserted with double halogen atom plates, which empower them with excellent photocatalytic activities. Having negatively charged halide layer and positively charged [Bi₂O₂]²⁺ layer makes the BiOX anisotropic [78, 79].

Moreover, the indirect transition band gap makes the excited electrons move to the valence band with the help of phonons, extending the lifetime of the electron-hole pairs and enhancing the photocatalytic activity [80]. The photogenerated holes on the surface of bismuth-contained photocatalysts under visible light cannot react with water to form [•]OH radicals because of the standard redox potential of Bi⁵⁺/Bi³⁺ (1.59 eV) is lower than the [•]OH/OH⁻ (1.99 eV). Thus, it promotes valence band potential, accumulation of large number of holes [81]. Compared to BiOCl, BiOF and BiOBr, BiOI can show higher photocatalytic activity for the degradation of organic pollutants due to low band gap energy of 1.8 eV and wider absorption in the visible light region [78, 82]. More interestingly, BiOI could be a good choice for making hybrids with BN in achieving a high-performance photocatalytic activity for MB and p-NP degradation. Also, there are no reports of using BiOI/BN nanocomposites for p-NP removal in aqueous solution.

1.2.6 Plasma Catalysis

Plasma-catalysis is currently one of the rapidly growing multidisciplinary branches that holds great potential to improve the existing catalytic technologies for many applications

including wastewater treatment [83-85]. Plasma-catalysis is also referred as plasma-assisted catalysis or plasma-enhanced catalysis. The aim of this process is to improve the catalytic reactions by combining plasma to the reaction cycle. In particular, non-thermal plasma has proven to be effective for the catalysts to run at low temperatures. This is due to the energetic electrons that can produce a wider variety of reactive species such as free radicals, excited state ions, molecules and other species, which are not possible at thermal equilibrium at ambient temperatures. Besides that, can produce UV-vis irradiation, shock waves. These electrons have a typical energy of 1-10 eV, which is enough to break chemical bonds [86].

The plasma-catalytic combination is expected to have many synergistic advantages, can minimize the unwanted by-products and improve the yield, selectivity, carbon balance and energy efficiency [87]. Table 1.1 shows the synergetic effects of plasma catalysis. To overcome the shortcomings of photocatalysis, combining the non-thermal plasma and photocatalysis would be good choice to enhance degradation and mineralization of organic pollutants and improve the sustainability of the process.

Table 1.1. Synergetic effects of plasma catalysis [38]

Influence of catalyst on plasma	Influence of plasma on catalyst
Enhancement of electric field	Higher adsorption and desorption of catalyst
Microdischarges generation	Change in catalyst oxidation state
Change in the distribution of active species	Hotspot formation
Adsorption of reactants	Higher catalyst surface area
	Metal oxide catalysts reduction into their metallic form
	Formation of excited species and radicals, change in surface pathways
	Lowering the activation energy barrier
	Increasing the selectivity
	Photocatalyst effect

In general, plasma-catalytic set up can be distinguished in two main ways. 1) Single-stage plasma catalysis configuration, where catalyst is positioned directly inside the plasma discharge region, or the catalyst is added directly into the aqueous solution and passed through plasma discharge. 2) Two-stage plasma catalysis configuration, where catalyst and plasma are physically separated, either upstream or downstream.

The main difference between the single-stage and two-stage process is the variety of species that the catalyst interacts. In single stage, the catalyst interacts with short-lived species such as ions, excited radicals, photons and electrons. Whereas in two-stage, the catalyst will interact with long-lived intermediates or radicals, neutrals and end products [88]. The catalyst can be introduced into the discharge region in the form fine powder, pellets, electrode materials, honeycomb monolith, foam or electrode coating on the reactor wall or packed bed [85]. The ease of introducing catalyst is based on the reactor type used. It is easy to add the catalyst in a dielectric barrier discharge because it has simple geometry and operation to room temperature. Where in other types of reactors like microwave or gliding arc, the catalyst is implemented downstream due to high gas temperature [89]. Table 1.2 shows the comparison of homogeneous and heterogeneous catalysts assisted plasma processes with plasma alone for degradation of pollutants.

Table 1.2. Comparison of homogeneous and heterogeneous catalysts assisted plasma processes with plasma alone for degradation of pollutants

Plasma Reactor	Catalyst	Pollutant	Feed gas (L/min)	Initial concentration (C ₀ , mg/L)	Degradation (%) and Energy yield (g/kWh)	Reference
Cylindrical tube DBD, quartz dielectric (18 kV)	No catalyst	Phenol	Air (0.2 L/min)	100 mg/L	59.55% (30 min), 6.03	[90]
	CeO ₂ (100 mg/L)	Phenol	Air (0.2 L/min)	100 mg/L	72.9% (30 min), 8.05	
	Fe ₂ O ₃ /CeO ₂ (100 mg/L)	Phenol	Air (0.2 L/min)	100 mg/L	84.49% (30 min), 9.25	
	ZrO ₂ /CeO ₂ (100 mg/L)	Phenol	Air (0.2 L/min)	100 mg/L	91.48% (30 min), 10.03	
DBD (17 kV)	No catalyst	p-NP	-	5 mg/L	34.8% (50 min), 0.0994	[91]
	Fe ²⁺ (36 μM)	p-NP	-	5 mg/L	69.6% (50 min), 0.197	
	Persulfate (PS, 2.5 mM)	p-NP	-	5 mg/L	63.6% (50 min), 0.180	
	PS/Fe ²⁺	p-NP	-	5 mg/L	81.1%, (50 min), 0.229	
Needle to needle alternate current corona (45.91 W, pH= 3.5)	No catalyst	Methylene blue	O ₂	20 mg/L	96% (40 min), 0.063	[92]
	Pyrite (0.13 g/L)	Methylene blue	O ₂	20 mg/L	95% (10 min), 0.25	
DBD and DBD with gas bubbling system (5 kV)	No catalyst	Bisphenol A	-	20 mg/L	68.4% (40 min)	[93]
	Nano-ZnO (50 mg/L)	Bisphenol A	-	20 mg/L	85.4% (40 min)	
	Nano-ZnO (50 mg/L)	Bisphenol A	O ₂ (0.5 L/Min)	20 mg/L	100% (20 min)	

DBD (20 W, pH=10)	No catalyst	Acid Orange7	Air (0.014 L/min)	5 mg/L	61 % (12 min)	[94]
	g-C ₃ N ₄ /TiO ₂ (0.5 g/L)	Acid Orange 7	Air (0.014 L/min)	5 mg/L	100% (12 min)	
DBD (12 kV)	No catalyst	Acid Orange 7	Air (0.18 NL/min)	20 mg/L	14 % (30 min)	[95]
	Fe ₂ O ₃ immobilized on glass spheres (36 g)	Acid Orange 7	Air (0.18 NL/min)	20 mg/L	80% (5 min)	
DBD (20W, pH=7)	No catalyst	Methyl paraben	Air (0.33 L/min)	20 mg/L	55 % (15 min)	[96]
	ZnO-rGO nanosheets (0.015 g/L)	Methyl paraben	Air (0.33 L/min)	20 mg/L	99% (15 min), 7.98	
Atmospheric pressure plasma jet (32 kV)	No Catalyst	Reactive red-198	Ar (9 L/min)	10 ⁻⁴ M	52 % (10 min)	[97]
	Cu-doped TiO ₂ (20 mg/L)	Reactive red-198	Ar (9 L/min)	10 ⁻⁴ M	76% (10 min)	
	Ar plasma pretreated Cu-doped TiO ₂ (20 mg/L)	Reactive red-198	Ar (9 L/min)	10 ⁻⁴ M	85% (10 min)	
	N ₂ plasma pretreated Cu-doped TiO ₂ (20 mg/L)	Reactive red-198	Ar (9 L/min)	10 ⁻⁴ M	96% (10 min)	
Gliding arc discharge (GAD) (10 kV, pH=3)	No catalyst	Orange G	Air (13.3 NL/min)	23 mg/L	17 % (60 min)	[98]
	Laterite soil (3 g/L)	Orange G	Air (13.3 NL/min)	23 mg/L	100% (60 min)	

1.3 Research Objectives

Based on the literature review, the research objectives for this thesis will include:

1. Preparation of carbon-boron nitride quantum dots modified bismuth oxyiodide composites (BiOI/C-BNQDs) with high visible activity and apply to p-Nitrophenol (p-NP) remediation by photodegradation.
2. Remediate methylene blue for highly efficient degradation and mineralization by CFEHPD and explore the mechanism of rapid oxidation and the degradation pathway by CFEHPD.
3. Remediate p-NP, one of the top priority contaminants, from water by optimization and modeling of argon activated electrohydraulic plasma discharge process and determine the degradation mechanism of the plasma discharge.
4. Coupling of BiOI/C-BNQDs catalyst with CFEHPD process for the effective and efficient degradation and mineralization for p-NP.

CHAPTER 2 VISIBLE-LIGHT DRIVEN BISMUTH OXYIODIDE MODIFIED BY CARBON-BORON NITRIDE QUANTUM DOTS (BiOI/C-BNQDs) FOR DEGRADATION AND MINERALIZATION OF P-NITROPHENOL

2.1 Introduction

p-Nitrophenol (p-NP) is one of the most important and common nitroaromatic compounds in terms of applications and potential environmental and health effects [21, 99, 100]. p-NP is used as a precursor in manufacturing of pesticides, pharmaceuticals, dyes, leather, and explosives [101, 102]. Because of its extensive applications, p-NP is often easily discharged and found as an industrial effluent. However, the treatment and disposal of p-NP is very complex due to its persistent nature and degradation resistance, and its toxic health effects on humans and animals [103]. Due to its potential toxicity, p-NP is listed as a priority pollutant by US Environmental Protection Agency (USEPA) [104]. Therefore, there is an urge for an efficient technology to treat this kind of wastewater.

Over the past decade, advanced oxidation process (AOPs) such as electrochemical oxidation, Fenton oxidation, UV-H₂O₂, UV-persulfate and photocatalysis have been effective for the decomposition of organic pollutants [105]. Especially, photocatalysis has been ascribed as a potential technology due to its unique feature of high oxidation efficiency through production of free radicals such as hydroxyl ($\cdot\text{OH}$), superoxide ($\cdot\text{O}_2^-$) and holes (h^+) at the surface of catalyst [106]. For instance, metal oxide semiconductor such titanium dioxide (TiO₂) and zinc oxide (ZnO) are the most used photocatalysts and have attracted a great deal of attention because of high stability, high photocatalytic activity, low cost, non-toxicity, and high chemical inertness [59, 107]. However, the application of TiO₂ and ZnO are limited by its UV activation requirement. The major shortcoming is the lower utilization of visible light. The wide band gap energy of TiO₂ and ZnO (3.2 eV and 3.4 eV) limits harvesting of solar energy in the visible wavelength region. Moreover, high recombination of photogenerated charge carriers leads to low photocatalytic efficiency [108].

Recently, bismuth oxyhalides (BiOX; X = Cl, Br, I, and F) have been considered as emerging photocatalytic materials and have drawn great interest because of their excellent photocatalytic activity under both UV and visible light [79, 81, 82, 109-111]. These compounds are V–VI–VII ternary oxide semiconductors with interlaced [Bi₂O₂]²⁺ slabs and double halogen layered crystal structure. This layer structure has a self-built internal

electrostatic field which promotes greater separation efficiency of the photo-produced electron/hole pairs. Among the bismuth oxyhalides, bismuth oxyiodide have been described as excellent photocatalysts for wastewater treatment due to its strong absorption in visible light and smallest band gap (E_g) of $\sim 1.8\text{--}1.98$ eV [112, 113]. However, BiOI have a high valence band maximum which limits photocatalytic activity to be allowable for potential industrial applications [114, 115]. Thus, modifying BiOI by doping, modifying crystal facets, surface modification, and combining with other photocatalysts would improve the photocatalytic activity [53, 66, 77-80, 109, 110, 116-124]. Besides that, implanting a small size metal-free material such as quantum dot compound to BiOI might achieve superior photocatalytic activity as it forms the tight contact interfaces and efficiently promote charge transportation and confine the photogenerated electron-hole pairs recombination. Jun Di et al. [125] reported the preparation of carbon quantum dots in situ coupling to bismuth oxyiodide via reactable ionic liquid and found hybrid materials showing excellent contact interface and achieved a high photocatalytic activity than pure BiOI for rhodamine B degradation.

Among the metal-free materials, hexagonal-boron nitride (h-BN) has gained wide interest due to their similar structure like graphene, low toxicity, and unique properties such as excellent chemical stability, high thermal conductivity and abundant active sites featuring excellent photoelectric effects [65-68, 71, 74]. Moreover, the coupling of h-BN with other photocatalyst have already shown excellent photocatalytic activity for degradation of organic pollutants [64, 66, 68, 72]. Reducing the size of boron nitride to quantum dots level would provide more advantage towards the separation of photoinduced charges and absorption of solar light as the BNQDs are negatively charged species dominant to show excellent edge effects and defect centers [126, 127]. Yang et al. [128] reported a metal-free photocatalyst constructed by boron nitride quantum dots (BNQDs) and ultrathin porous $g\text{-C}_3\text{N}_4$ (UPCN). BNQDs/UPCN (BU) photocatalyst displayed excellent visible-light-driven molecular oxygen activation ability, such as superoxide radical ($\cdot\text{O}_2^-$) generation and hydrogen peroxide (H_2O_2) production. The average $\cdot\text{O}_2^-$ generation rate of the optimal sample was estimated to be 0.25 $\mu\text{mol/L/min}$, which was about 2.3 and 1.6 times than that of bulk $g\text{-C}_3\text{N}_4$ and UPCN. Zhang et al. [74] reported BNQDs/BPS-CN-4 for the sulfamethazine (SMZ) degradation. The composites showed excellent photocatalytic activities and photostability for SMZ degradation and the removal efficiency of SMZ reached 100% after 60 min of visible light

irradiation, and the rate constant displayed 13.7 times higher than pure g-C₃N₄. However, the role of BNQDs with other photocatalyst for organic pollutants degradation is still currently limited. Therefore, evaluating the combination of BNQDs with BiOI on p-NP degradation would be interesting to research.

In this work, carbon-boron nitride quantum dots (C-BNQDs) was synthesized using microwave process and different weight content of C-BNQDs was combined with bismuth oxyiodide nanosheets to make a hybrid photocatalyst for the degradation p-NP. Moreover, C-BNQDs modified BiOI photocatalytic activity was evaluated with radical scavenging experiments to know the possible active species involved for the visible light photocatalytic degradation of p-NP and the possible photocatalytic mechanism of BiOI/C-BNQDs was studied.

2.2 Materials and Methods

2.2.1 Chemicals

Bismuth nitrate pentahydrate (Bi (NO₃)₃·5H₂O) (Chemsavers Inc, VA), boric acid, urea, citric acid, potassium iodide (KI), nitric acid and potassium hydroxide (KOH) from Fisher Scientific (Eugene, OR) and p-Nitrophenol from TCI chemicals Pvt. Ltd.

2.2.2 Synthesis of C-BNQDs

Boric acid (boron), urea (nitrogen) and citric acid (carbon) were used as precursors. 0.5 g boric acid, 0.3 g urea and 0.05 g citric acid were dissolved in 15 mL distilled water. The solution was stirred for 20 minutes to form homogenous solution. Then the solution was heated for 5 min in a domestic microwave oven (700 W) without any cover. After heating, a light-yellow solid was form, which further dissolved in 30 mL distilled water and the solution was centrifuged for 30 minutes at 5000 rpm to remove excessive raw material. The clear solution was collected and filtered using 0.22 μm microporous membrane filter for two times. The resultant solution was stored at 4 °C for further analysis.

2.2.3 Synthesis of Bismuth oxyiodide (BiOI) and BiOI/C-BNQDs.

In BiOI synthesis, 0.5 g of bismuth nitrate pentahydrate Bi (NO₃)₃·5H₂O was dissolved into 0.2 M nitric acid (HNO₃) in 20 ml distilled water under vigorous stirring for

30 min. 1 M of potassium iodide (KI) was added in to 5ml of distilled water and added dropwise into the solution.

pH of 6 was adjusted by using 5M potassium hydroxide (KOH) and stirred for one hour. Then, the solution was passed into hydrothermal reactor and heated in an oven at 160 °C for 2 hours. After that, particles were collected by centrifugation technique at 5000 rpm for 10 min. The particles were washed with distilled water and ethanol many times to remove residual ions and was dried in an oven at 70°C. The dried fine powder was further subjected to different characterization techniques.

For synthesis of BiOI/C-BNQDs composites, 300 mg of BiOI was added to 20 mL methanol and ultrasonicated for one hour. Then, C-BNQDs of volume of 1 mL, 3mL and 5mL were added to the BiOI solution and sonicated overnight. The BiOI/C-BNQDsX, (X=1 mL, 3mL, and 5mL) photocatalysts was dried in a vacuum oven at 50 °C for 12 hours for methanol to be completely evaporated.

2.2.4 Characterization of materials

X-Ray diffraction (XRD) was carried out using Siemens D5000 powder diffractometer to know the crystal structure and phase purity of the materials. Diffractometer was equipped with copper x-ray source with wavelength, $\lambda = 1.5406 \text{ \AA}$. Data was recorded in the range of 2 theta from 10° -80° with 0.05° step using a 2.50 second acquisition time per step.

Fourier transform infrared (FT-IR) spectra was recorded at room temperature in the region of 400-4000 cm^{-1} using Thermo Scientific Nicolet iS5 Spectrometer.

A Leo Supra 35 SEM with an energy dispersive spectroscopy (EDS) was used to determine the surface morphology of the materials. A carbon double-sided tape was used to mount the powder samples on the specimen stubs. Transmission electron microscopy (TEM) from Thermo Scientific Talos L120C was used to know the size and surface morphology of the C-BNQDs modified BiOI.

In addition, X-ray photoelectron spectroscopy (XPS) characterization was carried out using a Kratos AXIS ULTRADLD XPS system equipped with an Al $K\alpha$ monochromated X-ray source to know the chemical bonding, elements constituting the sample surface and its composition.

2.2.5 Photocatalytic activity

A photocatalytic activity measurement of as prepared composites was used for the degradation of p-NP aqueous solution. Cool white waterproof LED strips with the dimensions 5 metre x 8mm x 2mm consisting of 60 (SMD type-3528) LEDs obtained from HitLights, USA with the following specifications: Input: 12V DC/2.8 Watts per Foot, Total: 48W and Output: 338 Lumens per Foot was used as a light source. A continuous recirculating photoreactor was used for degradation experiments. The photoreactor was made up of pyrex glass having two inner and outer glass tubes 33mm and 51 mm respectively, two teflon made flow dispersion disks for well disturbed and continuous flow of water throughout the reactor and teflon made end parts on top and bottom of the photoreactor.

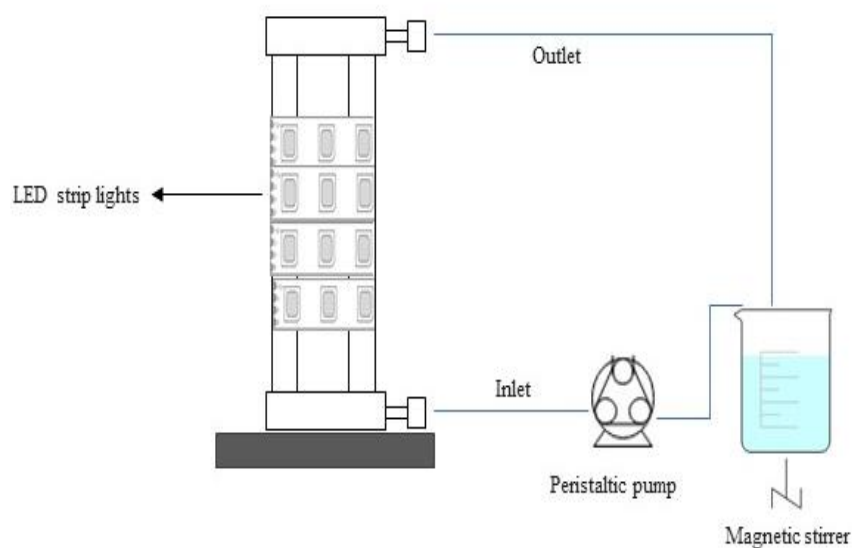


Figure 2.1. Recirculating photoreactor

The total volume used per each batch was 300 mL. Initial concentration of 10 mg/L of p-NP was added in a three neck round bottomed glass beaker. Later, 300 mg of different weight content catalyst BiOI/C-BNQDsX (X=1, 3 and 5 mL) including with BiOI was added in batch into the mixture. Prior to the start of the experiment, the solution was stirred continuously in the dark for 30 min to establish an adsorption-desorption equilibrium. At the specified irradiation time intervals (10 min, 20 min, 30 min, 40min, 50 min, 60 min, 120 min and 180 min), 5 mL of the suspension was collected and then centrifuged at 5,000 rpm for 10 min to separate the particles.

2.2.6 Sample analysis

The p-NP was analyzed using UV-vis spectroscopy at 317 nm. The degradation efficiency of p-NP was measured as follows:

$$n = C_0 - C / C_0 * 100\% \quad (1)$$

Where: C_0 is the initial concentration and C is the final concentration after irradiation.

Total organic carbon (TOC) was measured using a TOC kit was used and analyzed by Hach DR3900 laboratory spectrophotometer.

$$TOC (\%) = (TOC_0 - TOC_t) / TOC_0 * 100 \quad (2)$$

where TOC_0 = TOC of initial solution and TOC_t = TOC of the solution at time t .

2.2.7 Radical trapping experiment

To identify the active species, ascorbic acid (3mmol/L), 2-propanol (10 ml) and ammonium oxalate (3mmol/L) were used as a radical scavenger for $\cdot O_2^-$, $\cdot OH$ and h^+ respectively. The experiment was similar to that of photocatalytic process, where each scavenger was added with the catalyst into the p-NP solution (10 mg/L).

2.3 Results and Discussion

2.3.1 XRD analysis

Fig 2.1 shows the XRD patterns of C-BNQDS and BiOI/C-BNQDsX (X=1 mL, 3 mL, and 5 mL). C-BNQDs displayed a major peak at $2\theta=26.5^\circ$ which corresponds to the (002) crystal plane of BN and carbon atoms [129-131]. The characteristic peaks of pure BiOI exhibited around 2θ of 29.7° and 31.8° , resembles a tetragonal phase of BiOI (JCPDS Card No: 10-0445). The XRD patterns of BiOI/C-BNQDsX (X=1 mL, 3 mL, and 5 mL) looks similar to that BiOI. The addition of different weight contents of C-BNQDs did not show any changes in the characteristic peaks or crystalline structure of BiOI. This may be due to the low content and weaker diffraction intensity of C-BNQDs [66, 125].

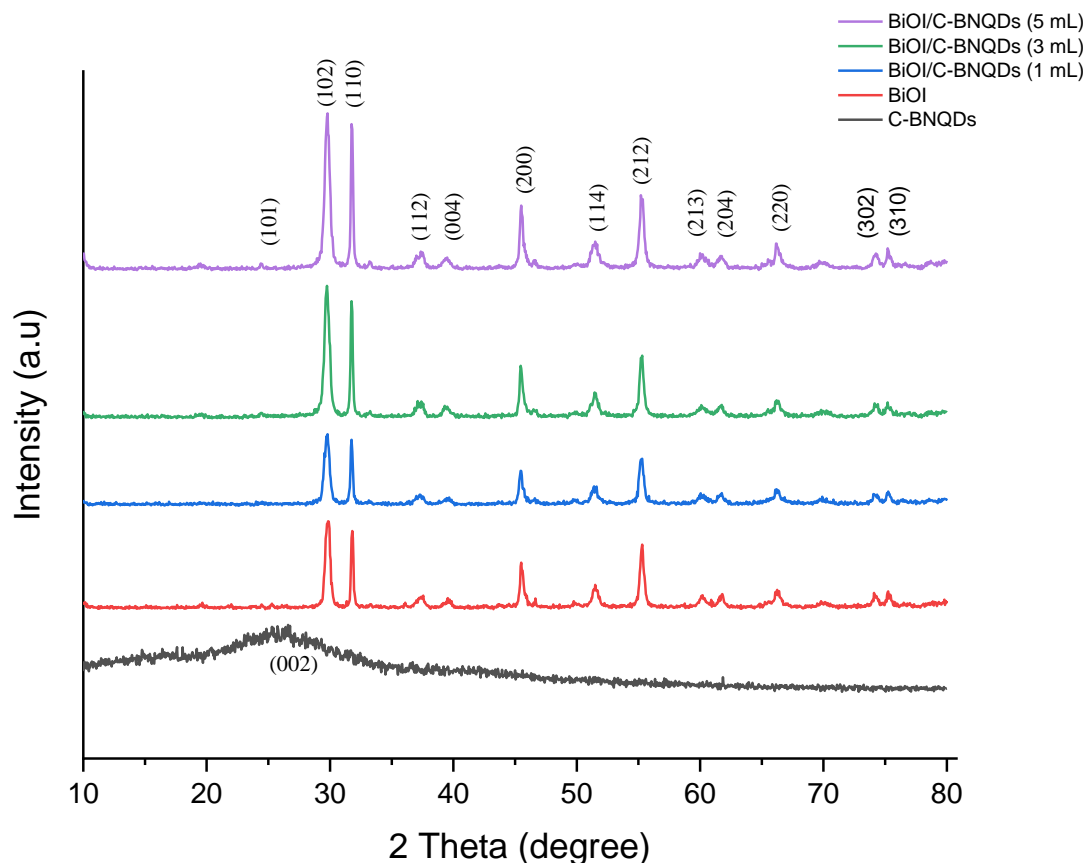


Figure 2.2. XRD patterns of C-BNQDs, BiOI and BiOI/C-BNQDsX (X= 1, 3 and 5 mL)

2.3.2 FTIR spectroscopy

FTIR spectroscopy was used to measure the bonding structure and characteristics of C-BNQDs, BiOI and BiOI with different weight contents of C-BNQDs (1, 3 and 5 mL) and the results are shown in Fig 2.2. In the FTIR spectra of C-BNQDs, the peaks around 1315 cm^{-1} were recognized as B-N stretching vibrations and the peak at 1540 cm^{-1} corresponded to C-BN bonding vibrations [129-131]. In addition, B-N-B out of plan bending vibrations was attributed at 787 cm^{-1} [132]. And the broad peak around 3200 cm^{-1} was recognized as the stretching vibrations of -NH and -OH respectively [71, 133]. In BiOI spectra, the peaks at 772 cm^{-1} and 1620 cm^{-1} were ascribed as Bi-O stretching bond and bending vibrations of O-H groups, respectively [80, 125, 132]. For the BiOI/C-BNQDsX (X=1, 3 and 5 mL) the peak at 1350 cm^{-1} and 1540 cm^{-1} clearly indicated the existence of C-BN, that gradually increased by increasing the weight contents of C-BNQDs.

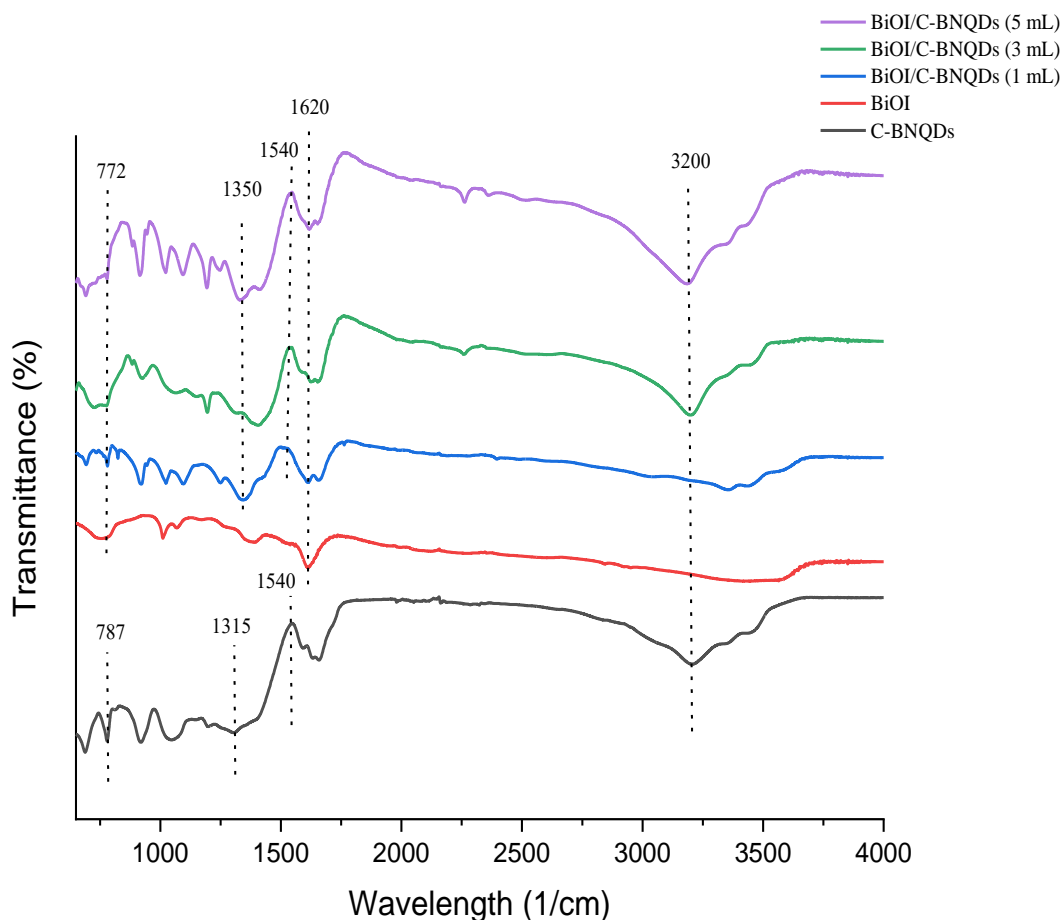


Figure 2.3. FTIR spectra of C-BNQDs, BiOI and BiOI/C-BNQDsX (X= 1, 3 and 5 mL)

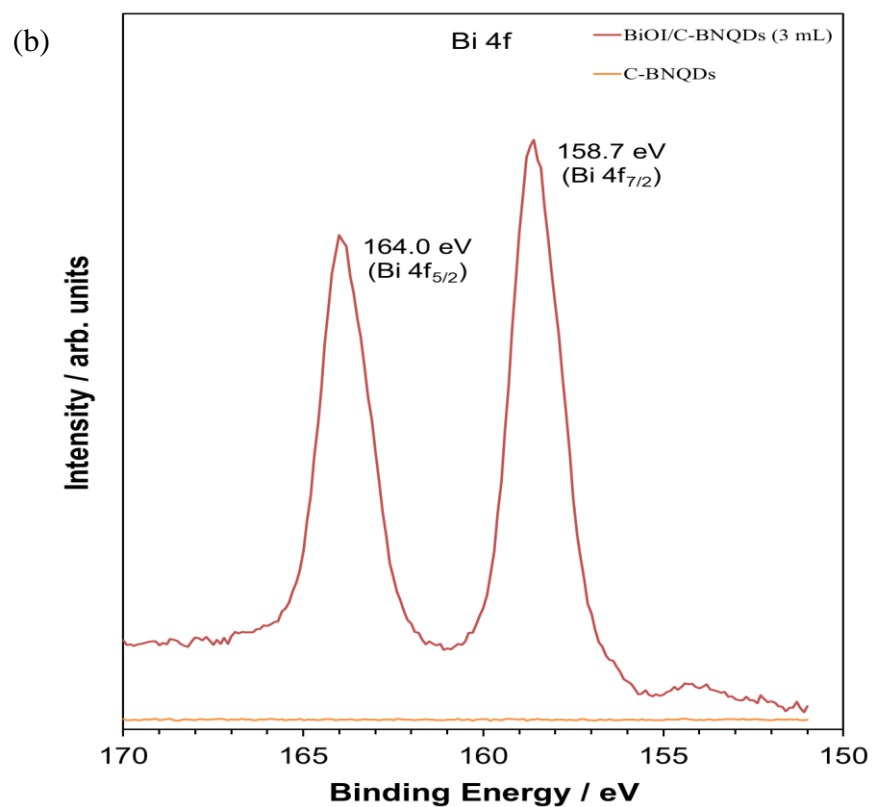
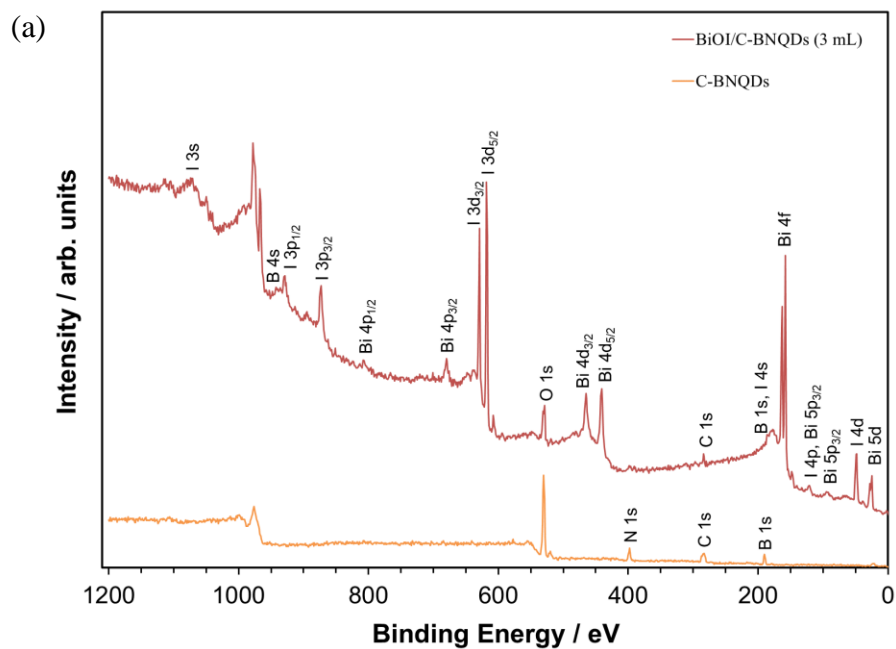
2.3.3 XPS analysis

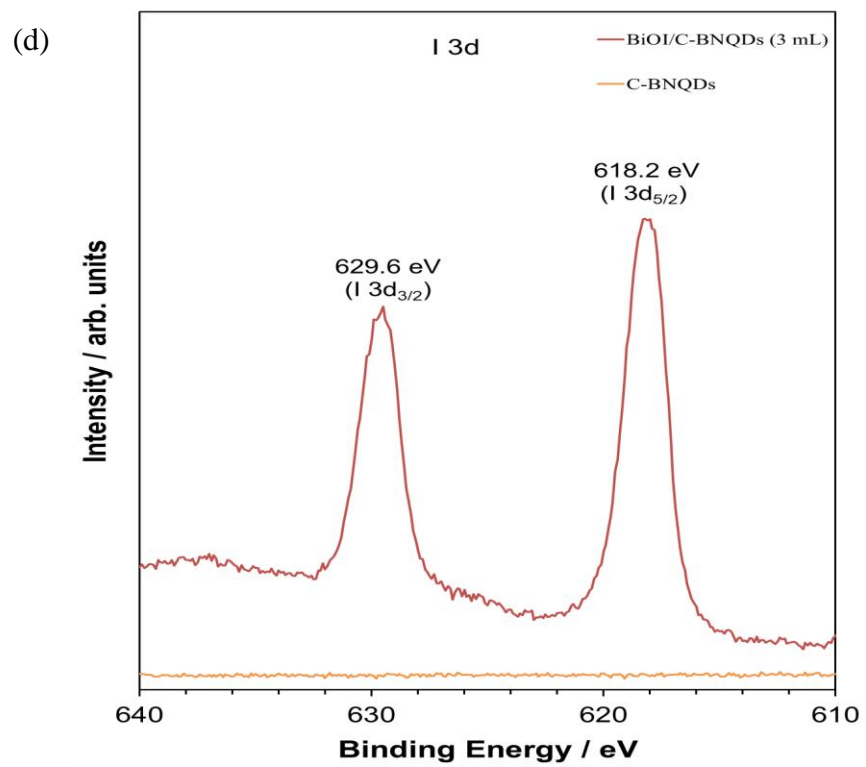
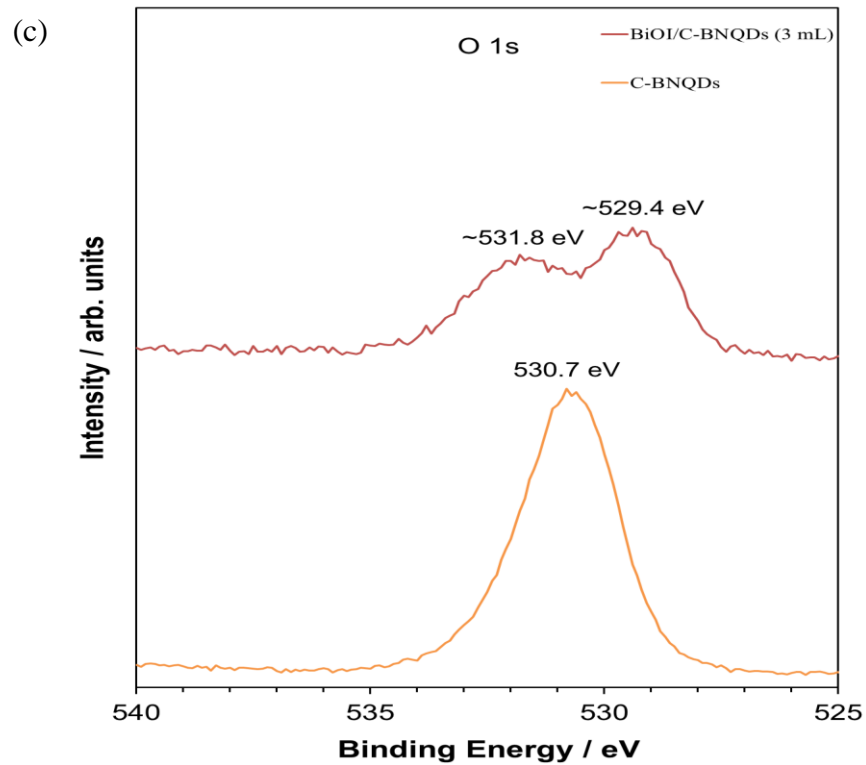
The surface chemical compositions and chemical states of the C-BNQDs and BiOI/C-BNQDs (3 mL) were investigated using XPS. C, B, N and O were detected in C-BNQDs sample and Bi, O, I, C, B and N were detected in the BiOI/C-BNQDs (3mL) sample, according to XPS survey spectrum as shown in the fig. 2.3 (a). The high resolution XPS spectrum of Bi 4f is shown in the fig. 2.3(b), where Bi 4f_{7/2} and Bi 4f_{5/2} were found to have strong significant peaks at 158.7 and 164.0 eV, indicating that Bi was present in its trivalent chemical form Bi³⁺ [134, 135]. The O 1s peaks at 529.4 and 531.8 eV binding energies (Fig. 2.3 (c)) was assigned to oxygen in BiOI material and for C-BNQDs, binding energy 530.7 eV was assigned as O 1s [125, 136]. The two strong peaks at 618.2 eV and 629.6 eV (Fig. 2.3 (d)) corresponded to the binding energies of I 3d_{5/2} and I 3d_{3/2}, respectively [66, 134, 137].

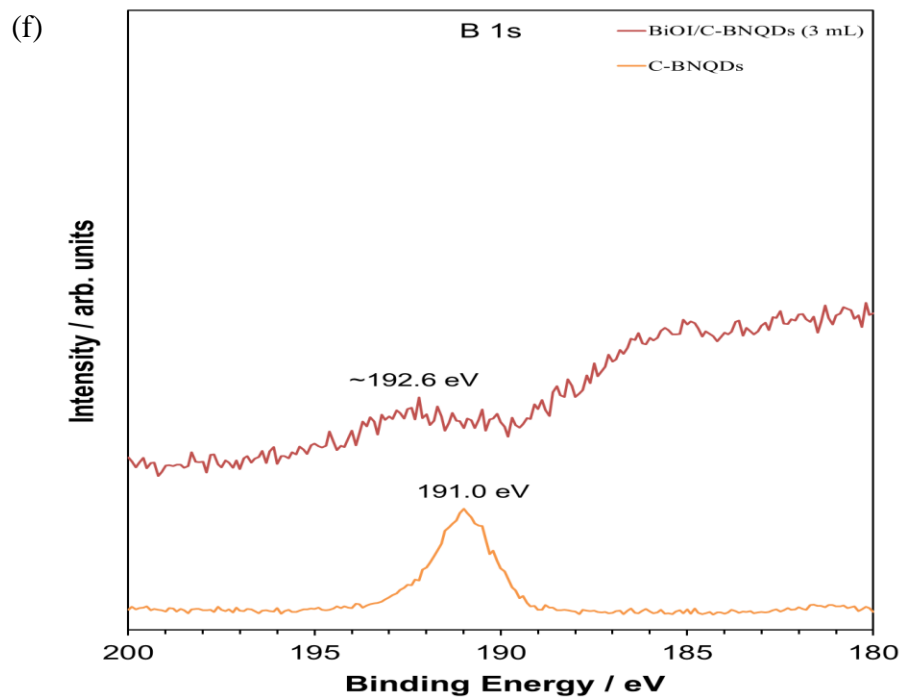
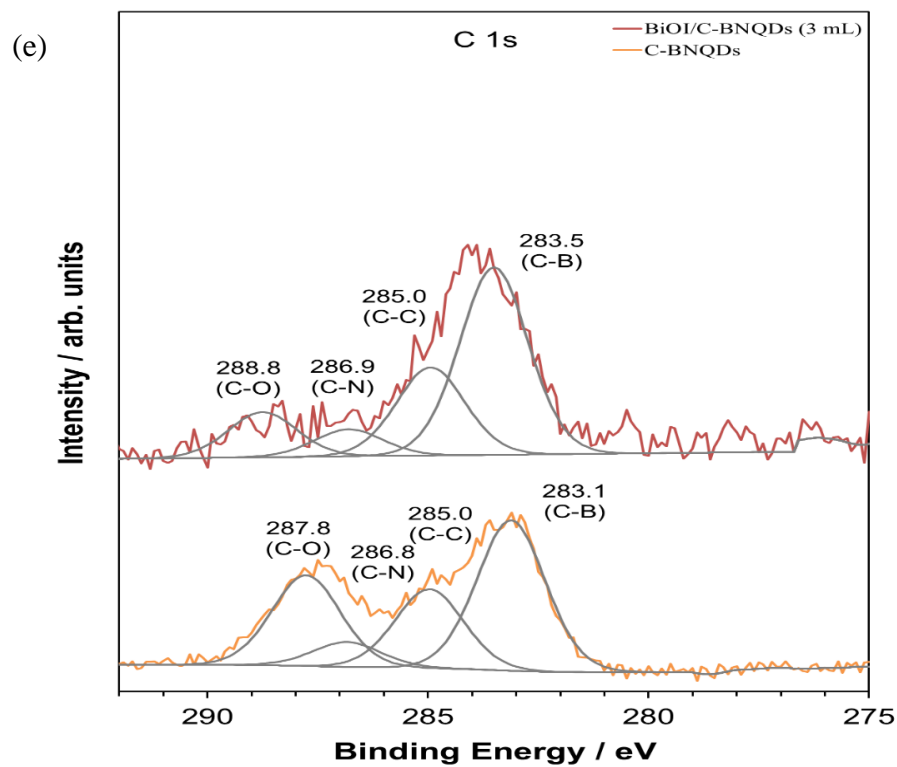
The signals at 283.5, 285.0, 286.9 and 288.8 eV in the high-resolution XPS spectrum of C 1s indicated the presence of C-B, C-C, C-N and C-O functional groups, respectively in BiOI/C-BNQDs (3 mL) material [66, 132]. Meanwhile, in the C-BNQDs material, C 1s were assigned at peaks 283.1, 285.0, 286.8 and 287.8 (Fig. 2.3 (e)) indicated the presence of C-B, C-C, C-N and C-O functional groups like the BiOI/C-BNQDs material [125, 128]. In the fig 2.3 (f), boron corresponds to the peaks at 191.0 and 192.6 eV in the B1s narrow region for C-BNQDs and BiOI/C-BNQDs (3 mL) [75, 138, 139]. The high-resolution spectrum of N 1s peaks at 398.5 eV for C-BNQDs; 396.8 and 399.7 eV for BiOI/C-BNQDs (3 mL) in fig 2.3 (f), could be attributed to N-B, N-C and N-H bonds [74, 140]. As a result, the XPS analysis confirms the coexistence of BiOI and C-BNQDs in the BiOI/C-BNQDs (3 mL) material.

Table 2.1. Relative atomic surface compositions (%) of C-BNQDs and BiOI/C-BNQDs (3 mL)

	Relative Atomic Concentration (%)					
	I	O	N	C	B	Bi
	%	%	%	%	%	%
C-BNQDs	0	41	12	21	26	0
BiOI/C-BNQDs (3 mL)	15	29	5	24	11	16







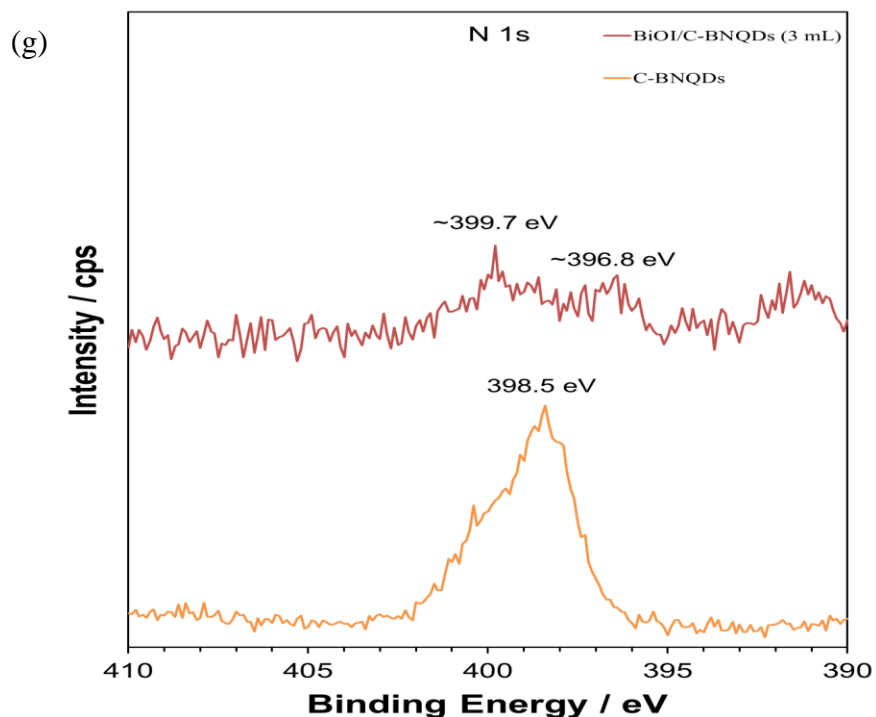
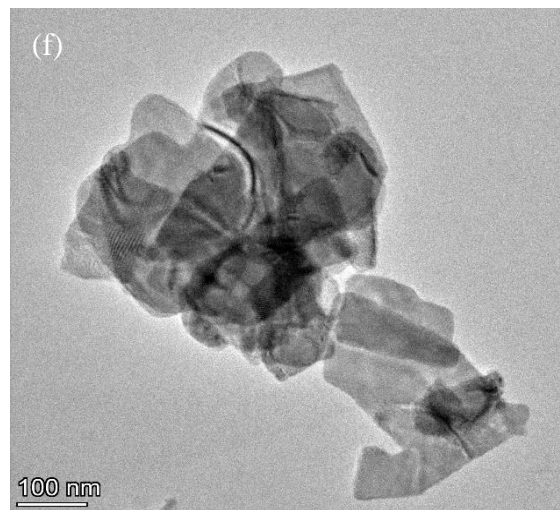
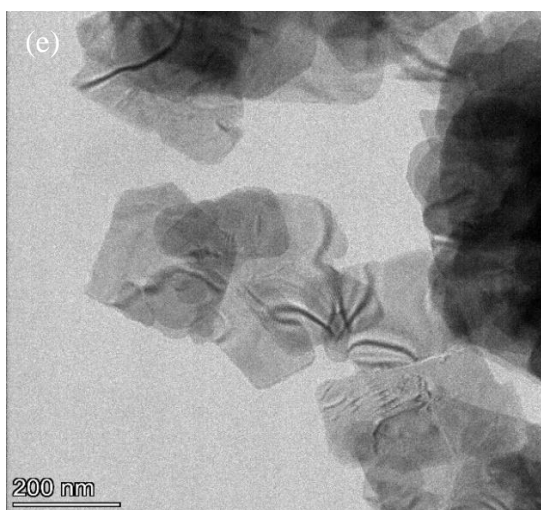
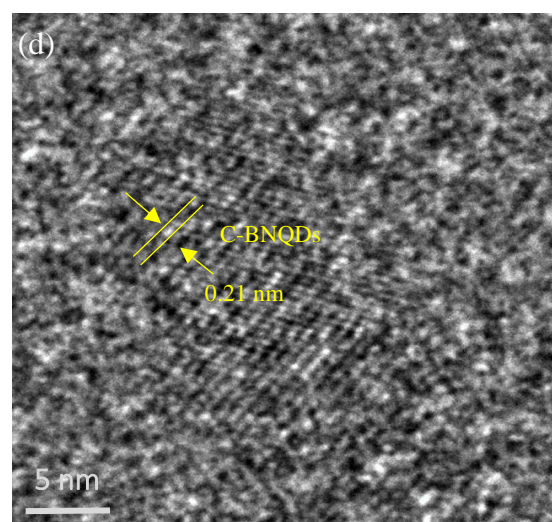
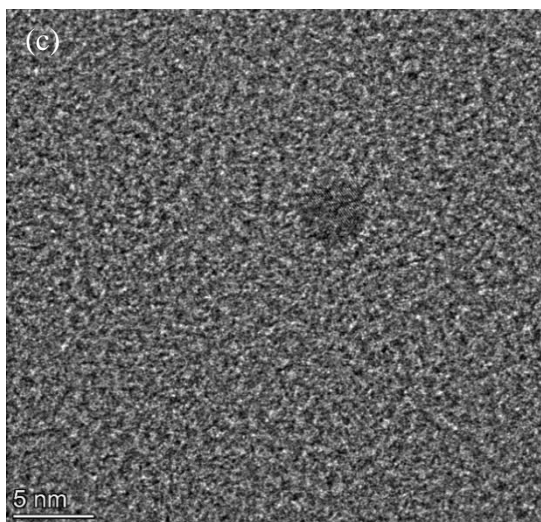
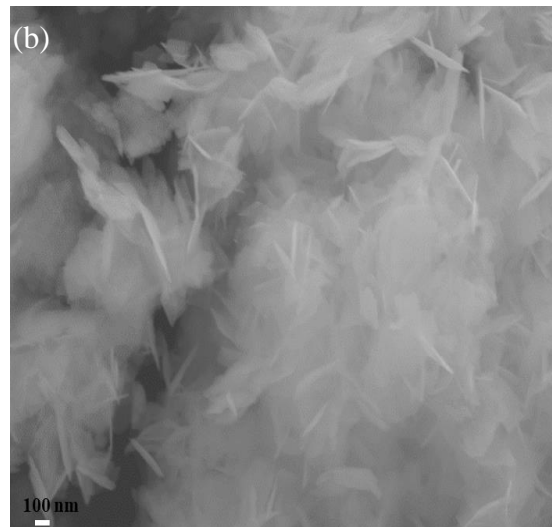
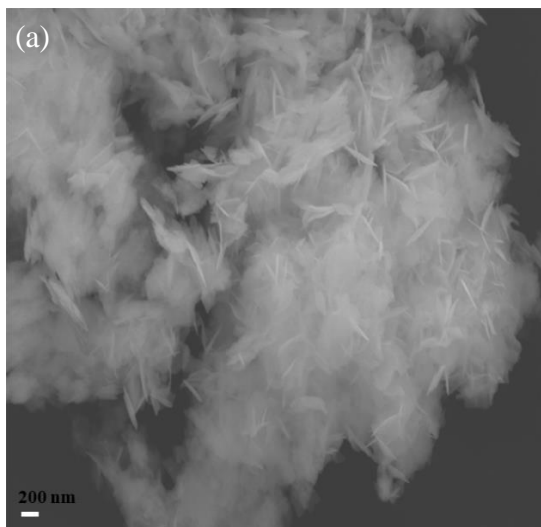


Figure 2.4. (a) XPS Survey of C-BNQDs and BiOI/C-BNQDs (3 mL); (b) Bi 4f; (c) O 1s; (d) I 3d; (e) C 1s; (f) B 1s; and (g) N 1s

2.3.4 SEM and TEM analysis

The field emission SEM and TEM were used to determine the morphology of BiOI/C-BNQDs photocatalyst. Fig. 2.5 (a, b) depicts the SEM image of pure BiOI material, which indicates that BiOI as aggregated nanosheets. The HRTEM image of C-BNQDs showed that C-BNQDs have a spherical structure with an average diameter of 4 nm and it exhibited a high degree of crystallinity, as evidenced by 0.21 nm lattice fringes (fig. 2.5 (d)), which corresponds to BN and graphitic carbon lattice planes (100) [74, 131, 141, 142]. In addition, the TEM image in Fig. 2.5 (e,f) indicated that a nanosheet structure for the BiOI/C-BNQDs (3 mL) material. The arrangement of C-BNQDs and BiOI through HRTEM was shown in Fig. 2.5 (g). C-BNQDs were evenly dispersed over the surface of BiOI nanosheets, indicating that C-BNQDs have been successfully introduced onto BiOI surface. Moreover, BiOI exhibit a clear lattice spacing of roughly 0.27 nm, which corresponds to the (111) crystal plane of BiOI [66, 143].



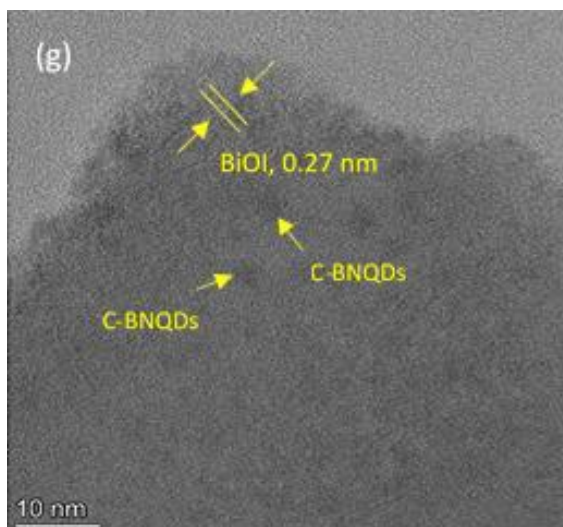


Figure 2.5. (a, b) SEM images of BiOI; (c, d) HRTEM images of C-BNQDs; (e, f) TEM images of BiOI/C-BNQDs (3 mL); (g) HRTEM image of BiOI/C-BNQDs (3 mL)

2.3.5 Photocatalytic Degradation Study

The photocatalytic activity of the synthesized BiOI/C-BNQDsX (X=1, 3 and 5 mL) materials was explored for the degradation of p-NP under visible light irradiation. The experimental results show that all composites have adsorption capacity less than 3% after 30 min of dark adsorption. This result indicated that degradation of p-NP was caused by photocatalysis. As shown in the fig 2.6, BiOI/C-BNQDs (3 mL) showed a high degradation rate of 95.7% for p-NP within 180 minutes of irradiation. Whereas the weight content of C-BNQDs (1 mL and 5 mL) sample showed 91.9% and 90.7 %, which have a little low degradation rate compared to BiOI/C-BNQDs (3mL) within the 180 min of irradiation. The photocatalytic activity of BiOI/C-BNQDs (3 mL) was higher than that of BiOI and BiOI/C-BNQDs (1 and 5 mL). When the C-BNQDs exceed the optimal proportion, the photocatalytic performance of the composite decreased, indicating that the presence of more C-BNQDs depress the light harvesting ability by covering the active sites of BiOI [135, 144]. In addition, when compared with BiOI (65.9%), the degradation rate of the composite photocatalysts was much higher. This clearly indicates that the addition of C-BNQDs with BiOI enhance the photocatalytic performance activity.

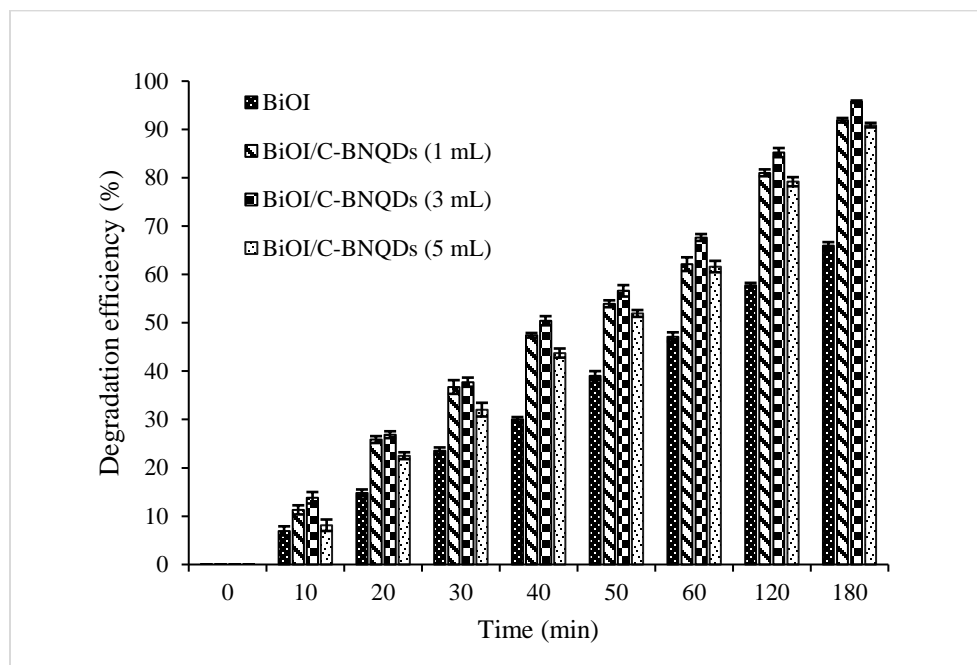


Figure 2.6. Degradation efficiency of BiOI and BiOI/C-BNQDsX (X=1, 3 and 5 mL)

As shown in fig. 2.7 and table 2.2, the degradation reaction process can be fitted to pseudo-first-order kinetics by the equation of $-\ln(C_t/C_0) = kt$. The rate constant ($k \text{ min}^{-1}$) value of BiOI/C-BNQDs (3 mL) is 0.0173 min^{-1} , which is 2.83 times higher than the BiOI material. The kinetic rate Half-life for first order kinetics is calculated by using equation (3). The enhanced photocatalytic performance was due to the introduction of C-BNQDs, which accelerate the transfer of charges and stimulate the dissociation of excitons [128]. Considering the total volume treated in this study, composites showed effective photocatalytic degradation of p-NP.

$$t_{1/2} = \ln(2)/\text{rate constant (K)} \quad (3)$$

Moreover, TOC analysis was used to determine the extent of p-NP mineralization. Fig 2.8 shows the TOC removal at different time intervals of photocatalytic irradiation, the BiOI/C-BNQDs removes 65.56% of TOC from p-NP after 180 minutes of irradiation. The mineralization rate showed there was residual carbon content left after degradation of p-NP as it got transform into aliphatic compounds, nitrate, water, and carbon dioxide.

Table 2.2. Rate constant (K) and R squared values of photocatalytic degradation study

Photocatalyst	p-NP (rate constant K)	p-NP (R ² Value)	t _{1/2} (half-life)
BiOI	0.0061	0.9311	113.63
BiOI/C-BNQDs (1mL)	0.0139	0.9959	49.86
BiOI/C-BNQDs (3 mL)	0.0173	0.9952	40.06
BiOI/C-BNQDs (5mL)	0.0133	0.9934	52.11

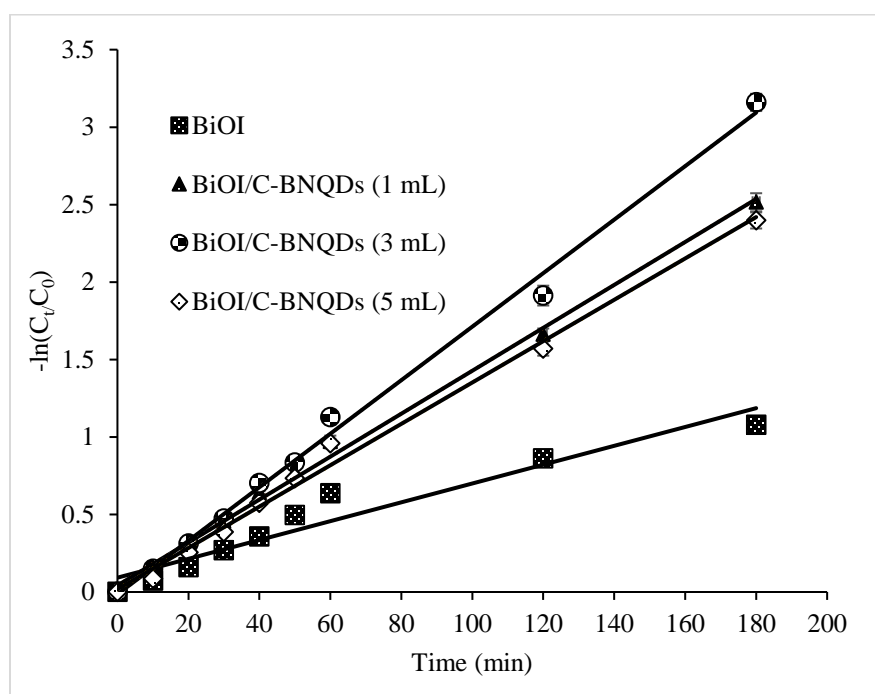


Figure 2.7. First order kinetics for p-NP degradation by BiOI and BiOI/C-BNQDsX (X= 1, 3 and 5 mL)

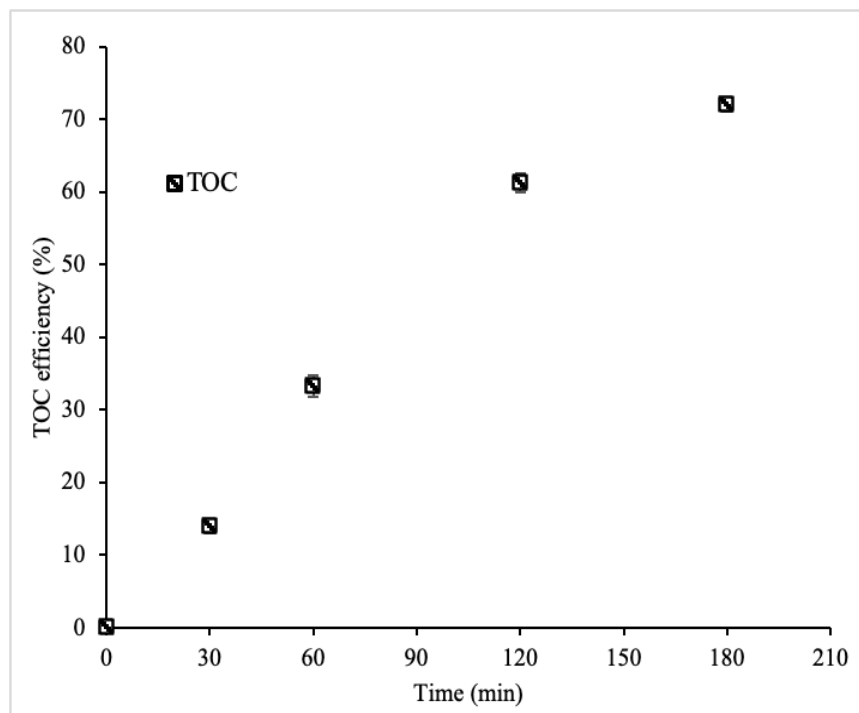


Figure 2.8. TOC removal efficiency for p-NP degradation by BiOI/C- BNQDs (3 mL)

2.3.6 Reusability of photocatalyst

Recycling tests with BiOI/C-BNQDs (3mL) for the degradation of p-NP under LED visible light irradiation was used to assess the stability of the composite photocatalyst. The photocatalysts were collected by centrifugation, cleaned with distilled water and dried in oven at 50 °C for 5 hours after each cycle. As shown in Fig. 2.9, after three recycling runs, the photocatalytic efficiency almost showed an average of 87% degradation of p-NP. The results show that the composite was relatively stable and may be reused easily. Therefore, all results showed that BiOI/C-BNQDs (3 mL) was a suitable photocatalyst for use in environmental applications.

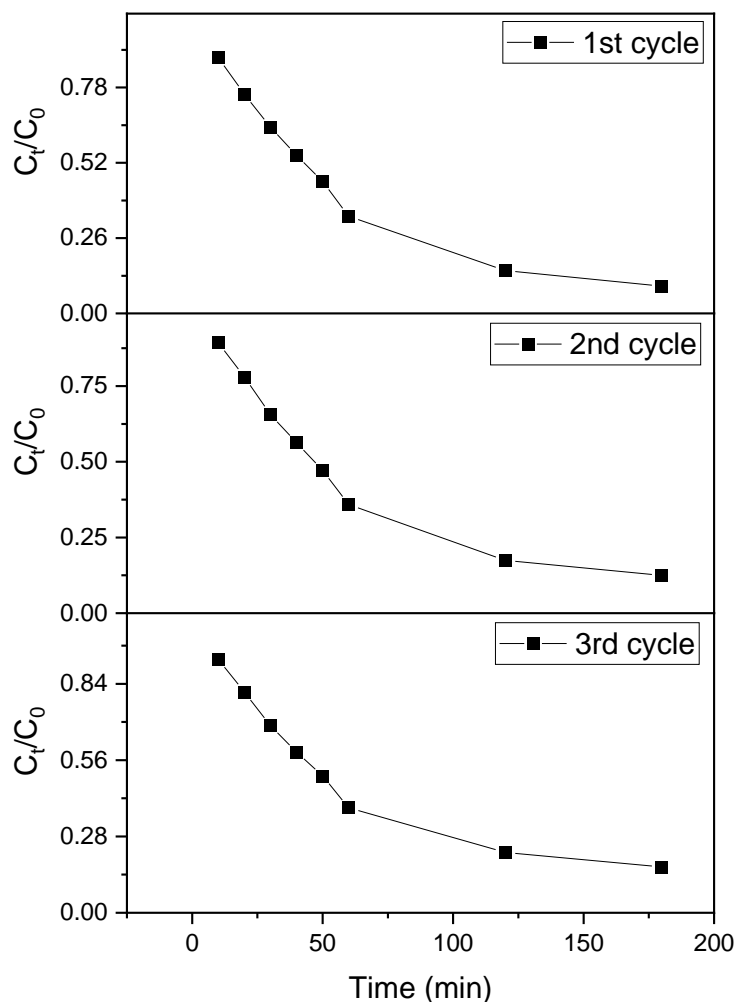


Figure 2.9. Reusability of BiOI/C- BNQDs (3 mL) for the degradation of p-NP

2.3.7 Radical trapping experiment

To investigate the influence of different free radicals on catalytic activity, BiOI/C- BNQDs (3mL) was used to degrade the p-NP, while ammonium oxalate, isopropanol (IPA), and ascorbic acid (AA) were used as radical scavengers to capture holes, hydroxyl radicals, and superoxide radicals, respectively. As shown in Fig 2.10, When ammonium oxalate, IPA, and AA were added to the reaction solution, the degradation efficiencies were 56.95%, 64.48%, and 43.07%, respectively, which were all lower than the 95.75% of BiOI/C-BNQDs (3mL) within 180 min of treatment. These results demonstrate that the most active species in

the process tested were superoxide radicals ($\cdot\text{O}_2^-$) and holes (h^+), with hydroxyl radicals ($\cdot\text{OH}$) as the second most active.

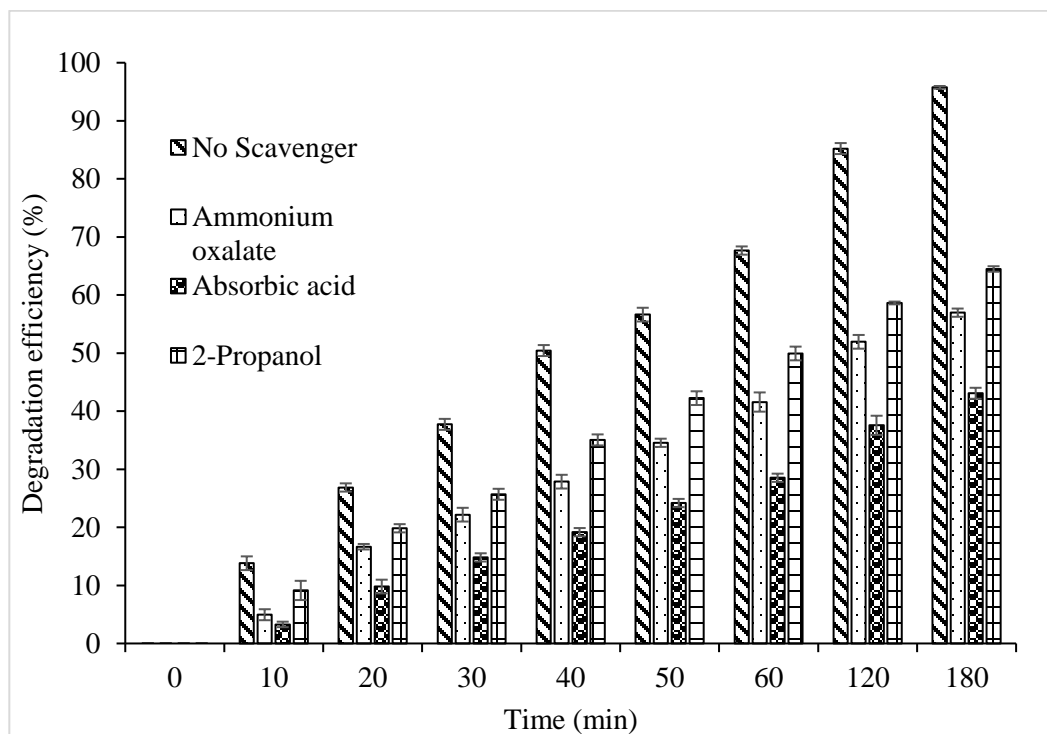
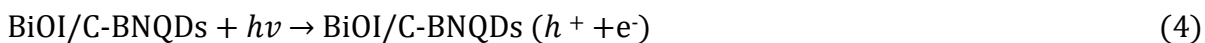


Figure 2.10. Photodegradation efficiencies of p-NP with different quenchers

2.3.8 Possible photocatalytic mechanism

The photocatalytic mechanism of BiOI/C-BNQDs (3 mL) was proposed based on the above experimental results. Under visible light irradiation, electrons on the valence band (VB) of BiOI were excited and transferred to the conduction band (CB), leaving behind the corresponding holes on the VB. The photogenerated electrons on the CB of BiOI were transferred to the C-BNQDs, resulting in effective separation of photogenerated electron-hole pairs and limit the electron-hole pair recombination. The transferred electrons accumulated on the surface of C-BNQDs could make O_2 reduce to generate $\cdot\text{O}_2^-$ through a single electron process. Then $\cdot\text{O}_2^-$ and electrons reacts with H^+ to form hydrogen peroxide (H_2O_2), which further transforms into $\cdot\text{OH}$ radicals. In contrast, the holes in the VB can also oxidize water to form $\cdot\text{OH}$ radicals. Therefore, superoxide ($\cdot\text{O}_2^-$), holes (h^+) and hydroxyl radicals ($\cdot\text{OH}$) were formed on the BiOI/C-BNQDs (3 mL) surface, responsible together for the degradation of p-NP.



2.4 Conclusions

In this study, BiOI/C-BNQDsX (X= 1, 3 and 5 mL) were prepared successfully using a facile method. XRD, FTIR, XPS, SEM and TEM were used to characterize the synthesized materials. Based on lattice planes, XRD analysis revealed a tetragonal phase of BiOI and no apparent peaks of C-BNQDs were observed in BiOI/C-BNQDsX, which could be attributed to the low amount of C-BNQDs in the composite. FTIR analysis showed the existence of C-BN in the composite materials, which gradually increased by increasing the weight contents of C-BNQDs. XPS analysis identified the coexistence of BiOI and C-BN in the BiOI/C-BNQDs (3 mL) material. SEM revealed pure BiOI as aggregated nanosheets shaped formations and HRTEM showed that C-BNQDs have a spherical structure with an average diameter of 4 nm. Moreover, HRTEM indicated that C-BNQDs were evenly dispersed over the surface of BiOI nanosheets. The visible light photocatalytic performance of synthesized materials was evaluated using the degradation of p-NP solution. In comparison with different weight contents, the BiOI/C-BNQDs (3 mL) sample showed a high degradation rate of 95.7% and TOC mineralization rate of 65.56% for p-NP during 180 minutes of irradiation. Furthermore, the results of active species trapping experiments identify that the superoxide radicals and photogenerated holes plays major roles in the photocatalytic degradation of p-NP. This study can provide a highly efficient and stable hybrid photocatalyst for the degradation of organic pollutants in a natural environment.

CHAPTER 3 REMEDIATION OF METHYLENE BLUE BY CONTINUOUS-FLOW ELECTROHYDRAULIC PLASMA DISCHARGE

3.1 Introduction

For the past few decades, rapid growth in population and industries has led to an increasing demand for energy and clean water all over the world. However, clean water has been, and is being, deteriorated by the toxic organic pollutants released from the industries. For instance, discharge of high concentrations of dyes in wastewater is one of the major problems in the world [25, 145]. Most of the organic dyes in wastewater are highly toxic and considered to be potential carcinogens to humans. Moreover, these dyes have complex and stable structures [146], which make them very resistant and difficult to degrade by conventional biological and physico-chemical processes [147]. Therefore, to maintain a clean and sustainable water supply, the only possible way is to develop effective treatment technologies to recycle and reuse the wastewater.

To treat dye wastewater, considerable interest has been given to advanced oxidation processes (AOPs), as they show specific advantages over other conventional treatments. AOPs can generate highly reactive hydroxyl radicals (oxidation potential of 2.8 V), which are strong oxidizers and are potent in degrading organic pollutants due to their electrophilic behavior [29]. Various AOP processes have been studied extensively and reported such as Fenton, UV/O₃ sonolysis, photocatalysis, UV/H₂O₂, etc. [25, 148]. Although effective, the applications of these technologies are limited due to the insufficient concentration of hydroxyl radicals ($\cdot\text{OH}$), high operating cost, and high energy consumption. Thus, there exists an urgent need to develop a robust water remediation technology for dye wastewater treatment.

Recently, electrical discharge in liquid with non-thermal plasma (NTP) generation is recognized as an effective, robust AOP method, as it generates many physicochemical effects such as highly reactive oxidative species (O₃, H₂O₂, $\cdot\text{O}$, $\cdot\text{OH}$), UV light, electric field, ions, electrons and shock waves [25, 32, 149, 150]. Various types of electrical discharge reactors including atmospheric pressure plasma, dielectric-barrier discharge (DBD), plasma jet, arc discharge, and corona discharge have been reported. Among these models, the DBD plasma process has been widely tested for wastewater remediation [151-153]. A DBD reactor was investigated by Czapka et al. [154] with air as a gas medium for decolorization of methylene

blue (MB) in aqueous samples. The results showed a complete MB decolorization within 30 min of treatment. In another study reported by Reddy et al. [84], a DBD reactor was operated with the addition of Fe^{2+} for degradation and mineralization of MB in solution. The results showed more than 95% MB degradation and 21% total organic carbon (TOC) removal within 25 min of treatment at an initial concentration of 100 ppm. In a recent study reported by L. Wu et al., the degradation efficiency of a hybrid DBD system was 97.9% within 10 min treatment, which was close to their plasma alone treatment for 30 min [155]. Currently, there are many new developments in plasma technology, by combining the plasma reactor with other treatment technologies to improve synergistic effects [156]. However, the efficiency of a particular plasma process depends on their reactor configuration and geometry [149, 157]. Moreover, the optimization of the current plasma technology is complex because of the types of reactor designs and materials used, discharge types, and operational parameters [158]. Therefore, it is important to develop an effective, robust plasma reactor that can further improve the degradation and mineralization efficiency of water pollutants without the addition of chemicals or absorbents.

In this study, a novel, continuous-flow electrohydraulic plasma discharge process (EHPD) was developed and evaluated for degradation of dye wastewater. The degradation efficiency was evaluated in light of the operational parameters such as liquid flow rate, air flow rate, and initial dye concentration. Once the best operational parameters were established, the energy yield was evaluated and compared with those of the other plasma systems. A radical scavenging experiment was conducted to determine the role of active species involved. In addition, the treated liquid was characterized for conductivity, pH, COD and degradation byproducts. The degradation mechanism was also briefly discussed.

3.2 Methods and Materials

3.2.1 Materials

Methylene blue (MB, $\text{C}_{16}\text{H}_{18}\text{N}_3\text{SCl}$) purchased from HiMedia Laboratories Pvt. Ltd. was used as the target pollutant. Different stock solutions (10 mg/L, 20 mg/L, 50 mg/L, and 100 mg/L) of MB were prepared by dissolving the chemical in deionized water. Other chemicals such as ascorbic acid, 2-propanol ($\text{C}_3\text{H}_8\text{O}$) and sodium nitrate (NaNO_3) used for radical scavengers were purchased from Fisher Scientific (Eugene, OR).

3.2.2 Experimental setup

The body of the electrohydraulic discharge reactor was made from polycarbonate material. The power was supplied by a high voltage transformer (catalog#: 110-LLHI10122/D115, Plasma Technics, Inc., Racine, WI, output: 12 KV), which was connected to an AC power. The plasma discharge was initiated between two stainless steel electrodes separated by a dielectric plate. The novel configuration of the electrohydraulic discharge reactor presented in this study was shown in Fig. 3.1. The dielectric plate between the electrodes was designed with a small opening in the middle (0.8 mm). Compared to the most common researched designs, pin-pin and pin-plate electrohydraulic discharge reactors, this design had a unique feature of establishing a complete discharge through the conducting channel of the orifice instead of between the electrodes. The orifice in the middle of the dielectric plate allowed electrons generated to be concentrated in the vicinity of the opening, and the continuity of discharge current could be achieved in the form of mobile electrons in the plasma phase to obtain a better mass transfer and breakdown of substrate molecules in contact with the plasma discharge. The voltage and power applied were adjusted by a Variac variable voltage regulator (model#: TDGC2-2KM, ISE, Inc., Cleveland, OH). The applied voltage between the top electrode and the ground electrode was measured by a high voltage probe (Tektronix P6015A) connected to an oscilloscope (Tektronix TBS1052B, Beaverton, OR). The power applied to the whole system was read from a power consumption Watt meter. In addition, the system included a peristaltic pump (Masterflex L/S 7523-60, Vernon Hills, IL), which allowed a continuous movement of prepared MB solutions through the reactor for treatment. This continuous operation design could significantly improve the quantity and capacity of the reactor system, therefore potentially reducing the operation costs and reactor size for commercial applications [149, 157].

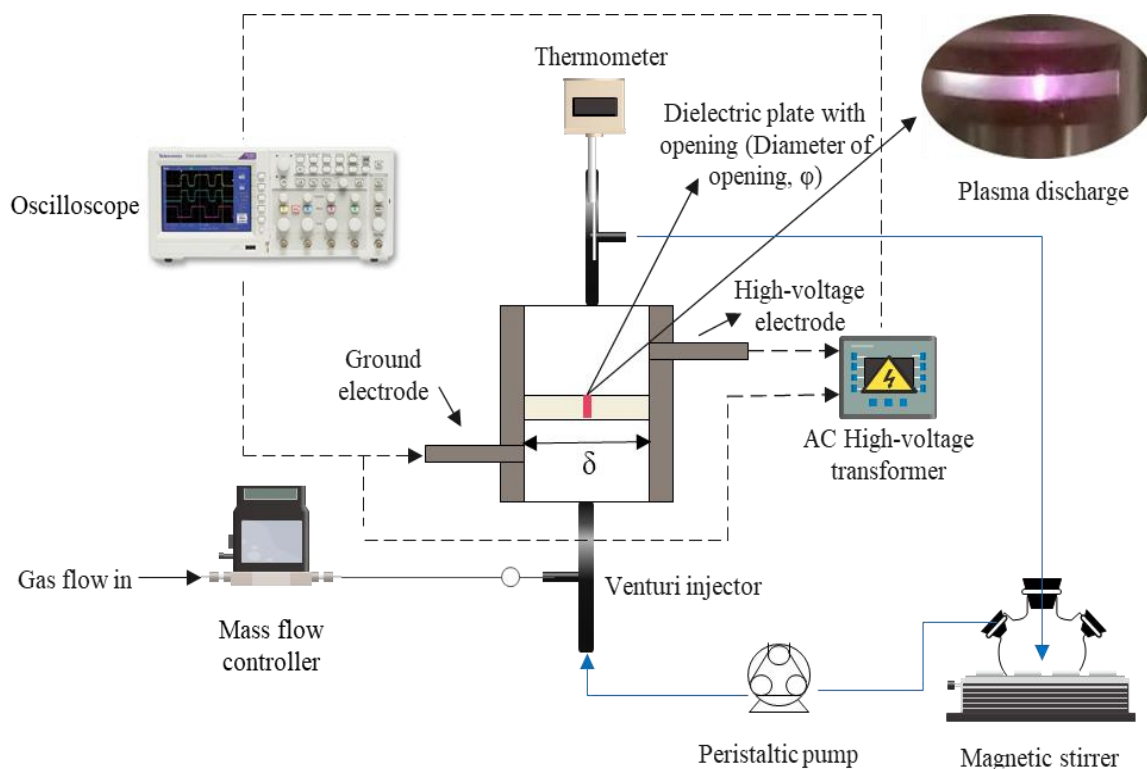


Figure 3.1. Schematic of the novel electrohydraulic discharge reactor system; $\delta = 3.2$ mm, $\phi = 0.8$ mm

3.2.3 Experimental design

Although the design of EHPD could treat wastewater in both continuous circulation and one-pass modes, in this study, the focus was only placed on the continuous flow circulation treatment to evaluate the efficiency of MB degradation. In each experiment, air was used as the carrier gas, which was fed into the reactor through a venturi injector. The air flow rate was controlled by a mass flow instrument. Use of a carrier gas facilitated the plasma discharge and the mass transfer between the plasma active species and water [159]. A total volume of 150 mL MB solution was used for each experimental run. The solution was introduced to a three-neck flask connected to a condenser tube and was pumped through the EHPD reactor through a peristaltic pump for treatment. The treated solution was then directed back to the flask to accomplish a continuous mixing and circulating operation. Once the solution filled the discharge region, the power was turned on, and the voltage and power were adjusted to the same position on the regulator for all the experiments. During the treatment process for each experiment, the power and voltage were found to be in the range

of 250-300 Watt and 2.5-5 kV, respectively. After each experimental run, the reactor system was rinsed twice with deionized water. The initial and final pH and conductivity of MB were measured using conductivity and pH probes with a Hach HQ 440D multi-meter.

To evaluate the MB degradation efficiency of the EHPD reactor, three operational parameters, i.e., liquid flow rate, air flow rate, and initial dye concentration, were chosen to conduct batch experiments. The first batch experiments were to study the effect of liquid flow rate on the MB removal efficiency. Four liquid flow rates were investigated, i.e., 37, 68, 84 and 94 mL/min, corresponding to 25, 50, 75 and 100 rpm on the peristaltic pump. The liquid flow rates were selected based on the manageable range of the system operability and their actual flow rates mentioned above (37, 68, 84 and 94 mL/min), together with the addition of air flow rate and plasma discharge. The selected initial concentration of MB and air flow rate were 20 mg/L and 3 L/min, respectively, based on preliminary trials. The second batch experiments were to study the effect of air flowrate on MB degradation efficiency. Four air flow rates, i.e., 1 L/min, 2 L/min, 3 L/min, and 4 L/min, were investigated under the optimum liquid flow rate determined from the first batch experiments. The initial MB concentration and other parameters such as solution volume and applied voltage were kept unchanged from the first batch experiments. In the third batch experiments, the effect of initial concentrations of MB, i.e., 10 mg/L, 20 mg/L, 50 mg/L, and 100 mg/L, on MB degradation efficiency were evaluated using the optimum liquid and air flowrates from the first and second batch experiments. Similarly, the solution volume and applied voltage were kept constant. A total treatment time of 10 minutes was used for each experiment.

Degradation of MB was monitored at 1 min intervals up to 10 min of EHPD treatment using a UV-vis spectrophotometer (Biotek Synergy HT) at 664 nm. Each experiment was repeated twice and were carried out at atmospheric pressure and ambient temperature. The degradation efficiency of dyes was measured as follows:

$$n(\%) = (C_0 - C) / C_0 * 100 \quad (1)$$

C_0 = initial concentration, C = final concentration.

Chemical oxygen demand (COD) was used to calculate the mineralization percentage of dye. Hach TNTplus Vial Test tubes was used to read COD on a Hach DR3900 spectrophotometer. The COD removal was calculated using the following equation:

$$COD(\%) = (COD_0 - COD_t) / COD_0 * 100 \quad (2)$$

where COD_0 = COD of initial solution and COD_t = COD of the solution at time t .

Hydrogen peroxide (H_2O_2) concentration in plasma treated solution was calculated based on the reaction with titanium sulfate reagent to form pertitanic acid. The concentration of pertitanic acid is directly proportional to the reacted H_2O_2 concentration and it is determined by measuring the absorbance at 407 nm in UV-vis spectrophotometer [160, 161].

The energy consumption for MB degradation was calculated using Eq. 3. The consumption value was expressed as the amount of pollutant converted divided by the energy input required at n % conversion of the pollutant [84]:

$$Y (g/kWh) = (C_0 * V_0 * n\% * 1/100) / Pt \quad (3)$$

where C_0 was the initial concentration of the pollutant in mg/L, V_0 was volume of treated solution in L, n % was degradation efficiency at time t , P was average power dissipated in the discharge (kW), and t was the time (in hour).

3.2.4 Radical scavenging experiments

In order to identify the role of active species produced in EHPD process for MB degradation, ascorbic acid (3 mmol/L), sodium nitrate (3 mmol/L) and 10 mL of 2-propanol diluted (100 mg/L) in distilled water were added to 20 mg/L MB in order to inhibit superoxide radical ($\cdot O_2^-$), aqueous electrons (e^-_{aq}), and hydroxyl radical ($\cdot OH$), respectively. The optimum condition found for combined liquid flow rate and air flow rate was used for all radical scavenging tests to compare with the scavenger-free running condition for the MB degradation. MB degradation efficiency was calculated based on the MB concentration measured with a UV spectrophotometer (Biotek Synergy HT) at 664 nm.

3.2.5 Sample analysis

The degradation product analysis and identification were conducted with an ACQUITY UPLC system coupled with a Waters Xevo TQ mass spectrometer and a tandem quadrupole mass spectrometer for LC-MS/MS quantification applications using single ion reaction monitoring (SIR) or multiple reaction monitoring (MRM) methods. The column used was 1 mm i.d. x 150 mm length packed with 5 μ m phenyl-hexyl packing from Phenomenex, Torrance, CA. The method referred to in this study was similar to that used by Rauf et al. [162], but with slight modifications. The mass spectroscopy (MS) system was composed of an electrospray ionization source in a multiple reaction monitoring mode. The

detector was a low-noise, off-axis, and long-life photomultiplier detector. The signal received from the detector was recorded by the MassLynx software. The mobile phases for the method consisted of two solvents, A and B. Mobile phase A was made using water and mobile phase B was made of 20 % acetonitrile and 80 % ammonium acetate (0.1 M). The gradient was from 20 % to 80 % in 25 min with a flow rate of 0.060 mL/min and an injection volume of 4 μ L.

The inorganic ions in the degradation products were determined using a Dionex Ion Analyzer (Dionex, Sunnyvale, CA) with a GP40 gradient pump attached, an ED40 electrochemical detector, and an AS40 autosampler. 100 mM sodium hydroxide (NaOH) was used as the mobile phase and the injection volume was about 20 μ L. The anion suppressor current was set to 300 mA and the detector stabilizer temperature was set at 30 °C. The inorganic ions check standard (CertiPrep) was used as reference to compare the products formed in the ion chromatography trace. The concentration of each inorganic ion present in the aqueous media was calculated and presented.

3.3 Results and Discussion

3.3.1 Effects of process operating parameters on the MB degradation

3.3.1.1 Effect of liquid flow rate

Under all the preset operational conditions based on the experimental design, stable electrical discharge was observed at the dielectric opening in the middle of the reactor where the continuous flow of MB solution is passing throughout the treatment period, as shown in Fig. 1. It was reported that, in the electrohydraulic discharge reactors with moving liquid, the liquid flow rate often influenced the degradation process and energy yield [158]. As seen in the Fig. 3.2, the MB initial concentration of 20 mg/L degraded very rapidly with plasma discharge at different liquid flow rates with 3 L/min air injection. All the liquid flow rates showed complete MB degradation within 10 min of plasma treatment. Finally, all the liquid flow rates showed almost complete MB degradation within 7 min of EHPD treatment.

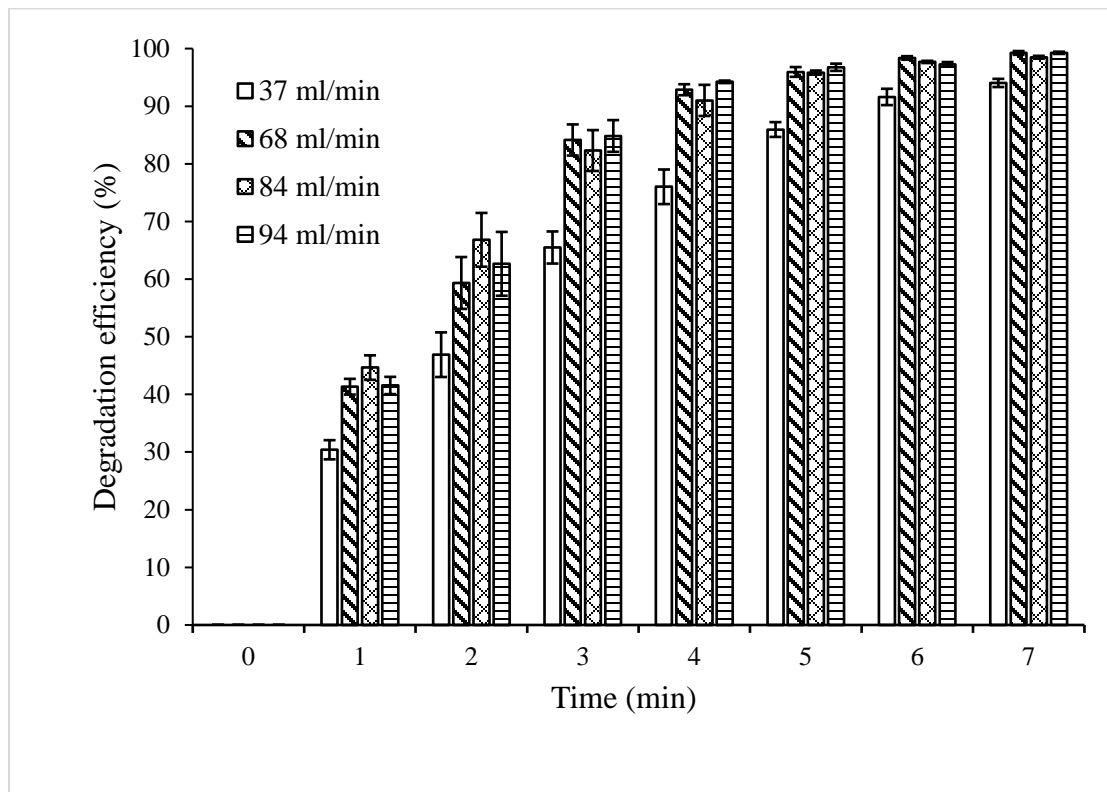


Figure 3.2. Degradation efficiency of MB (20 mg/L) using plasma at different liquid flow rates

The MB degradation efficiency was not substantially affected by the liquid flowrate (except 37 mL/min), because the total contact and reaction time of MB molecules with plasma discharge in the continuous circular flow was the same for all liquid flow rates, assuming the discharging channel where the reactive species were produced was the thickness of the dielectric plate. However, the trend was not consistent at the shorter treatment time. At the low liquid flow rate (37 mL/min), the degradation rate was slightly lower at first compared to those of the other flow rates.

The reason for this might be because the liquid flow rate needs to be high enough to maintain a high treatment frequency and power delivery, and to achieve an effective utilization of the reactive species produced with the high air flow rate. That said, the overall MB removal efficiency clearly indicated that the EHPD process could enhance the degradation activity by effectively transporting charge carriers to generate $\cdot\text{OH}$ radicals and other reactive species [25, 84, 152, 153, 155].

There were only a few reports available on the influence of liquid flow rate on the degradation process. For instance, one study reported that the phenol degradation rate was not affected by a faster water flow rate in coaxial falling water film reactors with corona discharge [163]. Another study reported that the energy yield of methylene blue degradation decreased with increase in solution flow rate in a pulsed DBD falling water film reactor [164]. The same behaviors were also observed in this study. Certainly, more research is required to evaluate the influence of liquid flow rate on MB degradation by the electric discharges in liquid media. Based on the results from this study, 68 mL/min (50 rpm) appeared to be the best flowrate for this reactor, as it achieved the highest degradation compared to other liquid flow rates and good energy yield at 50 % conversion with $Y_{50} = 0.27$ g/kWh (Table 1). Therefore, 68 mL/min (50 rpm) was used as the liquid flow rate for all other batch experiments.

3.3.1.2 Effect of air flow rate

Four air flow rates (1, 2, 3, and 4 L/min) were investigated at the liquid flow rate controlled at a pump speed of 50 rpm under the same parameters as in the first batch (initial concentration = 20 mg/L, solution volume = 150 ml). The actual liquid flow rate in this situation could slightly vary with the influence of different air flow rates and plasma discharge. Corresponding to the air flow rates of 1, 2, 3, and 4 L/min, the liquid flow rate of the peristaltic pump was 86, 78, 68, and 60 mL/min, respectively. As shown in Fig. 3.3, the concentration of MB decreased quickly with different air flow rates within 10 min of treatment. More than 95 % of dye was degraded within 5 min by different air flow rates, which was mainly due to the increasing effect of the active species [165, 166]. The fact that all airflow rates achieved nearly 100 % degradation rate clearly indicated that the air/gas flow rate in plasma treatment could effectively influence MB degradation. However, the results did not show any significant difference in MB degradation efficiency among different air flow rates used. This was likely due to the sufficient active species that were produced even at the lowest air flow rate employed in this study to degrade MB at an initial concentration of 20 mg/L. As such, the increase in air flow rate did not cause noticeable changes in MB removal rate. However, increasing the initial dye concentration appeared to have an effect on the MB degradation efficiency under different air flow rates as smaller air flow rates showed lower degradation efficiencies. This same phenomenon was reported by Reddy et al. [84].

Based on the results, an optimal airflow rate of 3 L/min was determined. However, it was observed that any air flow rate beyond 3 L/min sometimes caused fluctuations in the liquid flow or sparking effect during discharge, potentially leading to a system shutdown. It was thus suggested that the air flow rate should be kept around 2 L/min to lower the treatment cost and ensure a satisfactory removal efficiency for MB concentration up to 100 mg/L.

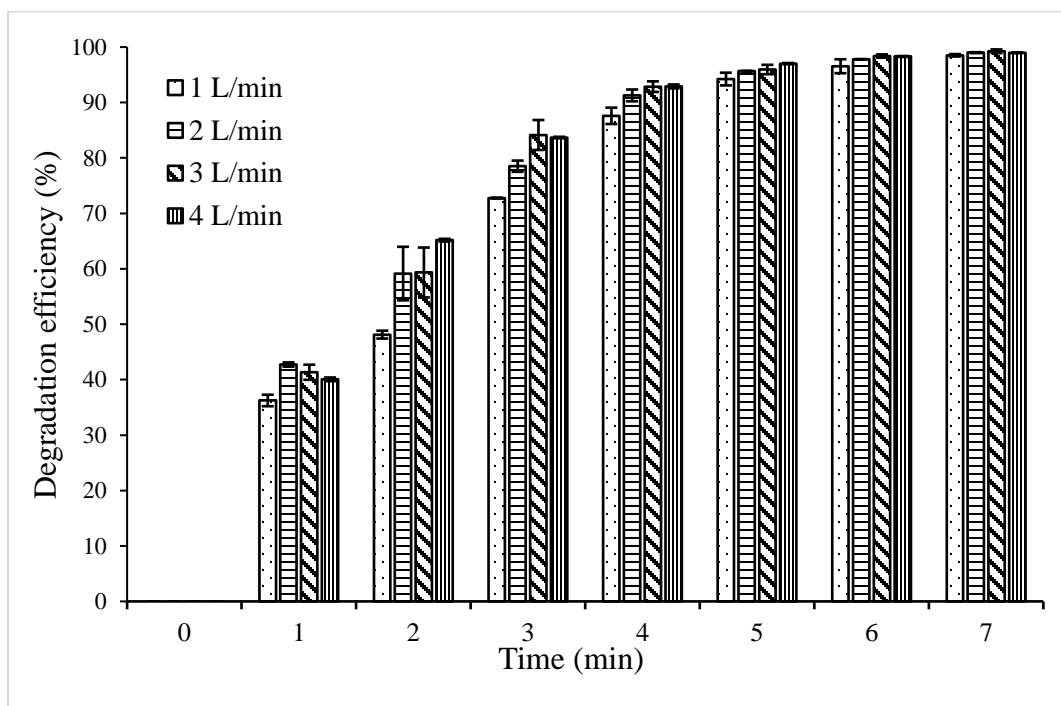


Figure 3.3. Degradation efficiency of MB (20 mg/L) by EHPD at different air flow rates

3.3.1.3 Effect of initial MB concentration in solution

Fig. 3.4 presented the effect of initial MB concentrations (10, 20, 50, and 100 mg/L) on MB degradation by plasma treatment with 68 mL/min liquid flow rate and 3 L/min airflow rate. The 10 mg/L initial concentration showed a 100% MB degradation efficiency after 7 min of treatment, followed by 20 mg/L (99.94%), 50 mg/L (99.67%), and 100 mg/L (97.69%), respectively, within 10 min of treatment time. It appeared that the initial MB concentration had an effect on the degradation rate by the EHPD process operated under the given parameters because the MB degradation efficiency at lower concentrations was slightly higher than that at higher concentrations. Similar phenomenon was observed and reported by various researchers that degradation efficiency decreased with increase in initial MB concentrations [84, 167]. In addition, Wu et al. [155] studied the MB degradation by

dielectric barrier discharge plasma treatment and also observed that MB degradation efficiency was higher at low MB concentrations and would decrease at higher MB concentrations because the amount of plasma active species formed in the discharge process was maintained at a specific concentration level for the constant energy input. In this study, since the results showed good MB degradation efficiency at different initial concentrations, it could be concluded that the novel EHPD reactor system was an effective process for MB degradation.

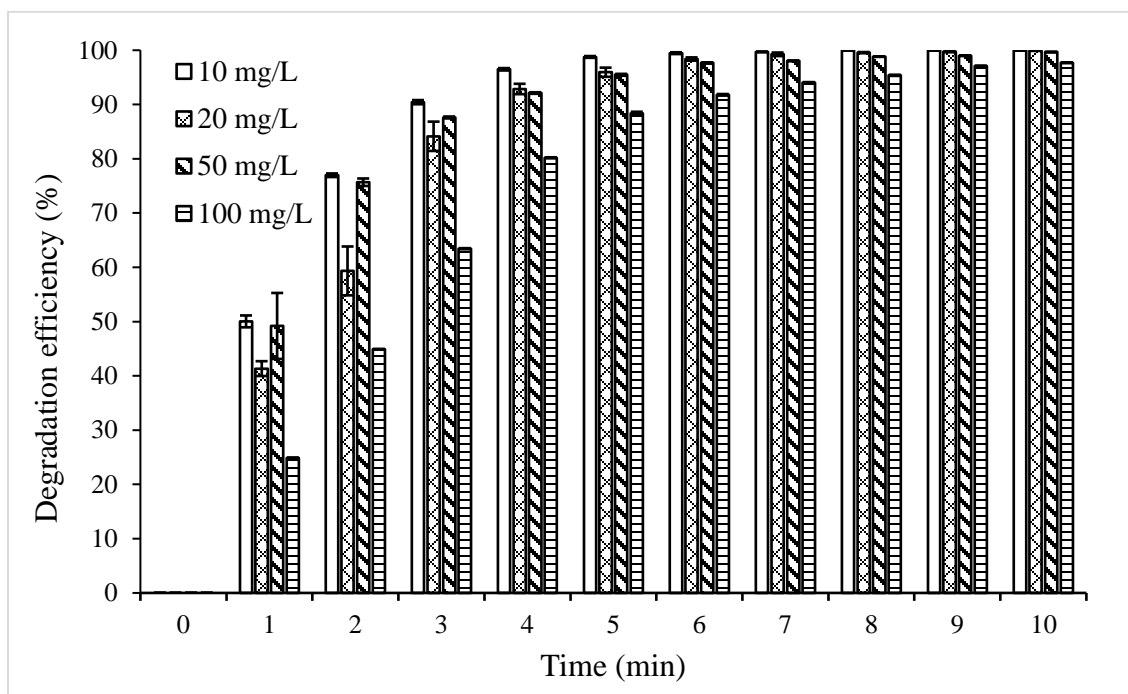


Figure 3.4. Degradation efficiency by EHPD at different initial concentrations under 68 mL/min and 3 L/min

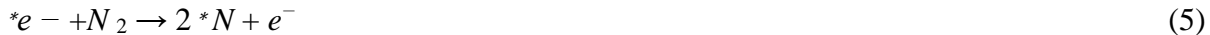
3.3.2 Mineralization of MB and water quality change during EHPD process

To evaluate the mineralization rate and change of water quality during the EHPD treatment, chemical oxygen demand (COD) as well as physicochemical attributes of the initial and treated solutions, including H_2O_2 , inorganic ions (nitrate, chloride and sulfate), pH and electrical conductivity were investigated (Figs.3.5 and 3.6). The measured COD concentration was adjusted based on the theoretical hydrogen peroxide interference to the COD measurement (470.6 mg of COD as O_2 per 1000mg H_2O_2 [168]. The COD in 100 mg/L MB solution was determined as 357.5 mg/L and decreased rapidly in the treatment

process with liquid flow rate at 68 mL/min, and air flow rate at 3 L/min. At 5 min and 10 min, the COD level reached down to 51.7 mg/L and 26.7 mg/L, signified a COD removal of 85.5% and 92.5%, respectively, which should be approximately equivalent to the removal rate of organic matter and the mineralization rate. The MB mineralization rate was slightly lower than the overall degradation efficiency of 98.7%, which implied that smaller organic molecules from MB degradation still present in the treated solutions. However, the COD removal obtained in this study during 10 min treatment for 100 mg/L initial MB concentration was much faster and higher compared to the results in literature of plasma alone and hybrid systems [84, 153, 155, 166].

Another major change in the water quality observed with MB treatment is the production of H_2O_2 (Fig. 3.5). H_2O_2 is a common stable compound attributed to the quenching of short-lived $\cdot OH$ radicals generated with plasma water/wastewater treatment, reported by several studies [149, 169, 170]. In this study, H_2O_2 concentration gradually increased with time and arrived 25.44 mg/L at 1 min, 66.18 mg/L at 5 min and 89.16 mg/L at 10 min. Thus, high concentration of H_2O_2 shows that large amount of hydroxyl radicals generated with air EHPD are excessive and not consumed by the oxidation of MB and nitrogen active species produced with plasma discharge. Several major inorganic ions were detected in the treated MB solution due to MB mineralization and/or plasma discharge. Changes in concentrations of chloride, sulfate, and nitrate were shown in Fig. 3.5. Chloride and sulfate presented low concentrations, which were produced with bond-breaking of MB, while nitrates showed a relatively high concentration of 43.76 mg/L at 1 min, 188.02 mg/L at 5 min and 223.74 mg/L at 10 min. The elevation of nitrate concentration with treatment time was attributed to not only the mineralization of MB molecule, but also the fixation of nitrogen in the air.

As the air contains 78.09% of nitrogen (N_2), 20.95% of oxygen (O_2), 0.93% of argon, and other small traces of gases [171], NO and NO_2 (Eq. 4, 5, 6, 7, 8) could be produced from the air due to nitrogen atoms competing with the oxygen atoms. These species can react with water molecules and produce NO_2^- and NO_3^- (Eq. 9). NO_2^- was not detected in our experiments possibly due to high oxidation capacity of 3 L/min air activated EHPD that converted all nitrogen to its highest valence.



These formed ions also explained the increasing acidity in the solution. Research on plasma activated water has reported similar results in nitrogen fixation effect by plasma discharge and these results indicated that the treated dye wastewater from the EHPD process was potentially used as a fertilizer [172, 173]. If used for drinking water, the concern of high nitrate concentration could be addressed by substituting the gas source of air with pure oxygen gas.

The initial pH and conductivity of MB solution at 10-100 mg/ L ranged in 5.3- 4.9 and 5.0- 36.7 $\mu\text{S}/\text{cm}$ (25 °C), respectively. Final pH values after 10-min EHPD treatment for all tested parameters for varying liquid flow rates, air flow rates, and initial MB concentration showed a big fall from the initial point but little variation among different operational conditions ranging from 2.5 to 2.7, apparently due to the acids production discussed earlier. On the other hand, the final conductivity leaped tremendously to 1000-1750 $\mu\text{S}/\text{cm}$ and showed a clear decreasing trend with increasing liquid flow rates, also increased with higher air flow rate and higher initial MB concentration (Fig. 3.6 (a)- (c)). This same phenomenon, i.e., decrease in pH and increase in electrical conductivity, was observed by many other researchers [33, 167]. For instance, Magureanu et al. [33] reported that after 15 min of pulsed corona discharge on MB degradation, the pH was decreased to 3.2 and the conductivity was increased to 714 mS/cm. Evidence from literature showed that pH and conductivity were strongly related to electrical discharges in liquid media [158, 174, 175].

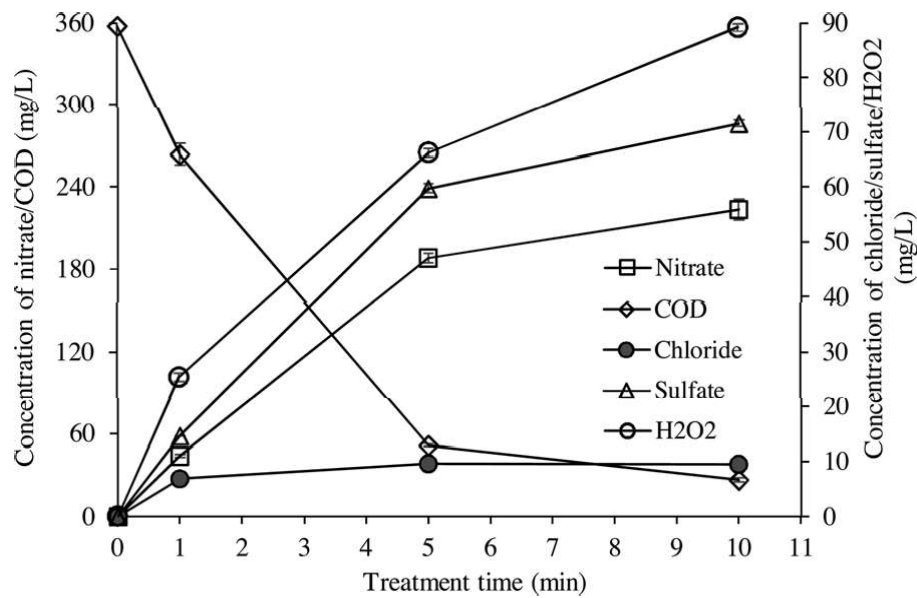
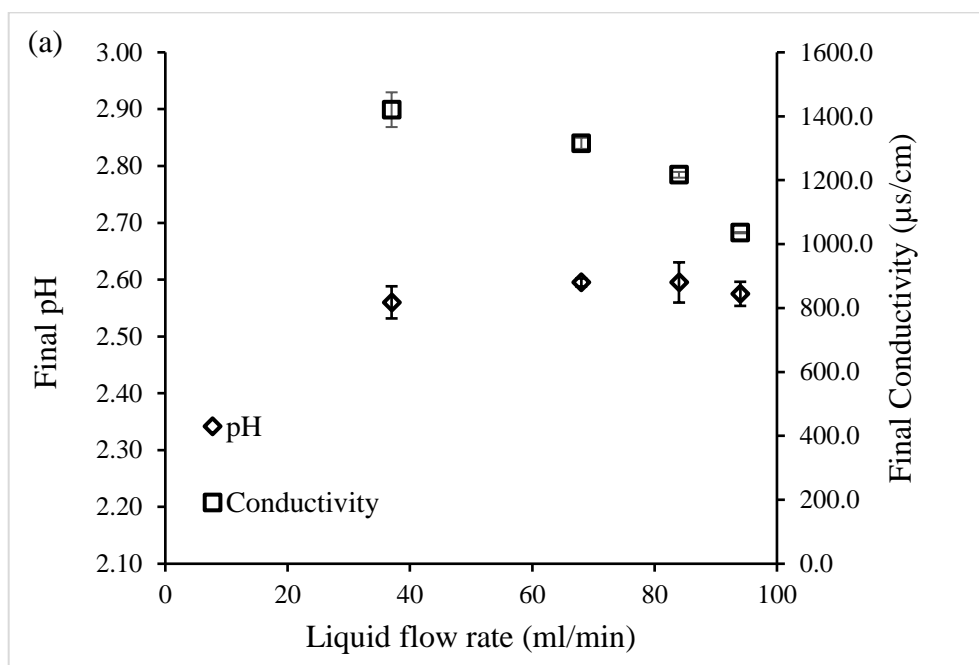


Figure 3.5. Changes of COD, H₂O₂ and inorganic ions during 10 min EHPD treatment time (liquid flow rate = 68 ml/min, and air flowrate = 3 L/min)



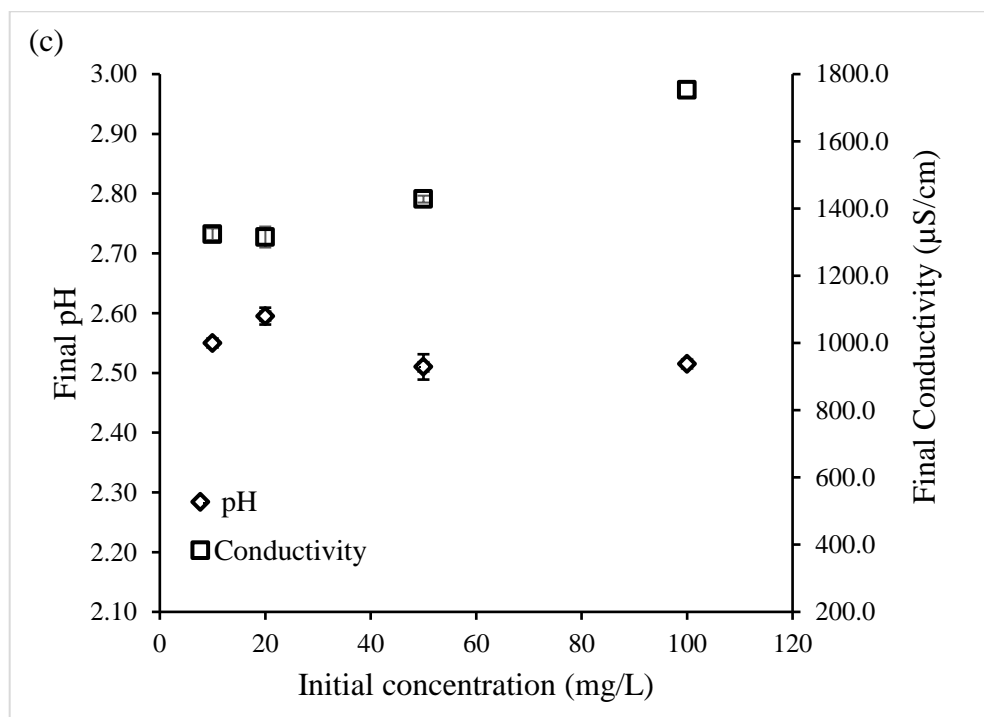
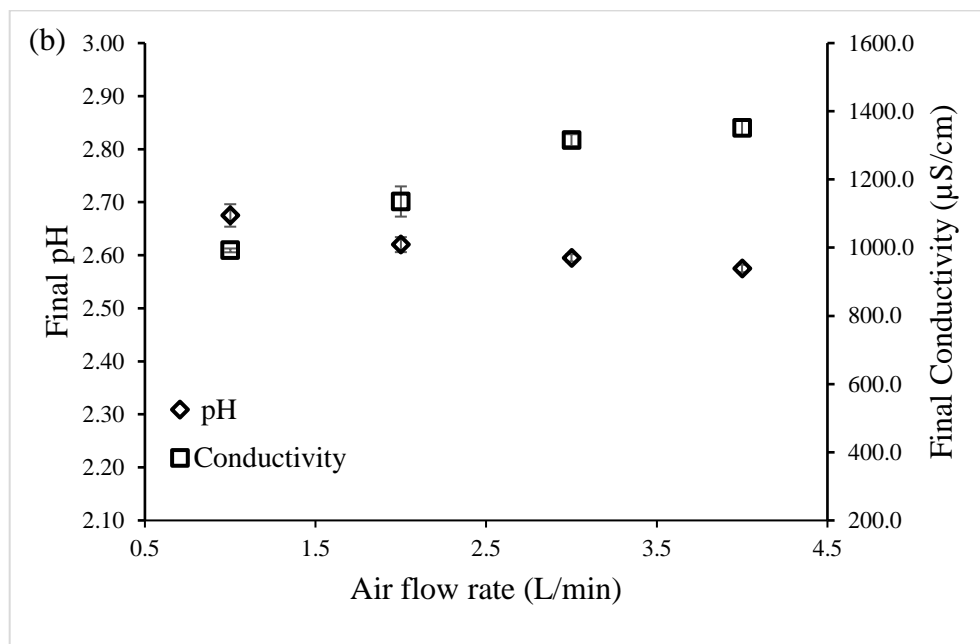


Figure 3.6. Final pH and conductivity at (a) different liquid flow rates; (b) different air flow rates; and (c) different initial MB concentrations after 10-minute treatment

3.3.3 Methylene blue degradation kinetics

Degradation kinetics were investigated to further confirm the effect of different parameters on the MB degradation efficiency. The degradation reaction process was fitted to a pseudo-first-order kinetics by Eq. 10 [31].

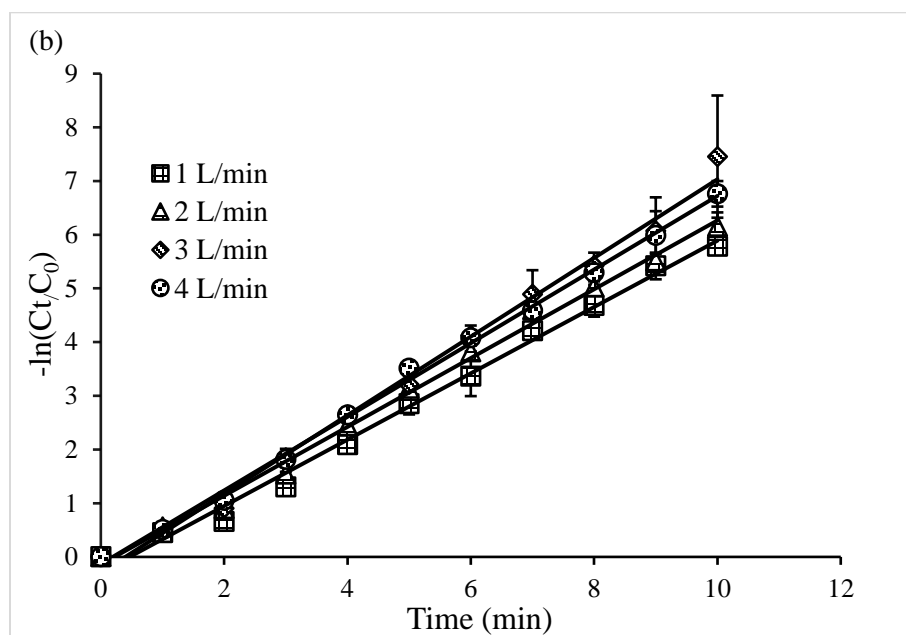
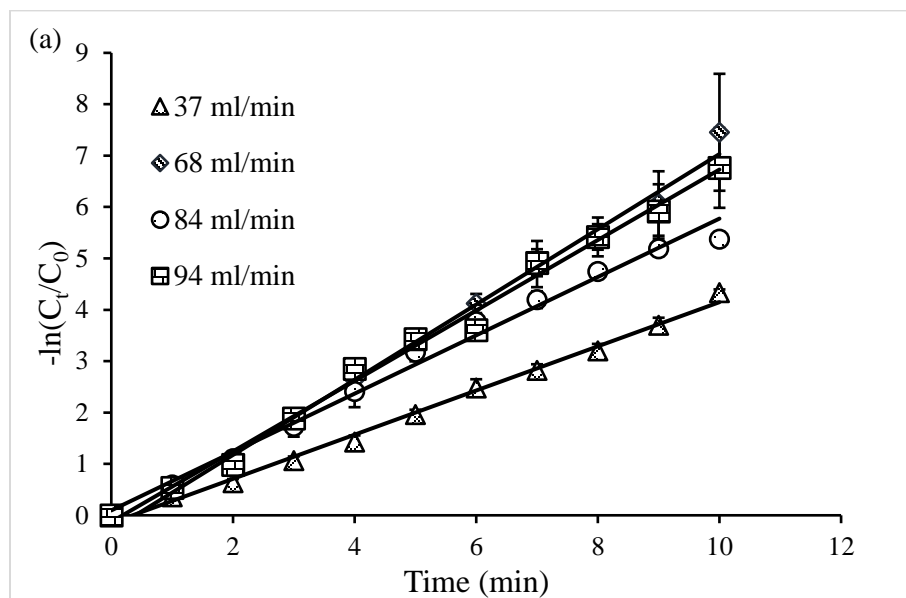
$$-\ln (C_t/C_0) = kt \quad (10)$$

where C_t , was concentration of MB for a given treatment time, C_0 was the initial concentration, and k was the first-order rate constant (min^{-1}), respectively.

As shown in Fig. 3.7 (a), (b), and (c), the correlation coefficients were obtained using linear regression by plotting $-\ln (C_t/C_0) = kt$ at different liquid flow rates, air flow rates, and initial MB concentrations. The correlation coefficients were above 0.98 for all the batch experiments, clearly indicating that the first order kinetic model agreed with the experimental data on the MB degradation. The results of the first order kinetic constant for degradation of MB at different operational parameters were presented in Table 3.1.

Table 3.1. First order kinetic constant of MB degradation at different operational parameters

Operational parameters	Rate constant, K (min^{-1})	R ² value	Half-life, $t_{1/2}$ (min)
<i>Liquid flow Rate (mL/min)</i>			
37	0.4299	0.9947	1.61
68	0.7322	0.9923	0.95
84	0.5679	0.9902	1.22
94	0.6857	0.9926	1.01
<i>Air flow rate (L/min)</i>			
1	0.6177	0.9922	1.12
2	0.6408	0.9944	1.08
3	0.7322	0.9923	0.95
4	0.6855	0.9974	1.01
<i>Initial Concentration (mg/L)</i>			
10	0.8676	0.9957	0.80
20	0.7322	0.9923	0.95
50	0.5293	0.9836	1.31
100	0.3979	0.9909	1.74



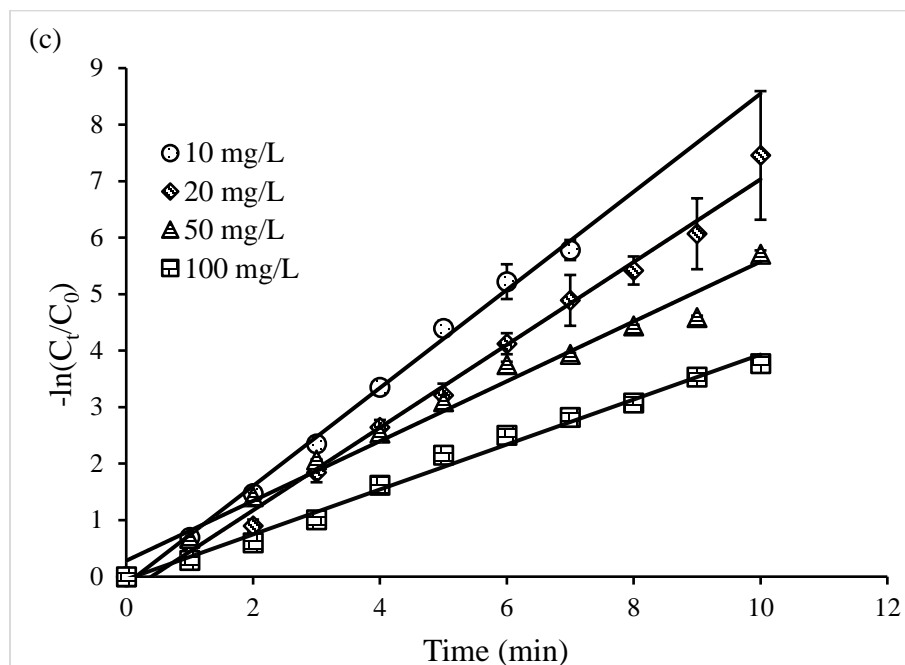


Figure 3.7. First order kinetics of MB degradation (a) at different liquid flow rates; (b) at different air flow rates; and (c) at different initial MB concentrations

3.3.4 Role of reactive species produced in electrohydraulic plasma for MB degradation

Operating at 20 mg/L MB initial concentration under the optimal condition of liquid flow rate of 68 ml/min and flow rate of 3 L/min air, the addition of radical scavengers for aqueous electrons, superoxide, and hydroxyl radicals in the system had shown different levels of decreases in MB degradation efficiency as compared to the scavenger-free trials. Degradation kinetics were investigated as shown in the fig. 3.8a to further confirm the effect of radical scavengers on the MB degradation efficiency. With addition of NaNO_3 , the degradation rate constant was 0.4796. The MB degradation was affected during the first few minutes and caught up after that, showed that the hydrated electrons played a minimal role in the EHPD process for MB degradation with 10 min treatment. On the other hand, with the addition of ascorbic acid, the degradation rate constant was 0.4219. It showed that MB decreased slightly than that of NaNO_3 , indicating minimal involvement of the $\cdot\text{O}_2$ species in MB degradation. In contrast, the MB degradation rate was significantly affected by 2-propanol during the entire treatment, the degradation rate constant was 0.1459, clearly

indicating that production of $\cdot\text{OH}$ radicals among different reactive species in the EHPD process played the major role for MB degradation.

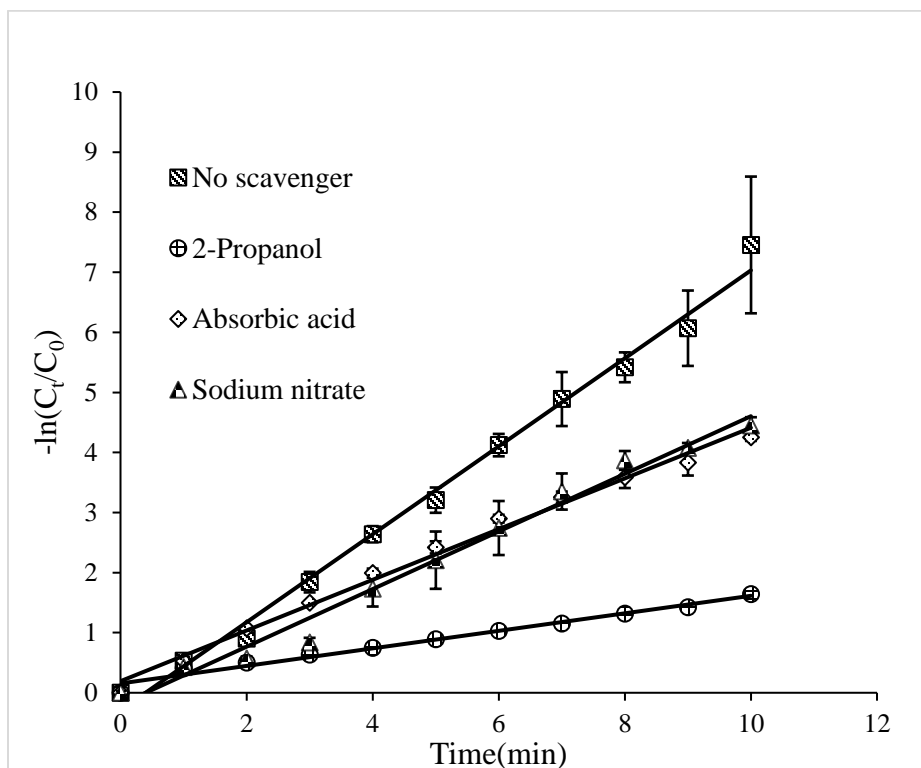


Figure 3.8. Role of active species by EHPD at 20 mg/L MB initial concentration under 68 ml/min and 3 L/min

3.3.5 Energy yield of the MB degradation by EHPD

The energy yield (g/kWh) of the EHPD reactor during the MB degradation process was calculated using Eq. (2) at 50% degradation rate and the input power for all the three operational parameters (Table 2). Based on the energy yield calculation, for 50% MB degradation, the highest energy yield was 0.27 g/kWh at 68 mL/min. For air flow rate, the highest energy yield was 0.27 g/kWh at 2 L/min and 3 L/min. And for the initial MB concentration, the highest energy yield was 0.81 g/kWh at 100 mg/L. It seemed that the energy yield decreased as the degradation efficiency and treatment time increased. The calculated results were obviously in line with the experiments results, which showed decreases in energy yield with the increase in treatment time for all the experiments. The reason was due to the low collision probability between plasma reactive species and MB molecules [84, 155]. Also, the energy yield was proportional with the initial dye

concentration because of more reactant molecules present in the solution influenced by the discharge [22]. As the MB degradation efficiency increased with respect to the treatment time, it led to a reduction in MB removal per unit of energy consumption over a longer treatment time.

Table 3.2. Energy yield at 50% MB degradation for different operational parameters of EHPD system

Operational Parameters	Time for 50% degradation (min)	Initial concentration (mg/L)	Power (kW)	Energy Yield (g/kWh)
<i>Liquid flow rate (mL/min)</i>				
37	2.15	20	0.251	0.17
68	1.25	20	0.267	0.27
84	1.2	20	0.283	0.26
94	1.25	20	0.285	0.25
<i>Air flow rate (L/min)</i>				
1	2.1	20	0.267	0.16
2	1.25	20	0.270	0.26
3	1.25	20	0.267	0.27
4	1.3	20	0.275	0.25
<i>MB Concentration (mg/L)</i>				
10	1	10	0.270	0.16
20	1.25	20	0.267	0.27
50	1.05	50	0.267	0.80
100	2.25	100	0.245	0.81

3.3.6 Comparison of novel electrohydraulic plasma discharge with existing processes

To further investigate the efficiency of the novel electrohydraulic plasma discharge process, a comparison was made between the EHPD in this study with other plasma treatment methods. Honestly, it was sometimes difficult to make a comparison about the efficiency and performance among the plasma processes because of the different reactor types, experimental conditions, and the wide variety of pollutants used for degradation [153]. Therefore, comparisons presented in this paper only focused on the performance of different nonthermal plasma reactors on MB degradation (Table 3.3) based on similar parameters such as degradation efficiencies and energy yield.

Table 3.3. Comparison of the novel EHPD on MB degradation with other nonthermal plasma processes

Methods	Initial concentration (mg/L)	Time (min)	Degradation efficiency (n%)	Energy Yield (g/kWh)	Reference
Continuous flow EHPD	100	10	97.7	0.37	This study
	20	6	98.5	0.14	This study
Double chamber-DBD in air	100	40	67.14	0.14	[153]
Argon plasma jet	50	40	72	0.4	[25]
DBD with Fe ²⁺	100	20	90.1	16.2 (discharge power 1.35W)	[84]
DBD with Argon	50	25	100	0.4	[22]
DBD point-to-plate electrical discharge in O ₂	20	20	81.36	0.024	[174]
Argon microwave plasma jet	100	10	50	0.018	[176]
DBD plasma	50	40	63.8	29.9 (discharge power 0.46W)	[164]
DC corona discharge	50	180	90	1.211	[167]

It could be concluded that the novel continuous-flow electrohydraulic plasma discharge process showed a faster degradation and relatively high energy yield compared to other nonthermal plasma reactor designs in the literature. Despite that a few methods reported a high energy yield, those reactor designs were not considered better than the EHPD process due to much longer treatment time and/or lower removal efficiency, according to the data collected in Table 3.3. Besides, the continuous flow EHPD provided flexibility and practicality in terms of potential development for mass treatment of wastewater.

3.3.7 Degradation mechanism of methylene blue by EHPD

The possible degradation pathway of MB was studied using LC-MS, and the total ion chromatogram (TIC) was shown in Fig. 3.9. The MB molecules at different treatment times

were broken down because of the electric plasma discharge in the MB solution. After the end of the treatment time (10 min), the peaks of MB were not observed, clearly indicating that it was completely degraded. The retention time for initial MB started to decrease with the discharge and new peaks (byproducts) were formed at the shorter retention times. The possible formation of intermediates and final products were detected by Mass Spectroscopy and the potential pathway was shown in Fig. 3.10.

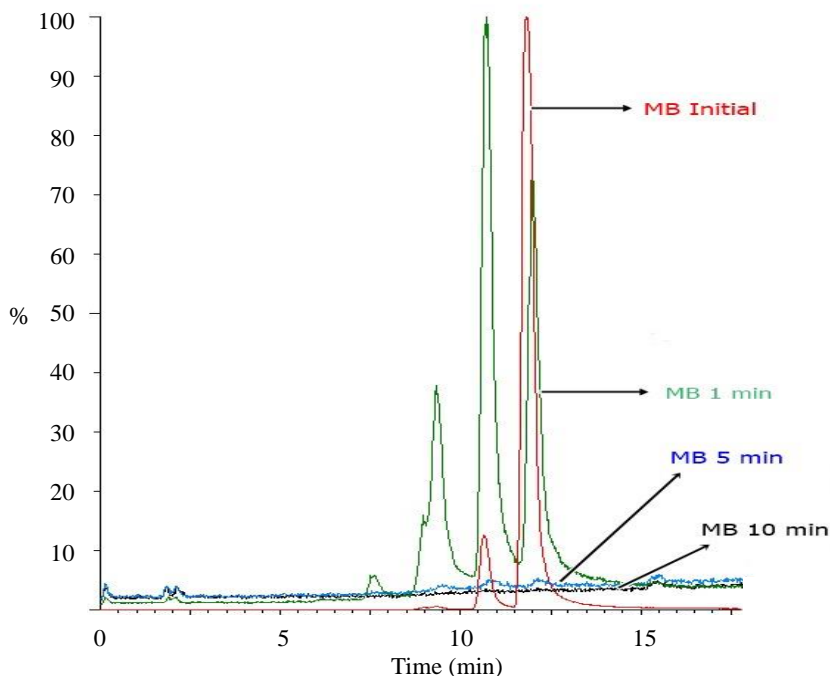


Figure 3.9. Total ion chromatogram (TIC) of MB degradation at different treatment times ($C_0 = 20$ mg/L, liquid flow rate = 68 ml/min, and air flowrate = 3 L/min)

When MB was dissolved in water, the mass spectroscopy observed an MB peak at m/z 284 due to the Cl^- being ionized and entering the detached state, and the MB cation was isomerized into $C_6H_{18}N_3S$ [153, 165]. When MB was degraded by the plasma, the presence of hydroxyl radicals ($\cdot OH$) decomposed MB molecules into different products such as Azure B (m/z 270), Azure A (m/z 256), Azure C (m/z 242) and Thionin (m/z 228). These products were formed mainly due to demethylation and hydroxylation from plasma and could further be reduced to aromatic ring compounds, which later broke down to various fragments (non-aromatic compounds) and reacted with other reactive species. These intermediate products were eventually mineralized into inorganic compounds such as CO_2 , H_2O , SO_4^{2-} and NO_3^- [92, 155, 165, 166, 177].

Many previous authors have suggested the similar possible pathway. Benetoli et al. [92] proposed that MB degradation took place due to two main reaction pathways in the non-thermal plasma reactor, 1) high energy electron impact and 2) successive hydroxylation addition to the benzene ring of the MB molecule. They also observed that demethylated MB molecules was blue-shifted in the UV–vis absorption peak at 664 nm. Huang et al. [165] proposed an MB degradation mechanism based on the bond dissociation energy (BDE) theory for the dielectric barrier discharge (DBD) reactor. They suggested that it was easier for the chemical bonds to break with low bond dissociation energy. They also detected phenyl thiophene during the discharge process at the peak intensity of m/z 138. Due to the production of ozone and hydroxyl radicals from the discharge, the MB molecular structure was oxidized and ultimately transformed into inorganic ions such as CO_2 , H_2O , SO_4^{2-} and NO_3^- .

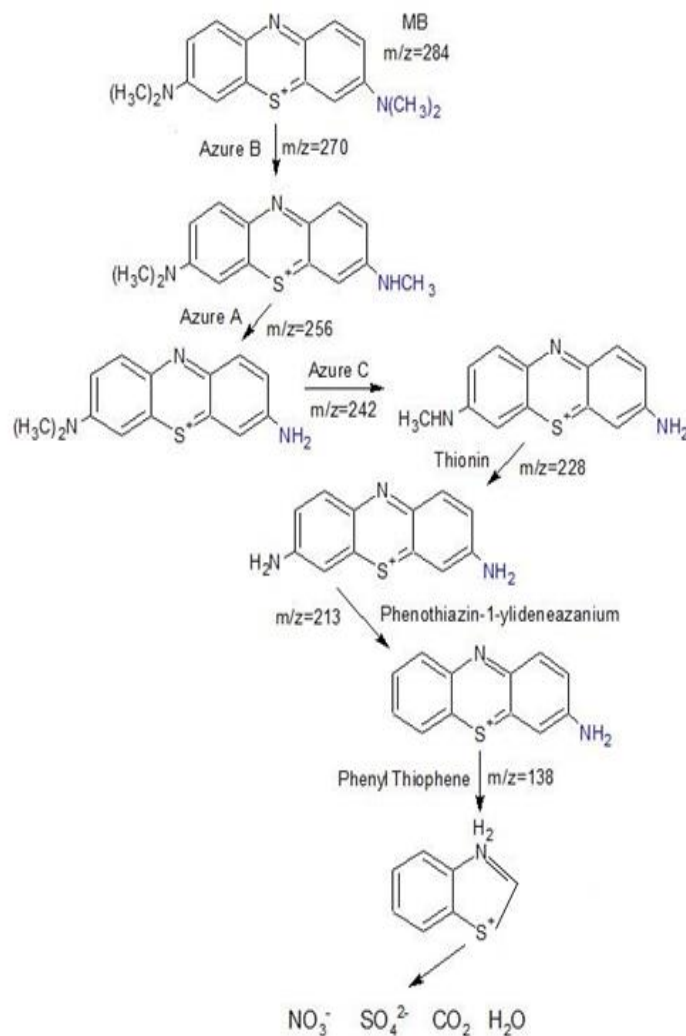


Figure 3.10. Degradation pathway of MB molecule

3.4. Conclusions

The results in this study concluded that the novel continuous-flow electrohydraulic plasma (EHPD) reactor developed was a highly efficient method for treating dye wastewater. A nearly complete degradation of methylene blue (MB) was achieved within 10 min of treatment time. The optimum running liquid and air flow rates were 68 mL/min and 3 L/min, showed almost 100% degradation and a better energy yield ($Y_{50}= 0.27$ g/kWh) were achieved for the initial MB concentration of 20 mg/L. Increasing initial MB concentrations could decrease degradation rates. However, almost 90 % of MB was degraded after only 5 min of treatment even at higher concentrations. Decrease in pH and increase in conductivity in the solution were observed after 10-min electrical discharge treatment for all experimental cases.

MB degradation followed the first order kinetics and the energy yield at 50% conversion was ranging from 0.16 g/kWh to 0.81 g/kWh for different operating parameters. The free radical scavenging experiment showed that hydroxyl radicals played a very important role in MB degradation. Demethylation and hydroxylation were the two main reactions found in degrading MB molecules. In addition, COD removal was 92.5% after 10 min treatment for 100 mg/L initial MB concentration and ion chromatography found that the concentration of nitrates was the highest in the aqueous solution after plasma treatment. Comparison with other plasma methods indicated that the novel continuous flow EHPD reactor examined in this study was a robust and highly efficient process for MB degradation and mineralization. Further study on this novel plasma reactor for wastewater treatment is warranted to develop this technology for commercial applications.

CHAPTER 4 OPTIMIZATION AND MODELING OF ARGON ACTIVATED ELECTROHYDRAULIC PLASMA DISCHARGE PROCESS FOR P- NITROPHENOL DEGRADATION

4.1 Introduction

Currently, among the existing advanced oxidation processes (AOPs), electrical plasma discharge is widely employed for wastewater treatment. Electrical plasma discharge is one of the most efficient technology because of its inimitable characteristics of producing reactive oxygen species (ROS) and reactive nitrogen species (RNS) without the need of any chemicals or external light source for organic pollutant degradation [158]. When the electrical plasma discharge happens in liquid-gas interaction, both physical and chemical effects are involved. The physical effects such as ultraviolet (UV) radiation, shock waves and cavitation effects, whereas the chemical effects include the formation of reactive species and oxidation/reduction of organic pollutants [159]. Both physical and chemical effects of plasma play an important role in the degradation of organic pollutants.

p-Nitrophenol (p-NP) is one of the most widely used chemicals in pesticides, explosives, dyes, herbicides, etc. [16, 17, 23, 178, 179]. However, p-NP has a complex lipophilic structure and can easily bioaccumulate making it very difficult to degrade by conventional biological treatment processes when released into environment. Moreover, toxicology studies on p-NP showed potential mutagenicity and toxicity and thus it is listed as one of the top priority pollutants by USEPA [21, 180, 181]. There are few studies that have been investigated for p-NP water treatment using plasma technology. K. Shang et al. [91] reported the degradation of p-NP by DBD plasma in the presence of persulfate (PS) and Fe^{2+} . Results showed that PS can be synergistically activated by DBD plasma and a small quantity of Fe^{2+} . The degradation efficiency of p-NP reached 34.8% by 50 min plasma treatment alone at 17 kV for initial concentration of 5 mg/L p-NP, and with an addition of 36 μM Fe^{2+} and 2.5 mM PS in p-NP solution increased the degradation efficiency to 81.1%. The energy yield for plasma alone was 99.4 mg/kWh and with Plasma/PS/ Fe^{2+} was 229.5 mg/kWh. The radical scavenging experiment showed $\cdot\text{OH}$ and $\text{SO}_4\cdot^-$ radicals were attributed in degradation of p-NP. In another study, reported by C. Zhao et al. [179], a microwave atmospheric pressure plasma jet to degrade p-NP in wastewater. Completed degradation of p-NP with an initial concentration of 100 mg/L was removed in 12 min of treatment. TOC removal

efficiency was 57.6% and the energy yield was 0.12 g/kWh. However, these studies vary greatly in discharge types and reactor size used, as well as the energy yield and treatment time.

In this study, argon (Ar) activated electrohydraulic plasma discharge was used for the degradation of p-NP in water. The influence of operation parameters such as pH, gas flowrate, applied power and persulfate concentration on p-NP degradation were investigated. It is difficult to determine the optimal conditions by conventional methods. To overcome the limitations of conventional methods, statistically experiment design such as fractional factorial design and Response Surface Methodology (RSM) was used. A 2^{4-1} factorial design was used to evaluate the relative importance of various factors that influence the plasma degradation of p-NP. The main purpose of using this method is to identify significant factors [99, 182]. To further analyze the significant factors, a standard Response Surface Methodology (RSM) called central composite design (CCD) was used for the experimental optimization. With RSM design, various variables and their interactions can be tested simultaneously with minimum experimental trails based on the factorial design. CCD is an effective tool for fitting quadratic surface and to determine optimum parameters of different process variables with very less experimental trails [118, 119]. Optical emission spectroscopy and a radical scavenging experiment was conducted to determine the role of active species involved. Moreover, UPLC-MS/MS was used to identify the intermediates of p-NP and determine the degradation pathway.

4.2 Methods and Materials

4.2.1 Materials

p-Nitrophenol purchased from TCI chemicals Pvt. Ltd. was used as the target pollutant. Other chemicals such as ascorbic acid, 2-propanol (C_3H_8O) and sodium nitrate ($NaNO_3$), potassium persulfate and sodium sulfate were purchased from Fisher Scientific (Eugene, OR).

4.2.2 Experimental setup

The setup of the reactor was similar to the chapter 3 [183]. The unique feature was the addition of two-dielectric plates for the better plasma discharge. The electrohydraulic

plasma discharge reactor body is made of polycarbonate material. A high voltage transformer (catalog#: 110-LLHI10122/D115, Plasma Technics, Inc., Racine, WI, output: 12 KV) was used to supply power, which was connected to an alternating current source. To produce plasma discharge, two stainless-steel bars were joined to high voltage and ground electrodes to make a full electrical circuit, separated by two dielectric plates as shown in the fig. 4.1. Between the electrodes, the dielectric plates were designed with a small hole in the center (0.8 mm). In comparison to the most frequently studied designs, pin-pin and pin-plate electrohydraulic discharge reactors, this design has a unique ability to establish a complete discharge through the conducting channel of the orifice rather than between the electrodes. The orifice in the middle of the dielectric plate allowed electrons to concentrate near the opening, and discharge current could be kept in the plasma phase as mobile electrons, allowing for better mass transfer and breakdown of substrate molecules in contact with the plasma discharge. To vary the voltage and power applied, a variac variable voltage regulator (model#: TDGC2-2KM, ISE, Inc., Cleveland, OH) was used. The applied voltage between the top electrode and the ground electrode was measured using a high voltage probe (Tektronix P6015A) connected to an oscilloscope (Tektronix TBS1052B, Beaverton, OR). The amount of power applied to the entire system was determined using a power consumption Watt meter. A peristaltic pump (Masterflex L/S 7523-60, Vernon Hills, IL) was also included in the system, allowing the as prepared p-NP solutions to be continuously passed through the reactor for treatment. This continuous operational design could significantly improve the reactor quantity and capacity and thus reduce operating costs and reactor size at the commercial level [149, 157].

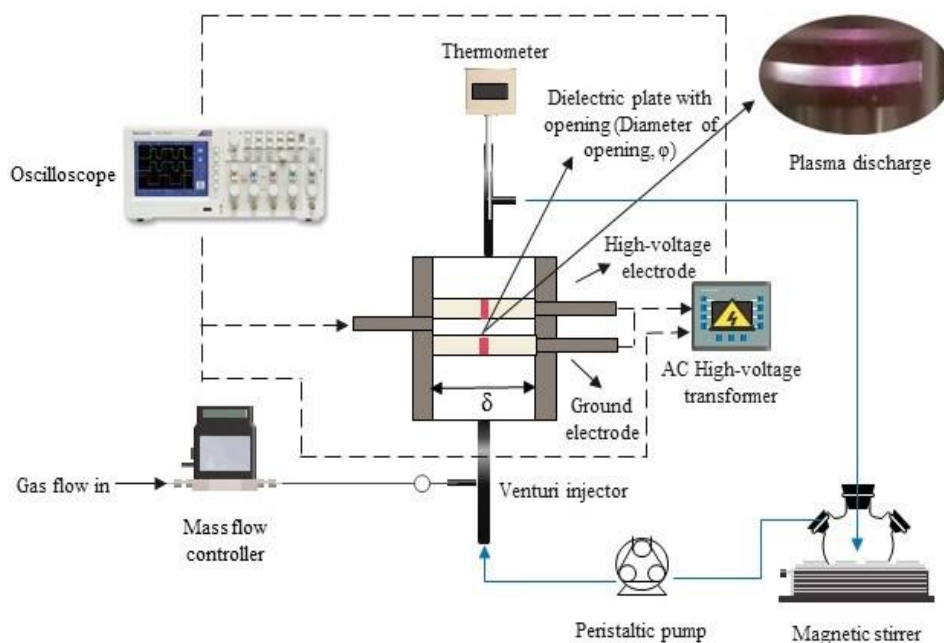


Figure 4.1. Schematic of the novel electrohydraulic discharge reactor system; $\delta = 3.2$ mm, $\varphi = 0.8$ mm

4.2.3 Design of Experiments (DOE)

Minitab 20.2.0 version (Minitab Inc., State college, PA) and Design Expert 11 (StatEase, Inc., St. Paul, MN 55413, USA) were both used in this study for factors screening and optimization studies. In the DOE, the initial step is to start screening the main effects of the process by performing a fractional factorial design (FFD). FFD follows a reduced set of experiments 2^{n-k} , for screening the main factors, where n is the number of factors to study at low and high levels (-1, +1) and k is the number of steps to minimize the experimental design [184]. Typically, the outcome of the screening experiment is the identification of a subset of a few critical factors. These factors can be further employed in a new experimental design as per response surface methodology (RSM) called central composite design (CCD) to determine the optimal factor values [185, 186].

4.2.4 Experimental procedure

Four process factors were selected for FFD such as pH, argon flowrate, applied power and persulfate, and their effects on p-NP degradation efficiency and energy yield were set as

dependent variables. Once the main independent variables were determined, a CCD was used to verify the optimal conditions of EHPD, setting the main significant factors as independent variables, which represent a quadratic response surface for each dependent variable.

A total volume of 100 mL of initial concentration 50 mg/L p-NP solution was used for each experimental run. Sodium sulfate was used to adjust the initial conductivity (65 $\mu\text{S}/\text{cm}$) of the solution. The solution was introduced to a three-neck flask connected to a condenser tube and pumped through the EHPD reactor through a peristaltic pump for treatment. The treated solution was then directed back to the flask to accomplish a continuous mixing and circulating operation. Argon gas was used for the initiation of plasma discharge. Once the solution filled the discharge region, the power was turned on. The treatment time was 10 min for each run. After each experimental run, the reactor system was flushed twice with distilled water to clean the system. The initial and final pH and conductivity of p-NP was measured using conductivity and pH probes with a Hach HQ 440D multi-meter.

Degradation of p-NP was monitored at 1 min intervals up to 10 min of EHPD treatment using a UV-vis spectrophotometer (Biotek Synergy HT) at 317 nm. Each experiment was repeated twice and were carried out at atmospheric pressure and ambient temperature. The degradation efficiency of p-NP is measured as follows:

$$n(\%) = (C_0 - C) / C_0 * 100 \quad (1)$$

C_0 = initial concentration, C = final concentration.

Total organic carbon was measured by TOC kit and analyzed by Hach DR3900 laboratory spectrophotometer for water analysis.

$$TOC(\%) = (TOC_0 - TOC_t) / TOC_0 * 100 \quad (2)$$

where TOC_0 = TOC of initial solution and TOC_t = TOC of the solution at time t .

The amount of hydrogen peroxide (H_2O_2) concentration in plasma treated solution was determined by using reaction of titanium sulfate reagent to form pertitanic acid. The absorbance at 407 nm in a UV-vis spectrophotometer was used to estimate the concentration of pertitanic acid, which is directly proportional to the reacting H_2O_2 concentration [160, 161].

The energy yield for p-NP degradation is calculated using Eq. 3. The yield value was expressed as the amount of pollutant converted divided by the energy input required at n % conversion of the pollutant [84]:

$$Y (g/kWh) = (C_0 * V_0 * n\% * 1/100) / Pt \quad (3)$$

where C_0 was the initial concentration of the pollutant in mg/L, V_0 was volume of treated solution in L, n % was degradation efficiency at time t, P was average power dissipated in the discharge (kW), and t was the time (in hour).

4.2.5 Radical scavenging experiments

To determine the role of active species produced during the EHPD process in p-NP degradation, ascorbic acid (3 mmol/L), sodium nitrate (3 mmol/L), and 10 mL diluted 2-propanol (100 mg/L) in distilled water were added to 50 mg/L p-NP to inhibit superoxide radical ($\cdot O_2^-$), aqueous electrons (e^-_{aq}), and hydroxyl radical ($\cdot OH$), respectively [183]. To compare with the scavenger-free experiment for p-NP degradation, the optimum conditions from the CCD were used for all radical scavenging tests. The efficiency of p-NP degradation was determined using a UV-Vis spectrophotometer (Biotek Synergy HT) at 317 nm.

4.2.6 Analytical methods

LC-MS data was collected using a Waters Acquity UPLC in conjunction with a Waters Xevo TQ MS triple quadrupole mass spectrometer. A reverse HPLC method was used with a 2.1 mm x 100 mm Hewlett-Packard Hypersil ODS column with a particle size of 5 μ m that was kept at 35°C. The solvent A mobile phase was water containing 0.1 percent formic acid, while the solvent B mobile phase contained acetonitrile containing 0.1 percent formic acid. The injection volume was 10 μ L and the flow rate was 0.1 mL/min. The initial solvent composition was 80% solvent A and 20% solvent B, which was kept isocratic for 1 minute after injection. A linear gradient was then initiated, bringing the composition to 20% A and 80% B in 6 minutes. The composition was held isocratic for the next two minutes, then returned to starting conditions for one minute before being allowed to equilibrate for three minutes. UV-vis absorption spectra were collected on an Acquity Diode Array Detector between 200 and 500 nm. Data for mass spectrometry were collected in negative ion ESI mode with a capillary voltage of 2.4 kV and a cone voltage of 20 v. The desolvation temperature was 300°C, and the flow rate of the desolvation gas (N₂) was 400 L/Hr. Total

ion MS spectra were collected at 1.5 sec/scan between 50 and 350 Da. Analytes of interest were identified from the resulting data by generating extracted ion chromatograms (TICs) of expected analytes and identifying peaks in the TICs.

A Dionex Ion Analyzer (Dionex, Sunnyvale, CA) with a GP40 gradient pump, an ED40 electrochemical detector, and an AS40 autosampler was used to detect inorganic ions in p-NP degradation. The mobile phase was 100 mM sodium hydroxide (NaOH), and the injection volume was around 20 μ L. The detector stabilizer temperature was set to 30 $^{\circ}$ C and the anion suppressor current was set to 300 mA. To compare the products created in the ion chromatography trace, the inorganic ions check standard (CertiPrep) was utilized as a reference.

4.3 Results and Discussion

4.3.1 2^{4-1} fractional factorial design

In this study, a 2^{4-1} FFD was designed to screen the significant variables on the degradation of p-NP using EHPD through a series of experiments conducted from various corners of the experimental area. A two-level half factorial design with four factors requires a total of 8 experimental runs. Four process variables such as pH, argon flowrate, applied power and persulfate were screened in 2^{4-1} factorial design with a duplicate of corner points as shown in the table 4.1, with responses being the degradation efficiency and energy yield.

The significance of each analyzed input variable influence was shown in a Pareto chart (Fig. 4.2 (a) and (b)). based on the results of the analysis of variance (ANOVA) model (table 4.2). Thus, ANOVA model showed argon flowrate, applied power, and persulfate were significant within the 95% confidence interval ($p \leq 0.05$) for both the responses. As illustrated in Fig. 4.3 (a) and (b), the predicted value vs actual values were in reasonable agreement and satisfies the prediction capability. Fig. 4.4 (a) and (b) illustrates the four main effects on degradation efficiency and energy yield. It clearly shows that for both responses, the larger the vertical line, the greater the difference when changing from level -1 to +1. Moreover, it was observed that the effect of argon flowrate and applied power were more noticeable, even though persulfate was significant. Thus, for the optimization, argon and power were elected as the important main effects for p-NP degradation using EHPD.

Table 4.1. The 2^{4-1} fractional factorial experimental design matrix with responses

	Factor A	Factor B	Factor C	Factor D	Response 1	Response 2
Run Order	Argon (L/min)	pH	Power (W)	Persulfate (mg/L)	Degradation efficiency (%)	Energy yield (g/kWh)
13	0.4	5	200	50	77.5	0.116
8	0.4	9	200	250	75.27	0.112
9	1	5	200	250	89.01	0.133
5	1	9	200	50	91.49	0.137
15	0.4	5	300	250	85.67	0.085
12	0.4	9	300	50	85.27	0.085
1	1	5	300	50	93.96	0.093
3	1	9	300	250	92.49	0.092
2	0.4	5	200	50	75.85	0.114
7	0.4	9	200	250	74.91	0.112
11	1	5	200	250	88.5	0.133
14	1	9	200	50	92.21	0.138
10	0.4	5	300	250	84.07	0.084
6	0.4	9	300	50	84.45	0.084
4	1	5	300	50	94.3	0.094
16	1	9	300	250	93.2	0.093

Table 4.2. Analysis of variance for the factorial model

Response 1: Degradation efficiency

Source	Sum of Squares	df	Mean Square	F-value	p-value	
Model	726.36	7	103.77	221.88	< 0.0001	significant
A-Argon	530.96	1	530.96	1135.33	< 0.0001	
B-pH	0.0116	1	0.0116	0.0247	0.8790	
C-Power	148.05	1	148.05	316.57	< 0.0001	
D-Persulfate	8.87	1	8.87	18.96	0.0024	
AB	2.90	1	2.90	6.20	0.0375	
AC	33.61	1	33.61	71.87	< 0.0001	
AD	1.97	1	1.97	4.21	0.0744	
Pure Error	3.74	8	0.4677			
Cor Total	730.10	15				

Response 2: Energy yield

Source	Sum of Squares	df	Mean Square	F-value	p-value	
Model	0.0062	7	0.0009	1573.95	< 0.0001	significant
A-Argon	0.0009	1	0.0009	1626.78	< 0.0001	
B-pH	6.250E-08	1	6.250E-08	0.1111	0.7475	
C-Power	0.0051	1	0.0051	9025.00	< 0.0001	
D-Persulfate	0.0000	1	0.0000	32.11	0.0005	
AB	0.0000	1	0.0000	18.78	0.0025	
AC	0.0002	1	0.0002	312.11	< 0.0001	
AD	1.562E-06	1	1.562E-06	2.78	0.1341	
Pure Error	4.500E-06	8	5.625E-07			
Cor Total	0.0062	15				

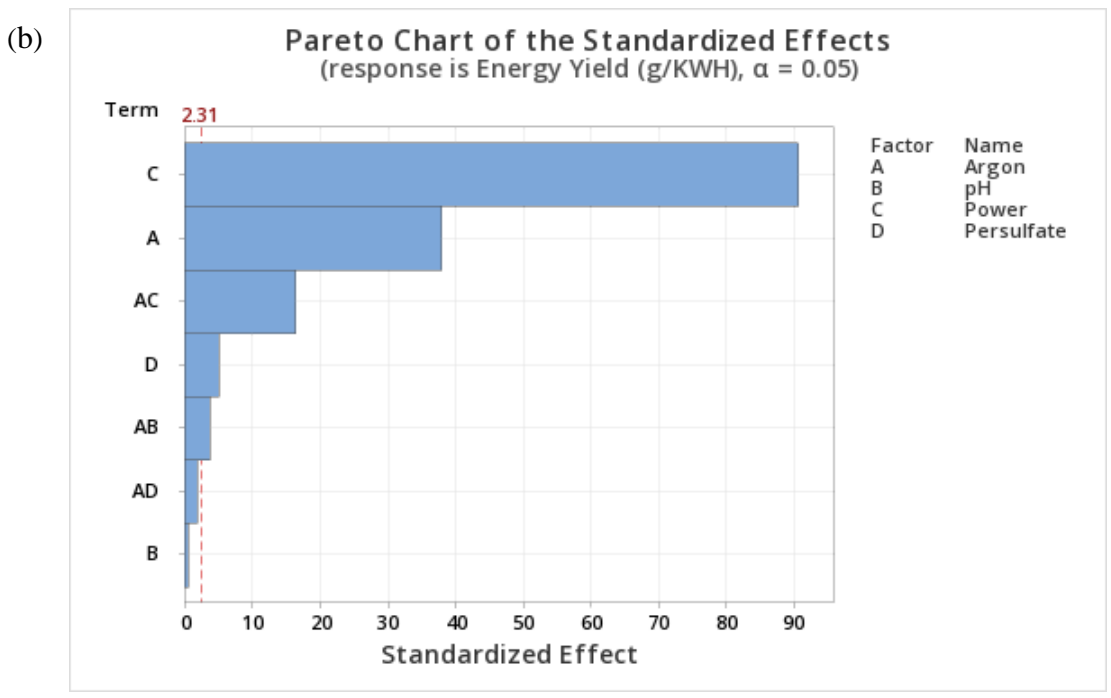
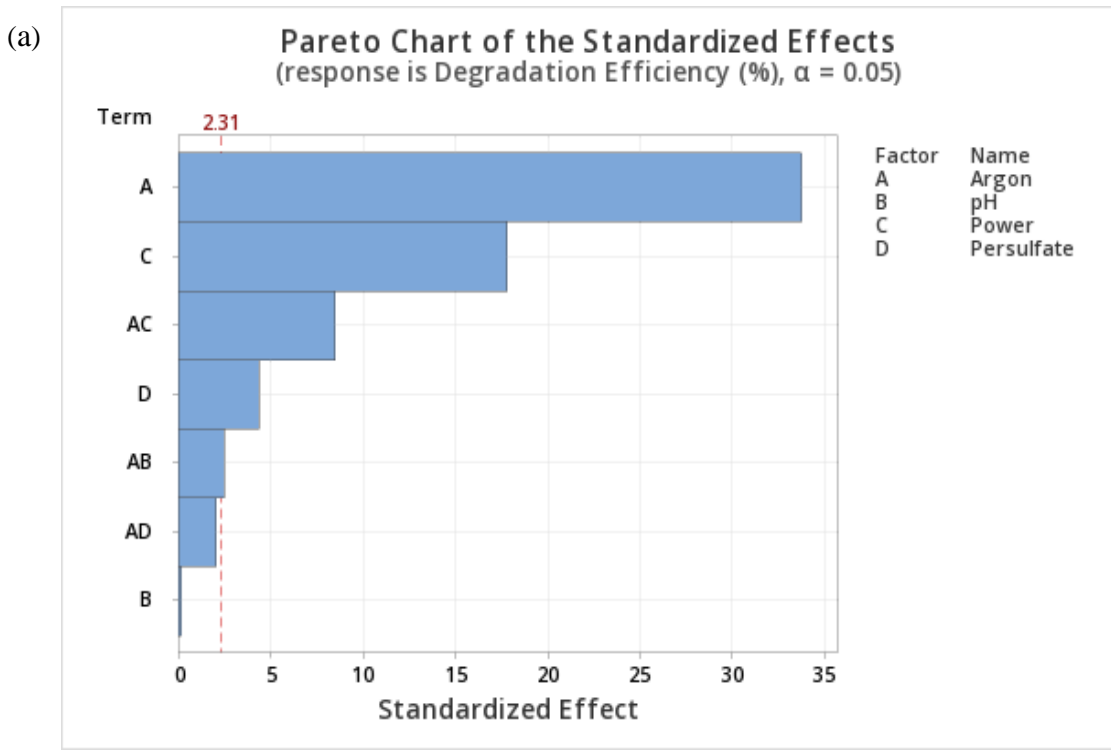

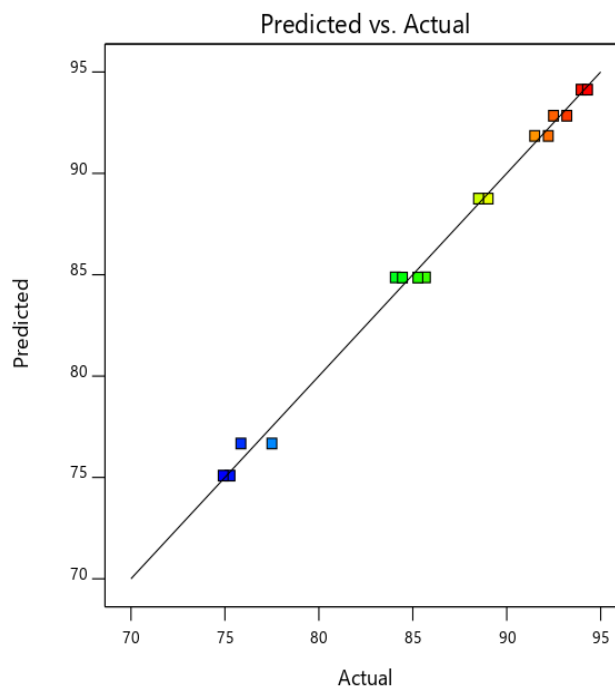


Figure 4.2. Pareto charts of the standardized effects based on (a) response degradation efficiency and (b) based on energy yield (Minitab)

(a) **Design-Expert® Software**
Degradation efficiency
 Color points by value of
 Degradation efficiency :
 74.91  94.3



(b) **Design-Expert® Software**
Energy yield
 Color points by value of
 Energy yield:
 0.084  0.138

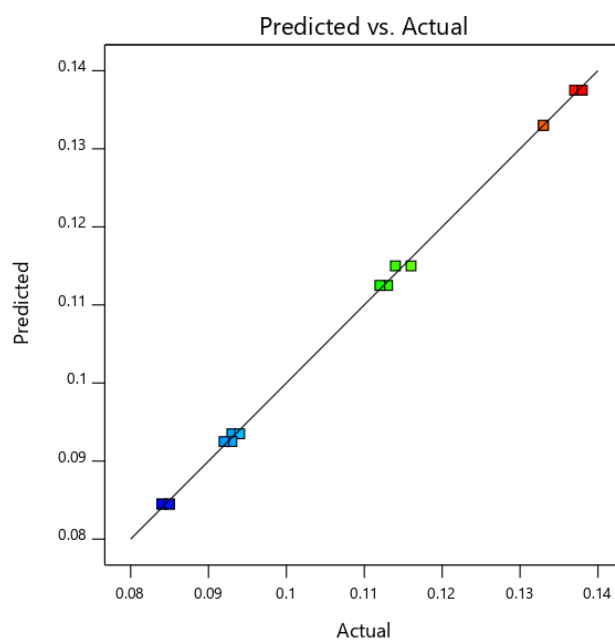


Figure 4.3. FFE predicted values vs actual values of (a) degradation efficiency and (b) energy yield

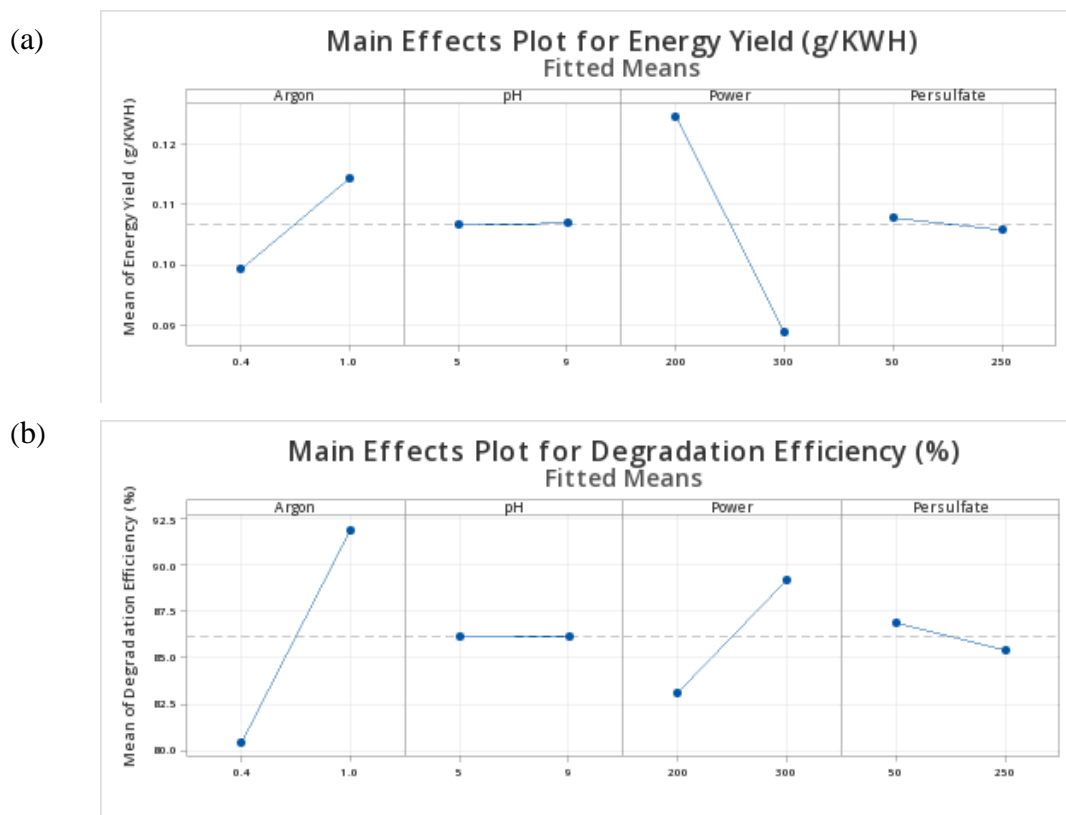


Figure 4.4. Four main effects plots for (a) degradation efficiency and (b) energy yield

4.3.2 Central composite design

According to the FFD, argon flowrate and applied power were found to be the most significant factors. Therefore, argon flowrate and applied power were chosen as control variables to be optimized using CCD for EHPD with the aid of Design Expert 11 and Minitab version 20.2.0. In CCD, a second order quadratic model, Eq. (4) was developed by varying each variable at five levels ($-\alpha$, -1 , 0 , $+1$ and $+\alpha$), to fit the responses to the independent variables. For the two independent variables, a total of thirteen experiments were run at five levels. Table 4.3 shows the many combinations of controlling factors that were examined, as well as the results achieved. Different levels of argon flow rate and power were performed according to the experimental runs as suggested by CCD model.

$$Y = \beta_0 + \beta_1x_1 + \beta_2x_2 + \beta_{12}x_1x_2 + \beta_{11}x_1^2 + \beta_{22}x_2^2 \quad (4)$$

Where: Y: the predicted response.

x_1 and x_2 : independent variables.

β_0 : the offset term

β_1 and β_2 : linear coefficients

β_{11} and β_{22} : the squared coefficients

β_{12} : the interaction coefficient

Table 4.3. Central composite design matrix of the two independent variables in real units with experimental responses for degradation efficiency (%) and energy yield (g/kWh)

		Factor 1	Factor 2	Response 1	Response 2
Std	Run	A: Argon	B: Power	Degradation efficiency	Energy yield
		L/min	W	%	g/kWh
1	11	0.8	150	83.06	0.166
2	2	2.4	150	92.63	0.185
3	13	0.8	300	93.1	0.093
4	7	2.4	300	95.37	0.096
5	8	0.468629	225	84.5	0.113
6	12	2.73137	225	95.51	0.127
7	3	1.6	118.934	83.5	0.212
8	10	1.6	331.066	96.61	0.088
9	1	1.6	225	91.96	0.1224
10	9	1.6	225	91.76	0.1223
11	5	1.6	225	91.56	0.122
12	6	1.6	225	90.23	0.12
13	4	1.6	225	92.8	0.123

4.3.3 Degradation efficiency and Energy yield model

Based on the responses - degradation efficiency and energy yield, obtained for the designated set of experiments in Table 4.3, response surface model was analyzed. The goodness of fit according to ANOVA analysis was used to validate the model, and the results was shown in Table 4.4. As shown in Table 4.4, the degradation efficiency model had an overall p value of 0.0002 and energy yield had an overall p value of less than 0.0001, suggesting both quadratic models were lower than 0.05 and were statistically significant. The F values of both models were 28.75 and 792.25 for degradation efficiency and energy yield, which implies the models were significant. Also, the terms argon, power and argon*power were found to be significant model terms in degradation efficiency model. For energy yield model, terms argon, power, argon*power and power² were significant.

Moreover, the lack of fit values of degradation and energy yield was 0.1541 and 0.0606, indicating that the lack of fit was insignificant. The insignificant lack of fit suggests a high level of predictability. With the result of ANOVA, the following empirical second order polynomial equations 5 and 6 were derived to estimate the degradation efficiency and energy yield. As shown in Fig. 4.5 (a) and (b), the observed degradation efficiency and energy yield values range from 83.06–96.61% and 0.08–0.212g/kWh, respectively, and are in good agreement with the expected values.

$$\begin{aligned} \text{Degradation efficiency (\%)} = & 54.85 + 14.01 \text{ Argon} + 0.1449 \text{ Power} \\ & - 0.900 \text{ Argon} * \text{Argon} - 0.000098 \text{ Power} * \text{Power} \\ & - 0.0304 \text{ Argon} * \text{Power} \end{aligned} \quad (5)$$

$$\begin{aligned} \text{Energy yield(g/kWh)} = & 0.33639 + 0.02638 \text{ Argon} - 0.001578 \text{ Power} \\ & - 0.00152 \text{ Argon} * \text{Argon} + 0.000002 \text{ Power} * \text{Power} \\ & - 0.000067 \text{ Argon} * \text{Power} \end{aligned} \quad (6)$$

Table 4.4. ANOVA for quadratic model of degradation efficiency and energy yield

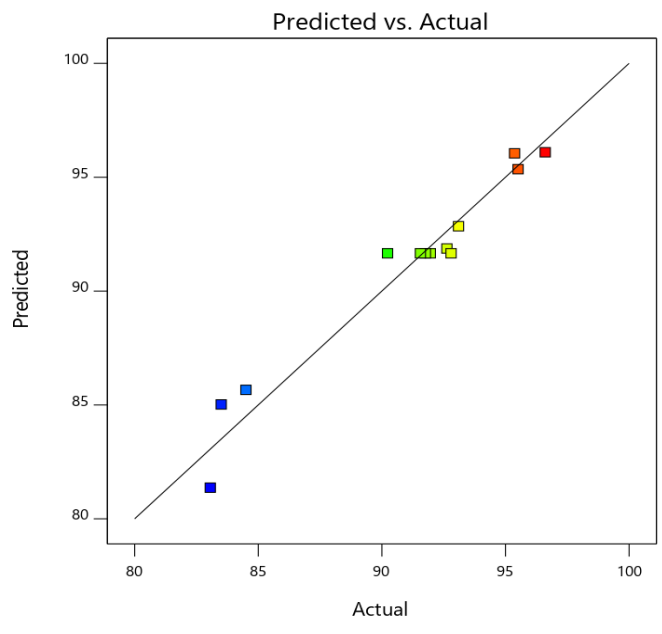
Response 1: Degradation efficiency

Source	Sum of Squares	df	Mean Square	F-value	p-value	
Model	233.77	5	46.75	28.75	0.0002	significant
A-Argon	93.92	1	93.92	57.76	0.0001	
B-Power	122.62	1	122.62	75.41	< 0.0001	
AB	13.32	1	13.32	8.19	0.0243	
A ²	2.31	1	2.31	1.42	0.2723	
B ²	2.11	1	2.11	1.30	0.2919	
Residual	11.38	7	1.63			
Lack of Fit	7.93	3	2.64	3.06	0.1541	not significant
Pure Error	3.45	4	0.8636			
Cor Total	245.15	12				

Response 2: Energy Yield

Source	Sum of Squares	df	Mean Square	F-value	p-value	
Model	0.0159	5	0.0032	792.25	< 0.0001	significant
A-Argon	0.0002	1	0.0002	54.29	0.0002	
B-Power	0.0142	1	0.0142	3536.83	< 0.0001	
AB	0.0001	1	0.0001	15.91	0.0053	
A ²	6.545E-06	1	6.545E-06	1.63	0.2428	
B ²	0.0014	1	0.0014	340.42	< 0.0001	
Residual	0.0000	7	4.022E-06			
Lack of Fit	0.0000	3	7.642E-06	5.84	0.0606	not significant
Pure Error	5.232E-06	4	1.308E-06			
Cor Total	0.0160	12				

(a) Design-Expert® Software
Degradation efficiency
Color points by value of Degradation efficiency:
83.06 96.61



(b) Design-Expert® Software
Energy Yield
Color points by value of Energy Yield:
0.088 0.212

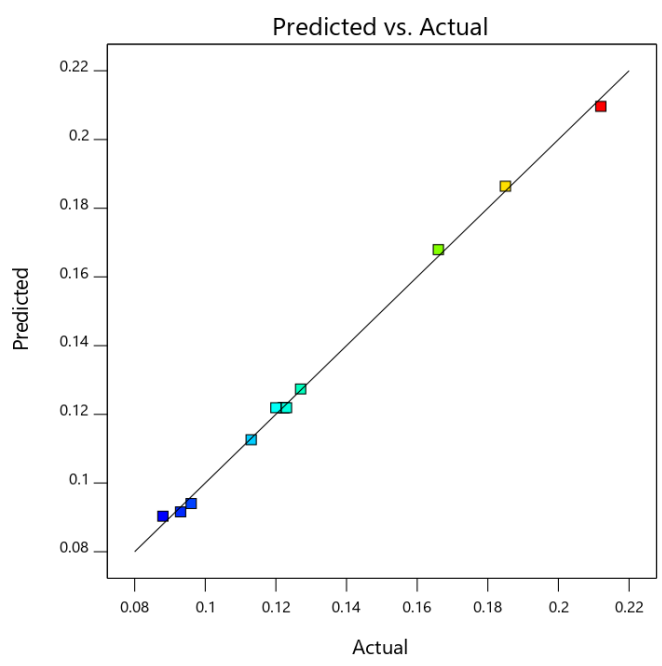


Figure 4.5. CCD predicted values vs actual values of (a) degradation efficiency and (b) energy yield

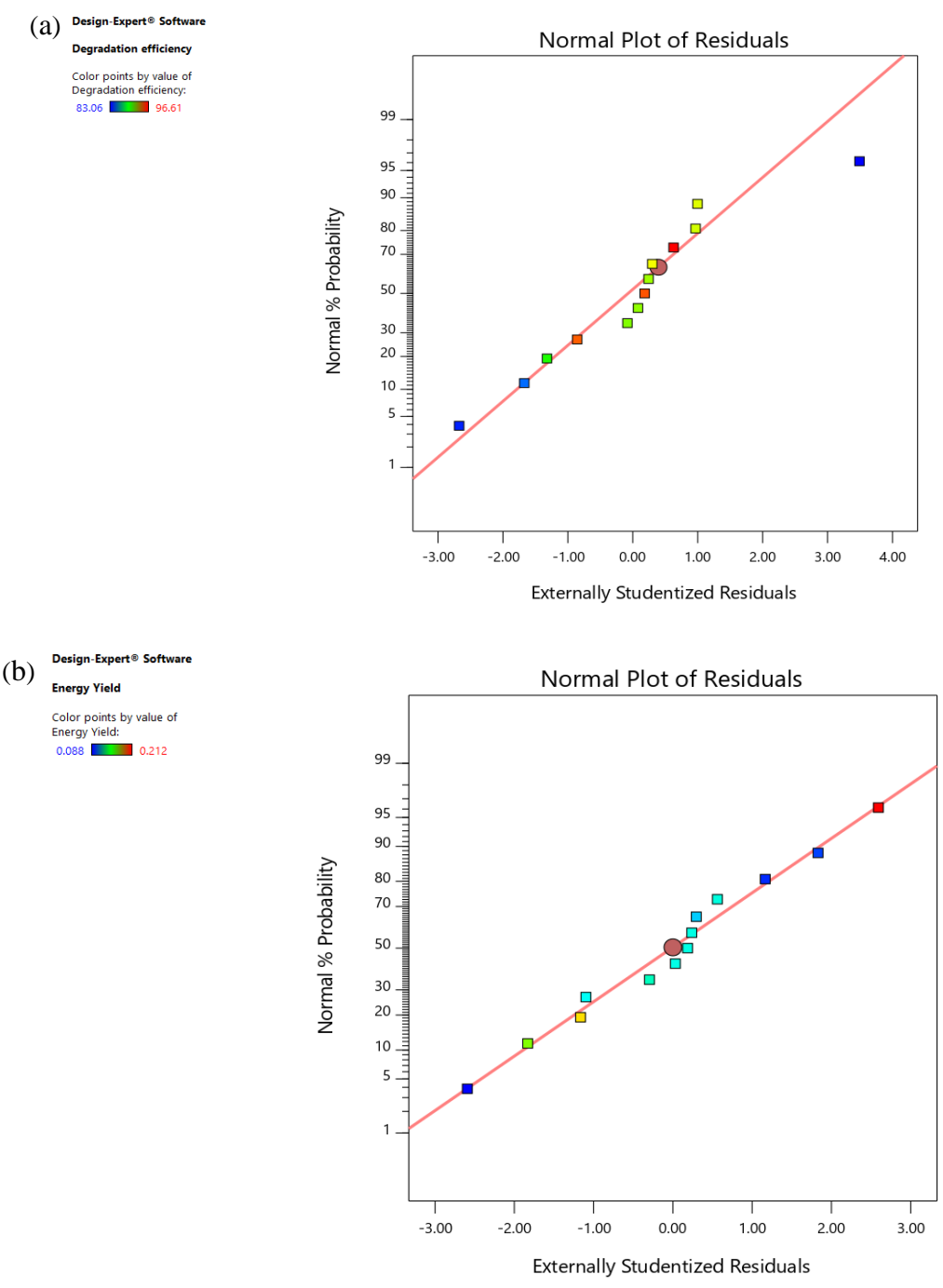


Figure 4.6. Normality plots for the regression model (a) degradation efficiency and (b) energy yield

Besides that, goodness of fit can be determined using R^2 value. In both responses, the R^2 (0.9536 and 0.9982) was in reasonable agreement with the adjusted R^2 (0.9204 and 0.9970) values. Also, Adeq precision was used to verify the model's validity by measuring the signal to noise (S/N) ratio. It is suggested that the ratio should be greater than 4. In this study, the ratio was 17.0 and 87.5 for degradation efficiency and energy yield responses, indicating an adequate signal. In addition to all these parameters, the normality plots and were used to provide further evidence and validation for the regression model. As shown in the Fig. 4.6 (a) and (b) the normality plot of externally studentized residuals denoting the major number of color points representing degradation efficiency and energy yield located in a narrow range on a normal probability line, while the minor-significant points departed from the normal line. Both models confirm the normal distribution of the plots. Therefore, all these results in this study concluded that the regression model could provide reliable prediction of degradation efficiency and energy yield.

4.3.4 Graphical interpretation and optimization of operating parameters

Figure 4.7 (a) and (b) and 4.8 (a) and (b) represents the contour and surface plots to view the effects of argon and power and their interaction between them in degradation efficiency and energy yield, developed to define the optimum value of each variable towards the maximum degradation efficiency and energy yield of EHPD process. As shown in Fig. 4.7 and 4.8(a), it implies that degradation efficiency was enhanced with the increase of either argon flowrate or applied power. The impact of argon flow rate is more prominent than the power. It also noticed that at high power (331.066 W) and mid-range argon flowrate (1.6 L/min), the degradation efficiency was maximum (96.61%) within 10 min of treatment time. However, argon flow rate plays an important parameter that can influence species concentrations when the plasma was initiated. Larger bubbles were evidently produced by a high argon flow rate. The plasma composition, as well as the concentrations of numerous species, are all directly related to argon flow rate [176, 187]. As shown in the Fig. 4.7 and 4.8 (b), the energy yield implies having a low power and high argon flow rate to have maximum energy yield. As the most energy efficient setting, low power should be preferred. When lower power is used, less energy may lose to heat dissipation, allowing the energy yield to be increased.

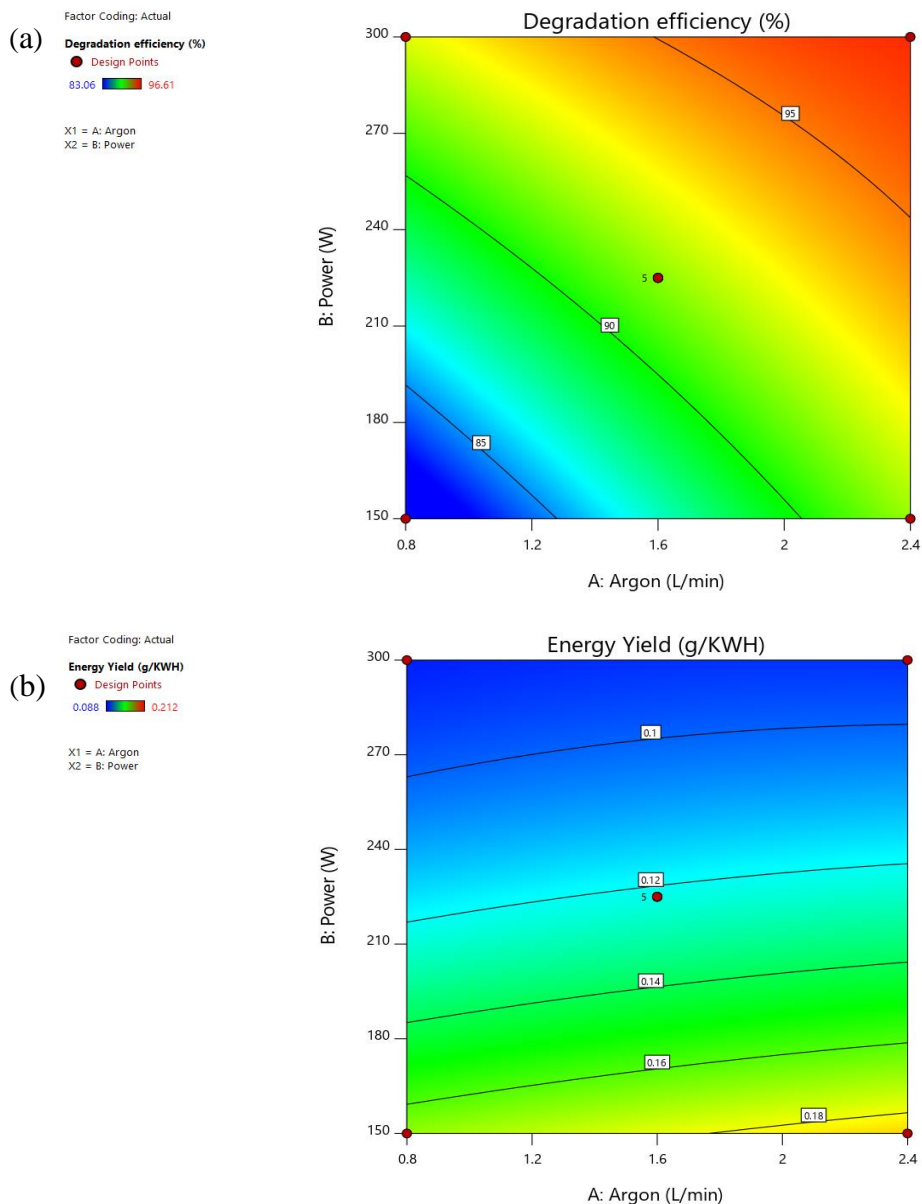


Figure 4.7. Contour plots of (a) degradation efficiency and (b) energy yield

Optimization of influencing factors is required to discover the optimum values of variables that lead to the best p-NP degradation efficiency and energy yield. The maximum value was chosen for the desired degradation and energy yield target, and the process variables were placed within the experimental range. A Minitab software was used for response surface optimization. The maximum percentage degradation was 92.73% and energy yield of 0.212 g/kWh was predicted under optimum conditions of argon flow rate of 2.73 L/min and applied power of 128.6 W (fig 4.9). To validate that the models were

satisfactory in predicting the maximum degradation and energy yield, an additional experiment was carried out in optimized conditions. The maximum degradation efficiency and energy yield in this study were 94.23 % and 0.22 g/kWh, respectively, meaning that RSM was a reliable technique for obtaining maximum degradation and energy yield in this investigation, and model accuracy was satisfactory.

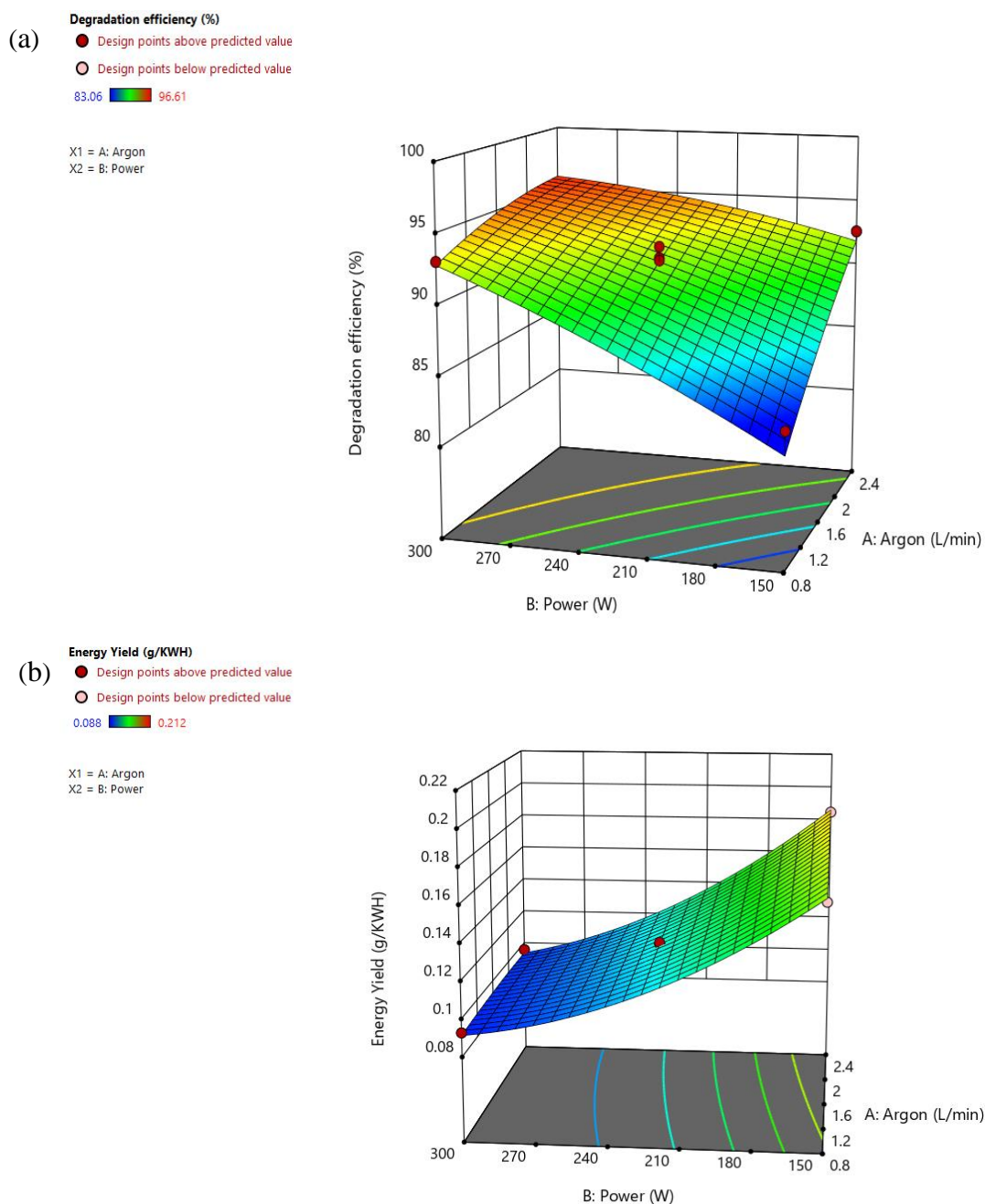


Figure 4.8. Surface plots of (a) degradation efficiency and (b) energy yield

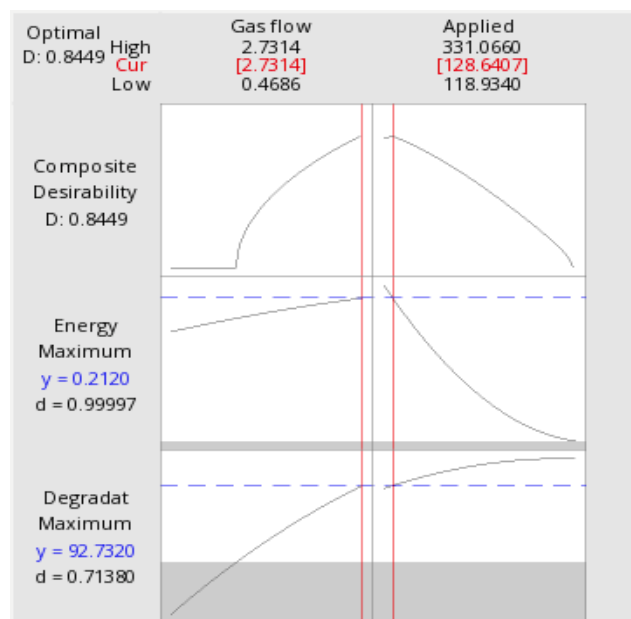
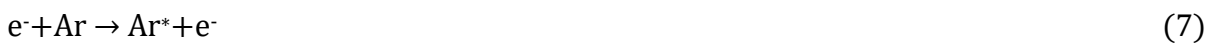


Figure 4.9. Optimization of EHPD process

4.3.5 Emission spectra of EHPD process

The emission spectra of the plasma discharge were recorded to better understand the nature of active species that contribute to degradation. Fig. 4.10 presented the optical emission spectra of the argon activated EHPD for p-NP (50 mg/L) degradation measured under optimum conditions. During plasma treatment, argon atomic (Ar I) system lines in between 690 to 965 nm were discovered in the OES spectra, corresponding to radiative de-excitations from 4p and 4p' to 4s levels [176, 179]. The emission line at 309.6 nm was attributed to be from $\cdot\text{OH}$ radical species corresponding to the transition $A^2\Sigma^+ (v''=0) - X^2\Pi (v''=0)$ [188]. Moreover, atomic oxygen species (OI at 777.03 and 844.13 nm) and H line of the Balmer series such as H_α (at 655.92 nm) and H_β (at 486.16) were discovered [189]. The formation of $\cdot\text{OH}$ radicals and hydrogen species during the plasma treatment may be attributed to the high-energy electrons colliding with the Ar atoms generates excited Ar atom, which further reacts with water to form $\cdot\text{OH}$ and H radicals as shown in Eq. 7-8. Also $\cdot\text{OH}$ and H radical may be produced by dissociation, ionization and excitation of water molecules (eq. 9-14). While the formation of atomic oxygen may be due to the dissociation of oxygen molecules as shown in eq. 15 [179, 190-192].



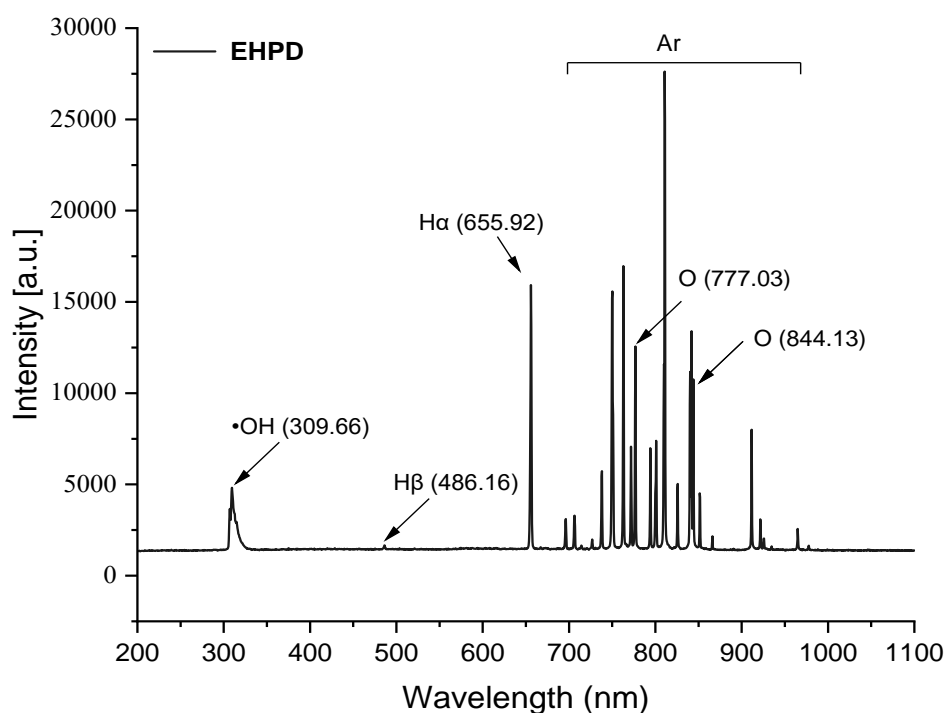


Figure 4.10. Optical emission spectra of argon activated EHPD process

4.3.6 Effects of initial concentration

Fig. 4.11. showed the effect of initial p-NP concentrations (10, 25, 50, and 100 mg/L) on p-NP degradation by EHPD performed under the optimal conditions such as 2.73 L/min argon flow rate and 128.6 W power obtained from the CCD. The 10 mg/L initial concentration showed a 100% p-NP degradation efficiency after 9 min of treatment, followed by 25 mg/L (95.35%), 50 mg/L (94.23%), and 100 mg/L (89.39%), respectively, within 10 min of treatment time. The complete degradation was achieved within 12 min of treatment

for 25 mg/L, 13 min for 50 mg/L and 15 min of treatment for 100 mg/L initial p-NP concentration. It was clear that initial p-NP concentration influenced the degradation efficiency as the lower concentrations have slightly higher degradation efficiency than at higher concentrations. Similar effect was reported by Zhao et al. [179], stating that the reactive chemical species interacted with p-NP intermediates before diffusing into the system to destroy the other p-NP molecules when the initial concentration was high. Therefore, under optimal conditions of argon flowrate and power, EHPD process showed effective degradation of p-NP.

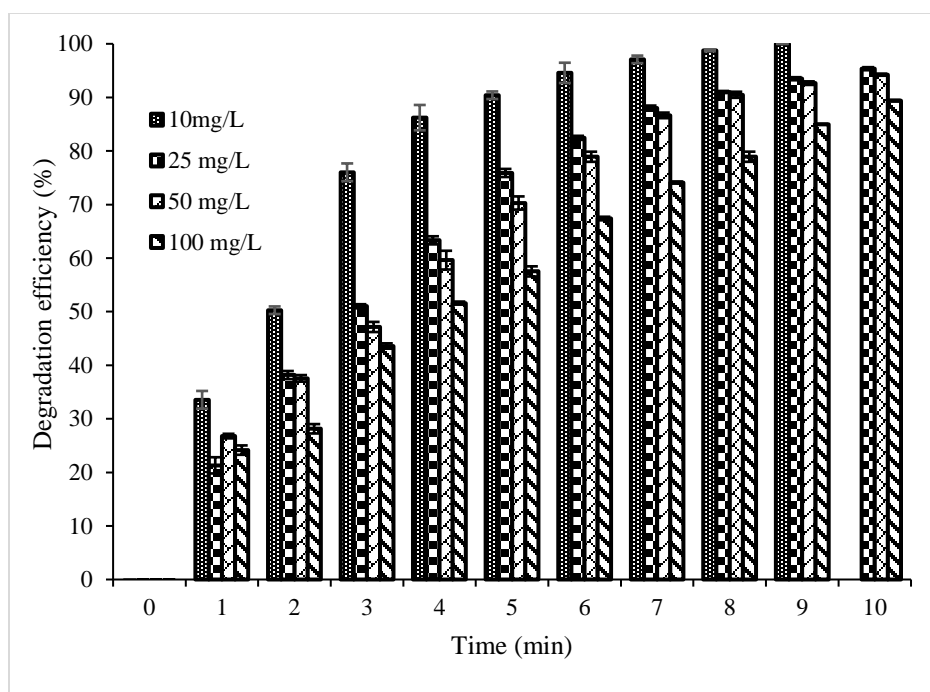


Figure 4.11. Degradation efficiency of different initial concentrations of p-NP by EHPD

Moreover, as shown in Fig. 4.12, the results of p-NP degradation at different initial concentrations by EHPD followed first order kinetics, correlation coefficients were obtained using linear regression by plotting $-\ln(C_t/C_0) = kt$ at initial p-NP concentrations. The correlation coefficients for all initial concentrations were above 0.98 and the kinetic constant K (min^{-1}) decreased from 0.5404 min^{-1} to 0.2121 min^{-1} degradation. The results of the first order kinetic constant for degradation of p-NP at different initial concentration were presented in Table 4.5.

Table 4.5. First order kinetic constant for degradation of p-NP at different initial concentrations

Operational parameters	Rate constant, K (min ⁻¹)	R ² value	Half-life, t _{1/2} (min)
<i>Initial Concentration (mg/L)</i>			
10	0.5404	0.9895	1.28
25	0.3151	0.9952	2.20
50	0.2956	0.9872	2.34
100	0.2121	0.9801	3.27

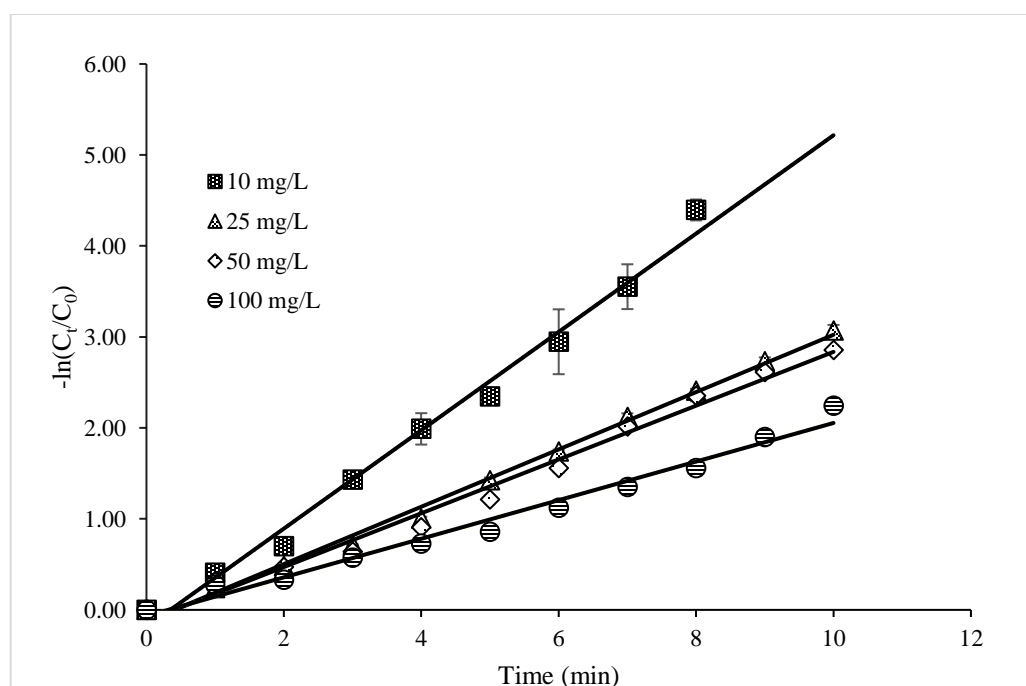


Figure 4.12. First order kinetics of different initial concentrations of p-NP degradation

4.3.7 Radical scavenging experiment

Radical scavengers were added to the p-NP solution at an initial concentration of 50 mg/L under optimal conditions of argon flow rate of 2.73 L/min and power of 128.6 W for detection of aqueous electrons, superoxide, and hydroxyl radicals. Furthermore, the results were compared to those obtained in the absence of scavengers to determine the main active species involved. To further establish the influence of radical scavengers on p-NP degradation efficiency, degradation kinetics were investigated as shown in Fig. 4.13. During the entire treatment, 2-propanol had a significant effect on p-NP degradation, the degradation

rate constant was 0.0848, showing that the production of $\cdot\text{OH}$ radicals in the argon initiated EHPD process, as the main active species for p-NP degradation. The degradation rate constant was reduced to 0.1129 with the addition of ascorbic acid, clearly suggesting a drop in degradation percentage as compared to scavenger-free trial. This data revealed that the superoxide radicals played a second most active species in degradation. When NaNO_3 was added, the degradation rate constant was 0.2116, showing a minor influence on the p-NP degradation, demonstrating that hydrated electrons had a minimal part in the argon initiated EHPD process for p-NP degradation.

The H_2O_2 concentration was also determined under optimal conditions. As shown in Fig. 4.14, the H_2O_2 concentration gradually increased as the plasma treatment time increased. The concentration increases from 27.38 mg/L at 1 min to 194.83 mg/L at 10 min. High electron density, plasma energy, and long-lived excited Ar species may have helped the energy transfer between excited species and water molecules, resulting in the production of H_2O_2 in argon activated EHPD process. Furthermore, atomic oxygen O can create H_2O_2 when it interacts with water molecules. The production of H_2O_2 in aqueous solution could be explained as follows (eq 16-18) [188, 193, 194]:



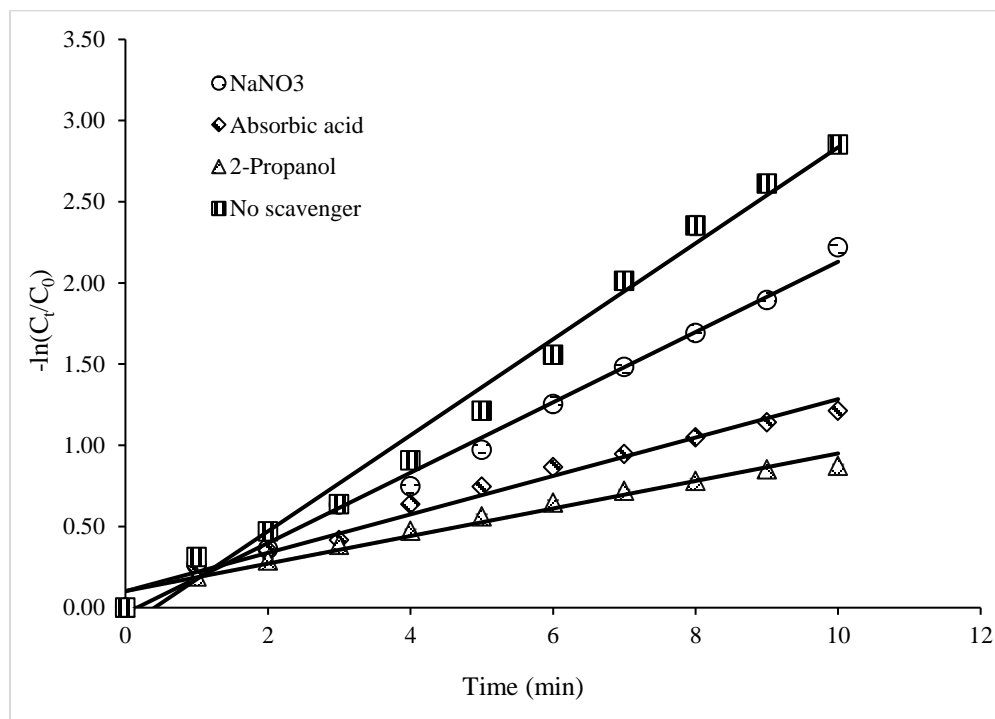


Figure 4.13. Radical scavenging experiment of EHPD process for p-NP degradation (50 mg/L)

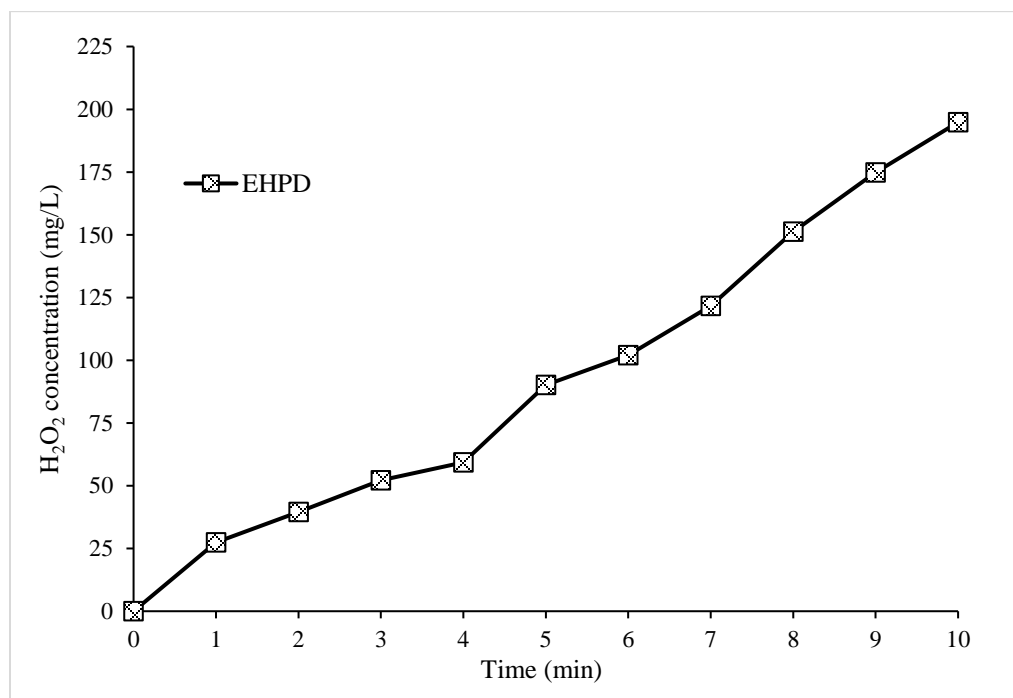


Figure 4.14. H₂O₂ concentration of EHPD process for p-NP degradation (50 mg/L)

4.3.8 TOC removal, Energy yield, pH and conductivity change

In order to evaluate the mineralization rate of p-NP, TOC was measured for different initial p-NP concentrations. TOC removal efficiency was 83.55%, 78.11%, 75.68% and 63.78% for 10 mg/L, 25 mg/L, 50 mg/L and 100 mg/L after 10 min of treatment. The result showed that in the EHPD system, more p-NP and intermediates were mineralized to smaller organic compounds or CO₂. When compared with other studies, EHPD process has a very high mineralization rate of p-NP [91, 179, 195].

The energy yield at different initial p-NP concentration under optimum conditions for 10 min treatment time were 0.05 g/kWh at 10 mg/L, 0.11 at 25 mg/L, 0.22 at 50 mg/L and 0.42 at 100 mg/L, respectively. The results showed that lower applied power and higher initial concentration was beneficial for improving the energy yield. When compared with other processes [91, 179], this study has a better energy yield and degradation efficiency. Comparison of this study with other processes was shown in table 4.6.

The initial pH was 5.45, 5.41, 5.38 and 5.36 and the initial conductivity was maintained at 65 μ S/cm (25°C) with addition of sodium sulfate corresponding to different initial p-NP concentrations of 10 mg/L, 25 mg/L, 50 mg/L, and 100 mg/L, respectively. After plasma treatment, the final pH decreased as expected and was in the range of between 3.37 - 3.65, and the final conductivity increased with increase in initial p-NP concentrations (Fig. 4.15). The interaction of reactive oxidative species from plasma with argon and water appeared to result in a decrease in pH in all cases, implying that p-NP was degraded to form acids and other ions that increased solution conductivity.

Table 4.6. Comparison of the Argon activated EHPD on p-NP degradation with other plasma processes

Methods	Initial p-NP concentration (mg/L)	Time (min)	Degradation efficiency (n%)	Energy Yield (g/kWh)	Reference
Argon activated EHPD	10	10	100	0.05	This study
	25	10	95.35	0.11	
	50	10	94.23	0.22	
	100	10	89.39	0.42	
	100	15	100	0.31	
DBD plasma	5	50	34.38	0.0994 (discharge power 4.2 W)	[91]
Plasma + persulfate	5	50	63.6	0.18 (discharge power 4.2 W)	[91]
Plasma +persulfate +Fe ²⁺	5	50	81.1	0.23 (discharge power 4.2 W)	[91]
Microwave plasma	100	12	100	0.07 (Ar flow: 8 L/min, microwave power 380W)	[179]

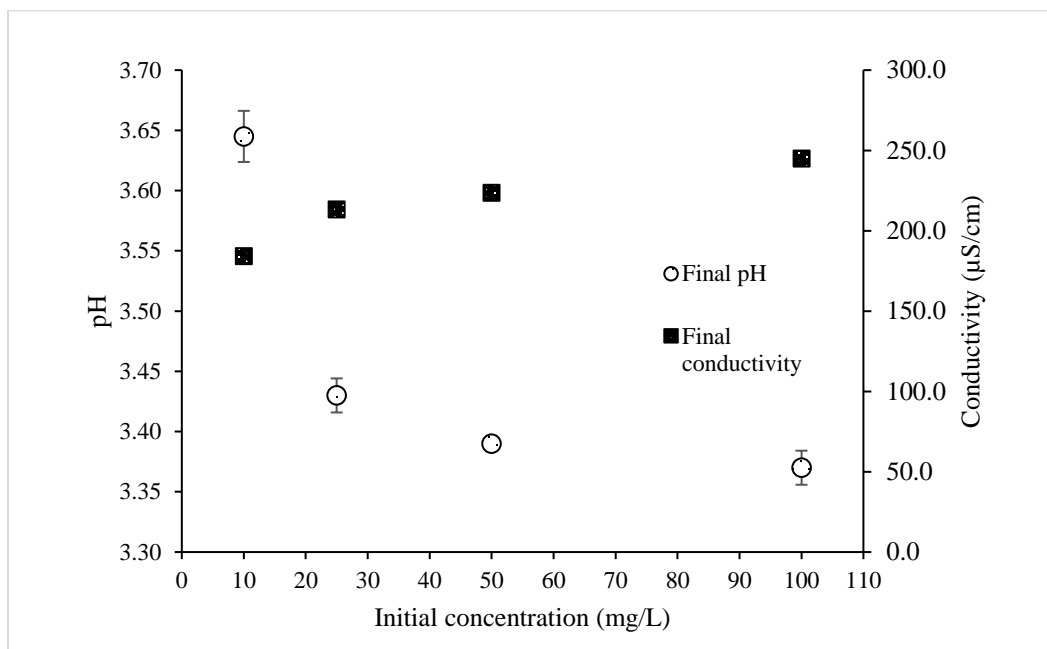


Figure 4.15. pH and conductivity for EHPD process at different initial p-NP concentration

4.3.9 UPLC-MS/MS and Ion chromatography analysis

To identify the p-NP degradation intermediates, 50 mg/L p-NP initial concentration was treated under optimal conditions by EHPD, and then intermediate products were analyzed using UPLC-MS/MS. The total chromatogram was shown in the Fig. 4.16. The intermediate products were hydroxylated, based of -ortho and-para position of the OH⁻, which has high density and the [•]OH radicals could readily attack it[196]. Based on the findings, p-NP was oxidized to p-nitrocatechol (m/z= 154) by electrophilic reaction, which further transforms by [•]OH radicals into p-nitropyrogallol (m/z=170). Further aromatic ring opening products were oxidized into aliphatic acids like formic acid or acetic acid or oxalic acid[197]. These aliphatic acids were eventually mineralized to NO₂⁻, NO₃⁻, H₂O and CO₂. The degradation pathway was shown in the Fig. 4.17. Besides [•]OH radicals, active species like [•]O and [•]H and physical effects such as heat, and UV might also participate in the process. A mass defect was found at m/z=217, which might be an inorganic material derived from sodium sulfate. The ms/ms product has a mass that corresponds close to HSO₄.

Many studies reported a similar mechanism for the degradation of p-NP through oxidation by [•]OH radicals through electrophilic attack [178, 179, 195, 197, 198]. Wang et al.[197], reported that [•]OH radicals may attack the -NO₂ group in p-NP molecules due to the relatively long C—N bond, which is the longest bond in the molecule and thus has the

potential to be attacked to form phenol, which transforms into hydroquinone, benzoquinone, and catechol generated through further oxidation of phenol. Additional reactions between these intermediates and $\bullet\text{OH}$ radicals result in ring cleavage and the formation of an aliphatic compound.

The results from ion chromatography for 50 mg/L p-NP initial concentration treated under optimal conditions showed nitrate, nitrite and sulfate were presented in low concentrations, which were produced with decomposition of p-NP molecule. While sulfate concentration was relatively high 44.9 mg/L, nitrates was 14.4 mg/L and nitrite was 1.4 mg/L at 10 min treatment time. The sulfate concentration was high due to addition of sodium sulfate addition for adjusting the initial conductivity of p-NP aqueous solution.

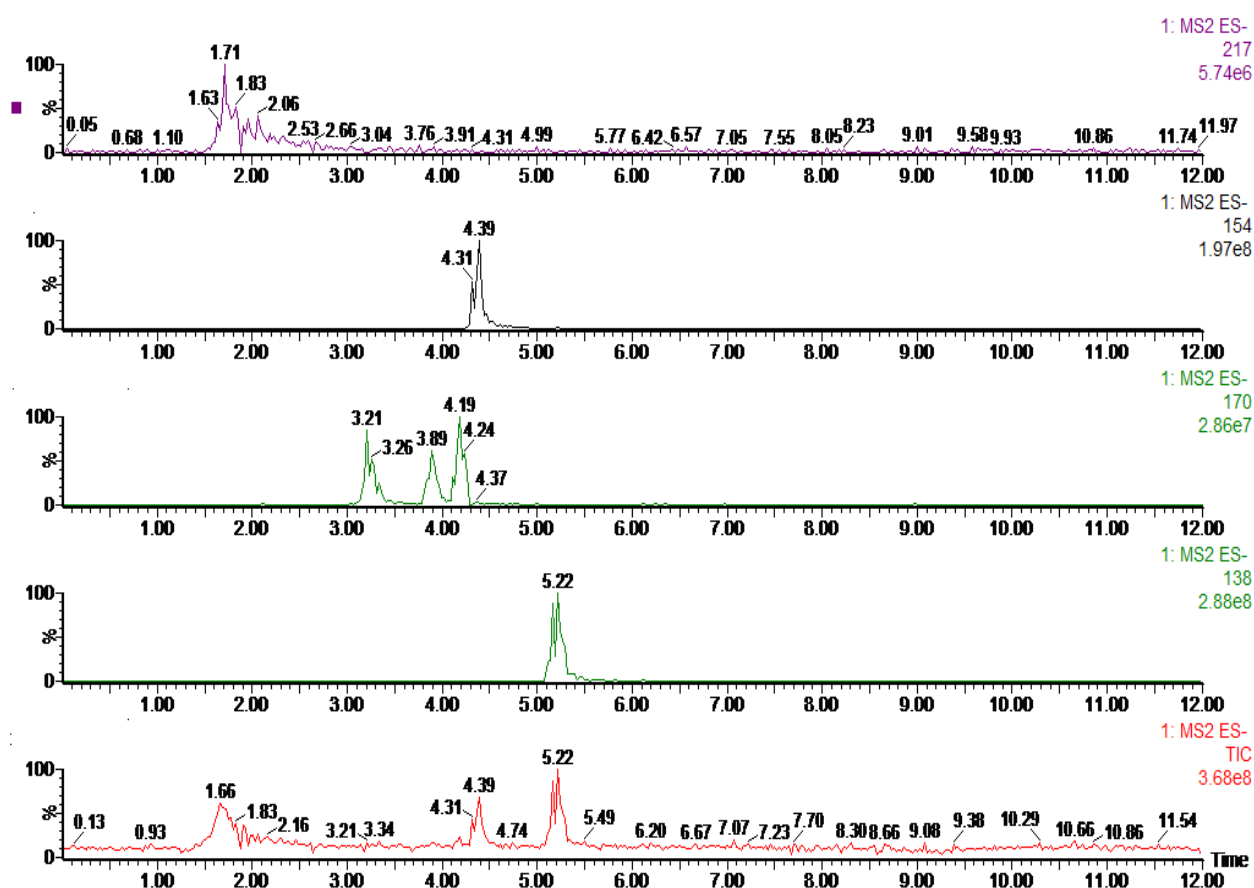


Figure 4.16. Total ion chromatogram (TIC) of p-NP degradation intermediates

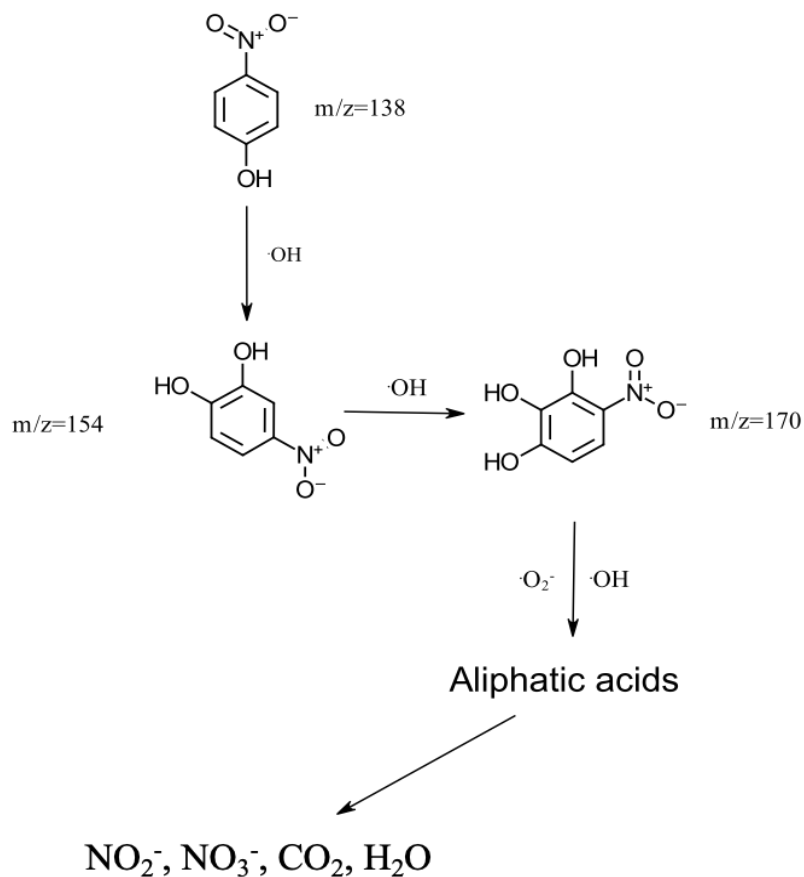


Figure 4.17. Degradation pathway of p-NP by EHPD

4.4 Conclusions

In this study, argon activated EHPD process had been efficient for p-NP degradation in aqueous solution with high performance. Fractional factorial design (FFD) was applied to screen the most significant operational factors of EHPD process. Argon and power were found to be the significant factors of EHPD process for p-NP degradation. These significant operational factors were predicted and optimized using Response surface methodology (RSM) based on CCD approach. The individual and interaction effects of argon and power were sufficiently modeled and optimized based on the responses-degradation efficiency and energy yield. The R^2 value of degradation efficiency was 0.9536 and energy yield was 0.9982, which were in reasonable agreement with the adjusted R^2 (0.9204 and 0.9970) values. Therefore, the optimal conditions for this process were found to be 2.73 L/min argon flow rate and 128.6 W applied power predicting a maximum degradation efficiency of

92.73% and energy yield of 0.212 g/kWh. Additional experiments were carried out under optimized conditions to validate the model. The maximum degradation efficiency and energy yield at 50 mg/L initial concentration were 94.23 % and 0.22g/kWh, respectively within 10 min of treatment, showing that the model accuracy was satisfactory. In addition, effect of different initial p-NP concentrations such as 10 mg/L, 25 mg/L, 50 mg/L and 100 mg/L was evaluated and found that degradation rates could be slowed down by increasing initial p-NP concentrations. Even at higher concentrations, about 90% of p-NP was degraded within 10 minutes of treatment. All experiments showed a decrease in pH and an increase in conductivity in the solution. Different initial p-NP concentrations (10 mg/L, 25 mg/L, 50 mg/L and 100 mg/L) followed first order degradation kinetics and the energy yield was in the range 0.05 g/kWh-0.42 g/kWh within 10 min of treatment. Furthermore, the H₂O₂ concentration was 194.83 mg/L and TOC mineralization efficiency was 75.68% for 50 mg/L initial concentration. Optical emission spectroscopy was used to identify the active species involved in the argon activated EHPD process and found argon atoms, [•]OH radicals, atomic oxygen species and hydrogen lines of Balmer series to be active. Radical scavenging experiment confirmed that main active species responsible for p-NP degradation was [•]OH radicals. UPLC-MS/MS and Ion chromatography was used to analyze the intermediates and inorganic ions involved in p-NP degradation by the EHPD process. Based on the intermediate products, the possible pathway for p-NP degradation was found to be electrophilic reactions by [•]OH radicals, oxidation of nitroaromatic rings and mineralized them into inorganic ions (NO_x) or smaller organic compounds, such as carbon dioxide. Therefore, under optimal conditions, the results showed effective p-NP decomposition and better energy yield compared to other studies, indicating EHPD process as a potential technology for wastewater treatment.

CHAPTER 5 BiOI/C-BNQDs CATALYST ASSISTED ELECTROHYDRAULIC PLASMA DISCHARGE PROCESS FOR P-NITROPHENOL DEGRADATION

5.1 Introduction

p-Nitrophenol (p-NP) or 4-Nitrophenol (4-NP) is a refractory aromatic organic compound used widely as chemical intermediates in the manufacturing of explosives, pesticides, dyes, pharmaceuticals, and wood preservatives [16, 17, 21, 178, 199]. Therefore, p-NP exists frequently in the industrial wastewater effluents, causing many concerns due to their potential toxicity and low degradability in the environmental media [200]. It poses a serious threat to both environment and the public, as the p-NP can lead to central nervous system damage, methemoglobin, respiratory tract, liver and kidney failure [19]. Thus, p-NP has been listed as one of the priority pollutants according to U.S. Environmental Protection Agency (U.S. EPA) and the maximum allowed concentration of p-NP in drinking water is in the range of 1-20 ppb [20, 201, 202].

It is difficult to degrade p-NP by conventional treatment technologies due to lipophilic and stable chemical structure, accumulated concentrated sludge after removal, membrane fouling, and secondary byproducts [203]. Advanced oxidation processes (AOPs) such as photocatalysis, Fenton, UV/H₂O₂, photo-Fenton, ozonation and sonolysis have gained wide attention for the degradation of p-NP as it produces hydroxyl radicals ($\cdot\text{OH}$) which is a powerful oxidant with high redox potential ($E_0=2.8\text{V}$) [16, 26, 204]. However, AOPs have some limitations such as the high cost, slower degradation, harsh pH condition, short life span and iron sludge [205]. Therefore, an improvement is needed for efficient treatment of organic pollutants.

Electrical discharge in liquid with non-thermal plasma (NTP) have a great potential and can be a promising technology out of all treatment methods for degradation of organic pollutants. At liquid-gas interface, it can produce, highly reactive chemical species such as radicals ($\cdot\text{OH}$, $\text{NO}\cdot$, $\text{H}\cdot$, $\text{O}\cdot$, $\text{NO}_2\cdot$), reactive oxygen species (H_2O_2 , O_3), reactive nitrogen species (ONOO^- and ONOOO^-) and hydrated electrons (e^-_{aq}) [32, 36, 206-208]. Moreover, it can generate ultraviolet (UV) radiation and reactive heat environment [209]. These highly reactive species help in reduction of chain length of p-NP and convert into non-toxic components. Although electrical discharge plasma demonstrated to be effective in water

treatment, there is still a need to improve the technology in terms of energy use, mineralization, and scalability.

Recently, the integration of plasma and heterogenous catalysis have attracted interest for environmental and energy applications. The combination of plasma and catalyst materials have many synergetic effects, improving energy yield and optimizing the byproducts generation [86]. The catalyst can help accelerate the reaction rates faster and improve the overall selectivity. While the plasma can generate energy to achieve highly endothermic reactions [88]. Moreover, the integration of catalyst to plasma can reduce the activation barrier of several reactions and improve the degradation rates and the energy yield of the plasma process [87]. T.C. Wang et al. [119] reported a pulsed discharge plasma-TiO₂ catalytic (PDPTC) technique for the remediation of p-NP contaminated soil. The study showed TiO₂ catalyst accelerated p-NP degradation. At pulsed discharge voltage of 20 kV, the degradation efficiency of p-NP in plasma alone treatment was 78.1% and in PDPTC was 88.8% after 10 min of discharge treatment. The total organic carbon removal rate was improved from and 55.1% after 30 min of treatment in PDPTC system. The ozone (O₃) and •OH radicals played a key role in decomposition and mineralization of p-NP in soil. Although there are no reports of plasma-catalysis degradation for p-NP in water. Therefore, designing an effective robust and energy efficient plasma-catalyst process becomes essential for water treatment.

For the catalyst selection, nano-photocatalyst is of great research interest due to its high performance, low cost and fascinating physical and chemical properties [210]. Among the different nano-photocatalysts, bismuth oxyhalides, BiOX (X=I, Cl, F or BR) shows high degradation efficiency of organic pollutants due to their active [Bi₂O₂]²⁺ layer which helps in bringing internal electrical field to each layer and promoting the separation rate of electron-hole pairs [78, 79, 211]. Among BiOX photocatalysts, bismuth oxyiodide (BiOI) shows better absorption in the visible light region due to its small band gap (1.8 -1.98 eV). However, many researchers found that the photocatalytic activity of pure BiOI can achieve high quantum yield and improved lifetime of charge carriers by combining BiOI with other nano materials [78, 111, 114, 120, 121, 123]. In particular, construction of BiOI based composites is the most promising way to enhance its photocatalytic activity for p-NP degradation.

An analog of graphene called boron nitride (BN) has emerged as a new material for organic pollutants degradation. Liu et al. [132] reported the solvothermal fabrication of novel BiOI photocatalysts modified by graphene-analogue BN. The BN/BiOI composite showed high performance visible light photocatalytic degradation efficiency for Rhodamine B, methylene blue and 4-chlorophenol in water. In addition, it showed superior improvement in efficiency with comparison over pure BiOI and TiO₂. Yang et al. [128] reported a metal-free photocatalyst constructed by boron nitride quantum dots (BNQDs) and ultrathin porous g-C₃N₄ (UPCN). BNQDs/UPCN (BU) photocatalyst showed excellent visible-light-driven molecular oxygen activation ability, such as superoxide radical ($\cdot\text{O}_2^-$) generation and hydrogen peroxide (H₂O₂) production. The average $\cdot\text{O}_2^-$ generation rate of the optimal sample was estimated to be 0.25 $\mu\text{mol/L/min}$, which was about 2.3 and 1.6 times than that of bulk g-C₃N₄ and UPCN.

In this work, BiOI/C-BNQDsX (X=1, 3 and 5 mL) composites was utilized with electrohydraulic plasma discharge (EHPD) to degrade p-NP in water. The BiOI/C-BNQDsX (X=1, 3 and 5 mL) was added directly in the p-NP aqueous solution and passed through the plasma discharge region. The different catalysts were first tested to determine best optimal catalyst and then investigate its influence on the operation parameters such as catalyst dosage and initial p-NP concentration on p-NP degradation. The degradation efficiency and energy yield were evaluated and compared with the sole EHPD process. The treated liquid was characterized for H₂O₂, pH and conductivity. Optical emission spectra (OES) were used to identify the reactive species in EHPD-catalysis system and radical scavenging experiment was used to determine main active species responsible for p-NP degradation. Furthermore, the intermediate products of p-NP degradation were identified using liquid chromatography–mass spectrometry (UPLC-MS/MS) and degradation mechanism was determined for the synergistic EHPD-catalysis system.

5.2 Materials and Methods

5.2.1 Chemicals

Bismuth nitrate pentahydrate (Bi(NO₃)₃·5H₂O) (Chemsavers Inc, VA), boric acid, urea, citric acid, potassium iodide (KI), nitric acid, potassium hydroxide (KOH) and sodium sulfate from Fisher Scientific (Eugene, OR) and p-Nitrophenol from TCI chemicals Pvt. Ltd.

5.2.2 Synthesis of C-BNQDs

Boric acid (boron), urea (nitrogen) and citric acid (carbon) were used as precursors. 0.5 g boric acid, 0.3 g urea and 0.05 g citric acid were dissolved in 15 mL distilled water. The solution was stirred for 20 minutes to form homogenous solution. Then the solution was heated for 5 min in a domestic microwave oven (700 W) without any cover. After heating, a light-yellow solid was form, which further dissolved in 30 mL distilled water and the solution was centrifuged for 30 minutes at 5000 rpm to remove excessive raw material. The clear solution was collected and filtered using 0.22 μm microporous membrane filter for two times. The resultant solution was stored at 4 $^{\circ}\text{C}$ for further analysis.

5.2.3 Synthesis of Bismuth oxyiodide (BiOI) and BiOI/C-BNQDs nanocomposites

In BiOI synthesis, 0.5 g of bismuth nitrate pentahydrate $\text{Bi}(\text{NO}_3)_3 \cdot 5\text{H}_2\text{O}$ was dissolved into 0.2 M nitric acid (HNO_3) in 20 ml distilled water under vigorous stirring for 30 min. 1 M of potassium iodide (KI) was added in to 5ml of distilled water and added dropwise into the solution. pH of 6 was adjusted by using 5M potassium hydroxide (KOH) and stirred for one hour. Then, the solution was passed into hydrothermal reactor and heated in an oven at 160 $^{\circ}\text{C}$ for 2 hours. After that, particles were collected by centrifugation technique at 5000 rpm for 10 min. The particles were washed with distilled water and ethanol many times to remove residual ions and was dried in an oven at 70 $^{\circ}\text{C}$. The dried fine powder was further subjected to different characterization techniques.

For synthesis of BiOI/C-BNQDs composites, 300 mg of BiOI was added to 20 mL methanol and ultrasonicated for one hour. Then, C-BNQDs of volume of 1 mL, 3mL and 5mL were added to the BiOI solution and sonicated overnight. The BiOI/C-BNQDsX, (X=1 mL, 3mL, and 5mL) photocatalysts was dried in a vacuum oven at 50 $^{\circ}\text{C}$ for 12 hours for methanol to be completely evaporated.

5.2.4 Experimental set up

The setup was similar to chapter 4. The body of the electrohydraulic discharge reactor was made from polycarbonate materials. The power was supplied by a high voltage transformer (catalog#: 110-LLHI10122/D115, Plasma Technics, Inc., Racine, WI, output: 12 KV), which was connected to an AC power. The plasma discharge was initiated between two

stainless steel electrodes separated by a two-dielectric plate. The two-dielectric plate between the electrodes was designed with a small opening in the middle (0.8mm).

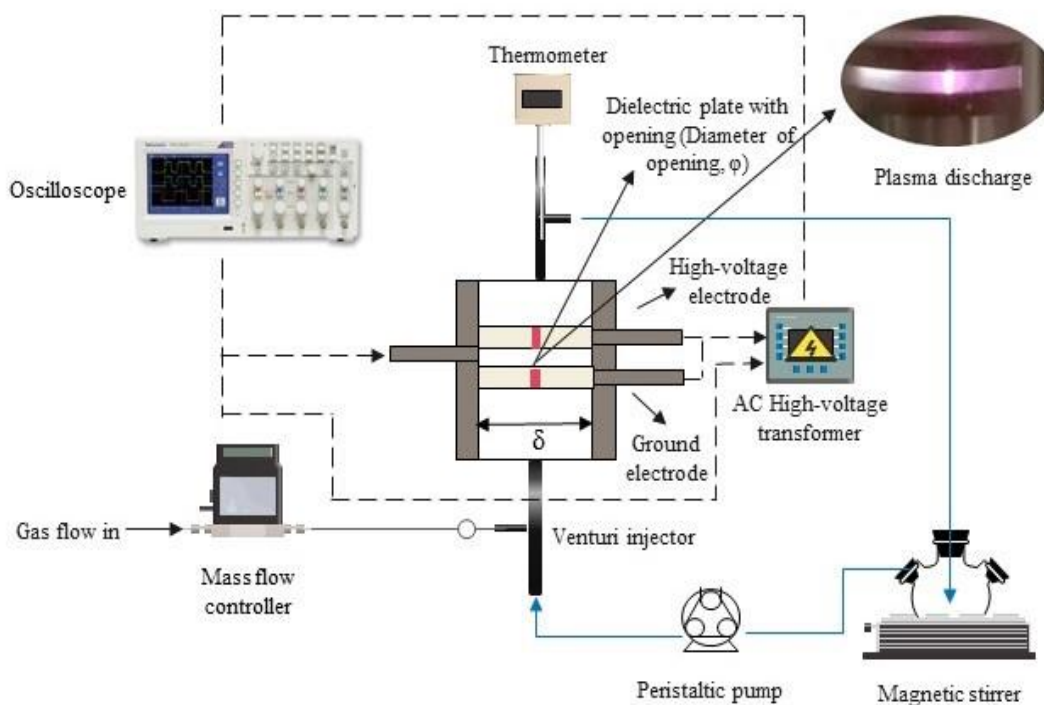


Figure 5.1. Schematic of the electrohydraulic discharge reactor system

Compared to the other two designs, the pin-to-pin and pin-to-plate electrohydraulic discharge reactors, this design had a unique feature of establishing a complete discharge through the conducting channel of the two electrodes. The small hole in the middle of the plate allowed electrons generated to be concentrated in the vicinity of the opening, and the discharge current continuity could be achieved in the form of mobile electrons in the plasma phase to obtain a better mass transfer and substrate molecules breakdown in contact with the plasma discharge. The voltage applied could be adjusted and read by a regulator (model#: TDGC2-2KM, ISE, Inc., Cleveland, OH). The voltage between the top electrode and the ground electrode was measured by a high voltage probe, and the discharge voltage traces were recorded and displayed by the oscilloscope (Tektronix, Beaverton, OR). Moreover, the system also included a peristaltic pump (Masterflex, Cole-Parmer, Vernon Hills, IL), which allowed for continuous movement of feedstock or solution through the reactor system. In

addition, a mass flow instrument (Smart-Trak, Sierra Instruments, Inc, Monterey, CA) is connected to the reactor to control the gas flow rate. This continuous operation design could significantly improve the quantity and capacity of the reactor system, therefore potentially reducing the operation costs and reactor size for commercial applications [149, 157].

5.2.5 Experimental procedures

All experiments were conducted based on the optimum conditions from chapter 4, i.e., argon flowrate 2.73 L/min and applied power 128.6W. A total volume of 100 mL of p-NP solution was used for each experimental run. Sodium sulfate was used to adjust the initial conductivity (65 $\mu\text{S}/\text{cm}$) of the solution. The solution was introduced through the EHPD reactor using a peristaltic pump via a three-neck flask connected to a condenser tube. The treated solution was then returned to the flask, allowing for continuous flow and mixing. The power was turned on once the solution had filled the discharge region. Argon gas was used for the initiation of plasma discharge. After each experimental run, the reactor system was flushed twice with distilled water. The initial and final pH and conductivity of p-NP was measured using conductivity and pH probes with a Hach HQ 440D multi-meter.

To investigate the p-NP degradation efficiency of the EHPD-catalysis system, three operational parameters were chosen for batch experiments: catalyst, catalyst dosage, and initial p-NP concentration. The first batch experiments were designed to investigate the effect of various catalyst BiOI and BiOI/C-BNQDsX (X= 1, 3, and 5 mL) on p-NP degradation efficiency. The catalyst dosage and initial concentration were set at 20 mg and 50 mg/L, respectively. The purpose of the second batch of experiments was to investigate the effect of catalyst dosage on p-NP degradation efficiency. Four catalyst dosages of 20 mg, 30 mg, 40 mg, and 50 mg were investigated using the best catalyst determined from the first batch experiments. The initial p-NP concentration, as well as other parameters such as solution volume, argon flowrate, and applied power, remained constant from the first batch experiments. Using the optimum conditions from the first and second batch experiments, the effect of initial p-NP concentrations of 10 mg/L, 25 mg/L, 50 mg/L, and 100 mg/L on p-NP degradation efficiency was evaluated in the third batch experiments. Likewise, the solution volume, argon flowrate, and applied power were all held constant. For each experimental run, the total treatment time was 10 minutes and samples were taken at one minute time intervals and the particles were separated using a 0.22 μm microporous membrane filter.

The samples were analyzed by measuring absorbance of p-NP using a UV-Vis spectrophotometer (Biotek Synergy HT) at 317 nm and the concentration of p-NP was calculated based on the standard curve. The degradation efficiency was calculated using eq 1.,

$$n = \frac{C_0 - C}{C_0} * 100 \quad (1)$$

$C_0 = \text{initial concentration}, C = \text{final concentration}$

The energy yield for degradation of p-NP was calculated using eq. 2. The yield value expressed the amount of pollutant converted divided by the energy input required at n% conversion of the pollutant [84]:

$$Y \text{ (g/kWh)} = \frac{C_0 * V_0 * n\% * \frac{1}{100}}{P * t} \quad (2)$$

where C_0 is the initial concentration of the pollutant in mg/l, V_0 is volume of treated solution in liters, n% is degradation efficiency at time t, P is average power dissipated in the discharge (kW), and t is the time (hr).

Total organic carbon of p-NP degradation in EHPD-catalysis system was measured by TOC kit and analyzed by Hach DR3900 laboratory spectrophotometer for water analysis.

$$\text{TOC (\%)} = (\text{TOC}_0 - \text{TOC}_t) / \text{TOC}_0 * 100 \quad (3)$$

where $\text{TOC}_0 = \text{TOC of initial solution}$ and $\text{TOC}_t = \text{TOC of the solution at time t}$.

H_2O_2 concentration was measured based on the reaction of H_2O_2 and titanil sulfate. The concentration of H_2O_2 was determined by measuring the absorbance at 407 nm in UV-vis spectrophotometer.

5.2.6 Radical scavenging experiments

To determine the role of active species produced during the EHPD process in p-NP degradation, ammonium oxalate (3mmol/L), ascorbic acid (3 mmol/L), sodium nitrate (3 mmol/L), and 10 mL diluted 2-propanol (100 mg/L) in distilled water were added to 50 mg/L p-NP to inhibit holes (h^+), superoxide radical (O_2^-), aqueous electrons (e^-_{aq}), and hydroxyl radical (OH^\bullet), respectively[183]. To compare with the scavenger-free experiment for p-NP degradation, the optimum conditions of EHPD-catalysis were used for all radical scavenging tests. The efficiency of p-NP degradation was determined using a UV-Vis spectrophotometer (Biotek Synergy HT) at 317 nm.

5.2.7 Analytical methods

LC-MS Data was acquired on a Waters Acquity UPLC interfaced with a Waters Xevo TQ MS triple quadrupole mass spectrometer. A reverse HPLC method was used with a 2.1 mm x 100 mm Hewlett-Packard Hypersil ODS column, with 5 μ m particle size which was maintained at 35°C. The Solvent A mobile phase was water with 0.1% formic acid and solvent B mobile phase was acetonitrile with 0.1% formic acid. The flow rate was 0.1 mL/min., and the injection volume was 10 μ L. Initial solvent composition was 80% solvent A and 20% solvent B, which was held isocratic for 1 min. following injection. A linear gradient was then initiated bringing the composition to 20% A and 80% B by 6 min. The composition was held isocratic for the next 2 minutes, returned to starting conditions over the next one minute, and allowed to equilibrate over the next 3 minutes. UV-vis absorption spectra were acquired between 200 to 500 nm on an Acquity Diode Array Detector. Mass spectrometry data was acquired in negative ion ESI mode using a capillary voltage of 2.4 kV and a cone voltage of 20 v. The desolvation temperature was 300°C and the desolvation gas (N₂) flow was 400 L/Hr. Total ion MS spectra were acquired between 50 and 350 Da at 1.5 sec/scan. Analytes of interest were identified from the resulting data by generating extracted ion chromatograms of expected analytes from the total ion chromatograms (TICs) and by identifying peaks in the TICs.

A Dionex Ion Analyzer (Dionex, Sunnyvale, CA) was used to detect inorganic ions in p-NP degradation with a GP40 gradient pump, an electrochemical detector and an auto sample AS40. The mobile phase consisted of 100 mM sodium hydroxide, with a volume of approximately 20 μ L. A temperature of 30°C and 300 mA were determined by the anion suppressor. The Inorganic Ion Check Standard (CertiPrep) was used as a reference to compare the products produced in the ion chromatography trace.

5.3 Results and discussion

5.3.1 Effect of various catalysts in EHPD system

Fig. 5.2 (a). presents the degradation efficiency of p-NP with various catalyst (20 mg dosage) in the EHPD system. The initial concentration of p-NP, argon flowrate and power were 50 mg/L, 2.73 L/min and 128.6 W, respectively. The addition of BiOI improved p-NP degradation efficiency by little, increasing it from 94.23 % to 94.60 % after 10 minutes of

treatment. When compared to pure BiOI, BiOI/C-BNQDsX (X= 1,3 and 5 mL) improves p-NP degradation efficiency in the EHPD system. The p-NP removal efficiency increases initially and then decreases as the weight ratio of C-BNQDs increased. When the C-BNQDs weight ratio was increased to 5 mL, the catalytic performance decreases while remaining higher than pure BiOI. The BiOI/C-BNQDs (3mL) has the highest catalytic performance in EHPD, and the corresponding removal efficiency can reach 96.17 % after 10 min of treatment, which is 2.48% higher than in plasma alone treatment. The addition of catalyst has an improvement in EHPD system showing synergistic effects. In fact, the degradation efficiency with plasma catalysis has a slight improvement when compared to plasma alone. It might be because, EHPD system has a good capability of producing different active species without the catalyst necessary for degrading p-NP.

The pseudo first-order kinetics of p-NP degradation was also examined to better understand the catalytic efficiency, as shown in Fig. 5.2.(b). BiOI, BiOI/C-BNQDs (1mL), BiOI/C-BNQDs (3 mL) and BiOI/C-BNQDs (5mL) have kinetic constants of 0.02939min^{-1} , 0.3075 min^{-1} , 0.3235 min^{-1} and 0.3027 min^{-1} , respectively. And the correlation coefficients were above 0.98 for all the catalyst, clearly indicating that the first order kinetic model agreed with the experimental data. Apparently, as the weight ratio of C-BNQDs increases, the kinetic constant first increases and then decreases, consistent with the removal efficiency trend. When C-BNQDs weight percentage is low, the C-BNQDs were able to transmit photoelectrons from BiOI CB after irradiated by visible light, allowing separation of electron-hole pair. As a result, BiOI/C-BNQDs materials in EHPD system show better degradation efficiency of p-NP. When the C-BNQDs level increased to 5 mL, too many C-BNQDs spread on the surface of BiOI would prevent it from absorbing visible light by covering its active sites. Similar was reported in many photocatalytic studies, Liu et al.[132], reported that the photocatalytic activity of BN/BiOI composites began to decline at concentrations greater than 1 wt%. It is possible that the excess BN covers the active sites of BiOI and reduces BiOI contact surface with light irradiation, resulting in the "shielding effect." Li et al., reported if there is too much BN on the BiOI surface, it will cover the active sites of the material, reducing its photocatalytic activity.

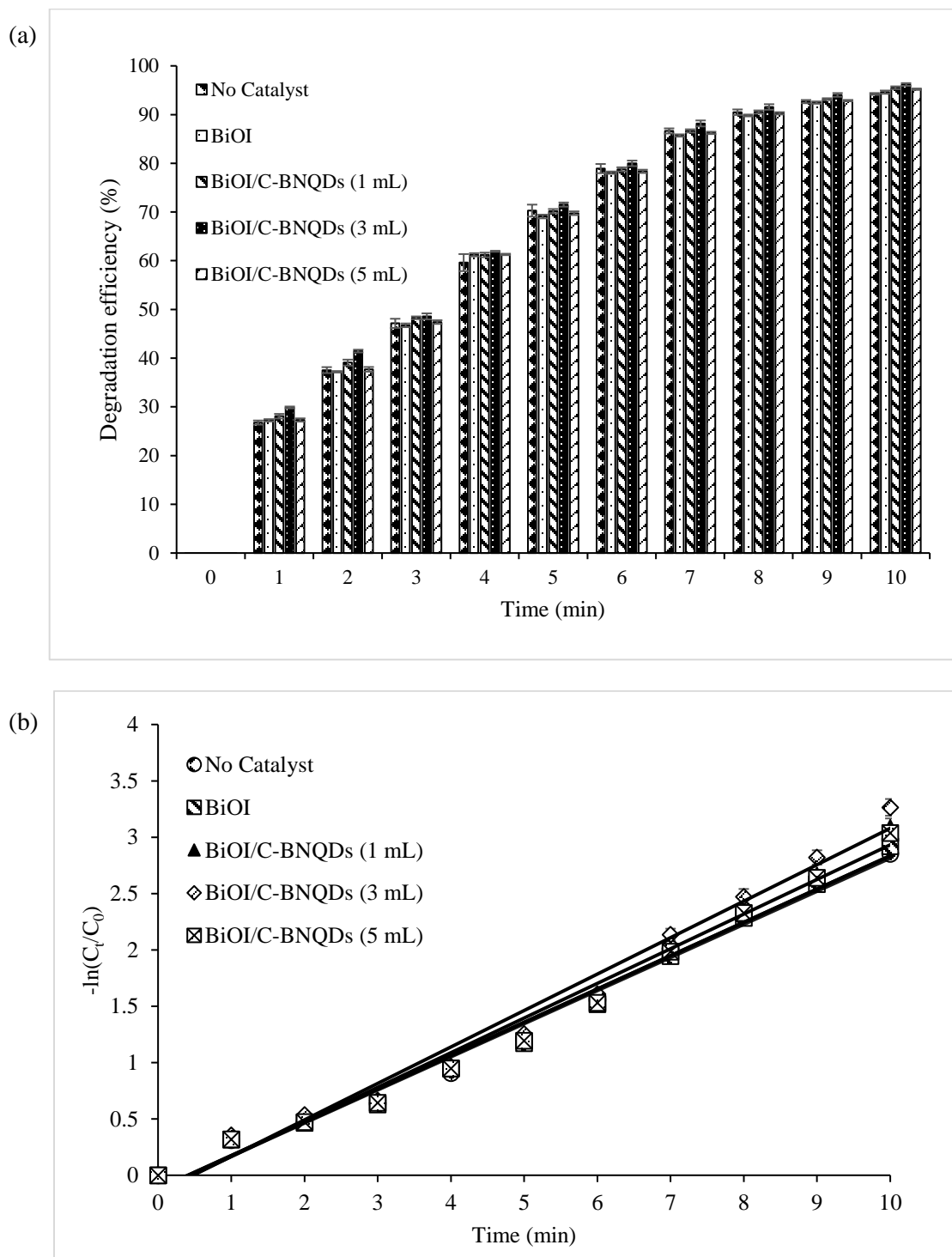


Figure 5.2. (a) Degradation efficiency of p-NP with BiOI and BiOI/C-BNQDsX (X =1, 3 and 5 mL) catalysts in EHPD system, (b) First order kinetics of p-NP degradation with BiOI and BiOI/C-BNQDsX (X =1, 3 and 5 mL) catalysts in EHPD system

5.3.2 Effect of catalyst dosage

From the various catalysts tested, BiOI/C-BNQDs (3mL) has shown the better degradation efficiency in the EHPD system. In this study, different catalyst dosages (20 mg, 30 mg, 40 mg and 50 mg) were tested on BiOI/C-BNQDs (3 mL) to investigate the optimal catalyst dosage in the EHPD system. The initial concentration, argon flow rate and power were kept same as the initial conditions, i.e., 50 mg/L, 2.73 L/min and 128.6 W, respectively. The BiOI/C-BNQDs (3mL) improved the p-NP degradation efficiency with increase in the catalyst dosage. Catalyst dosage with 30 mg have shown the highest degradation rate on the EHPD system. As shown in the figure 5.3 (a), increase in dosage varies from 94.23% (EHPD) to 96.17%, 98.01%, 97.14% and 95.37 after 10 min treatment with dosage of 20 mg, 30 mg, 40 mg and 50 mg, respectively. It was observed that further increasing the catalyst dosage limits the p-NP degradation. The catalyst dosage on EHPD system have shown great influence when compared to EHPD system alone (94.23%).

Moreover, the kinetic constant shown in Fig. 5.3 (b), improved from 0.2956 min^{-1} (EHPD alone) to 0.325 min^{-1} , 0.3788 min^{-1} , 0.3517 min^{-1} and 0.3067 min^{-1} respectively. p-NP degradation efficiency and kinetic constant increased at first and then decline with improving the BiOI/C-BNQDs (3mL) dosage. The most effective catalyst dosage was 30 mg. Similar phenomenon was observed by Guo. H et al. [212-214] stating that the increase in catalyst dosage increases the contact area between plasma and catalyst, causing more effective photons to convert into chemical energy and speeding up the catalytic activity. In contrast, when the dosage was greater than optimal dosage, the photons produced by EHPD were scattered and protected by catalyst, resulting in a reduction in luminous intensity and a loss of light energy. Moreover, it also limits the decomposition of H_2O_2 to $\cdot\text{OH}$, resulting in the decline of degradation efficiency.

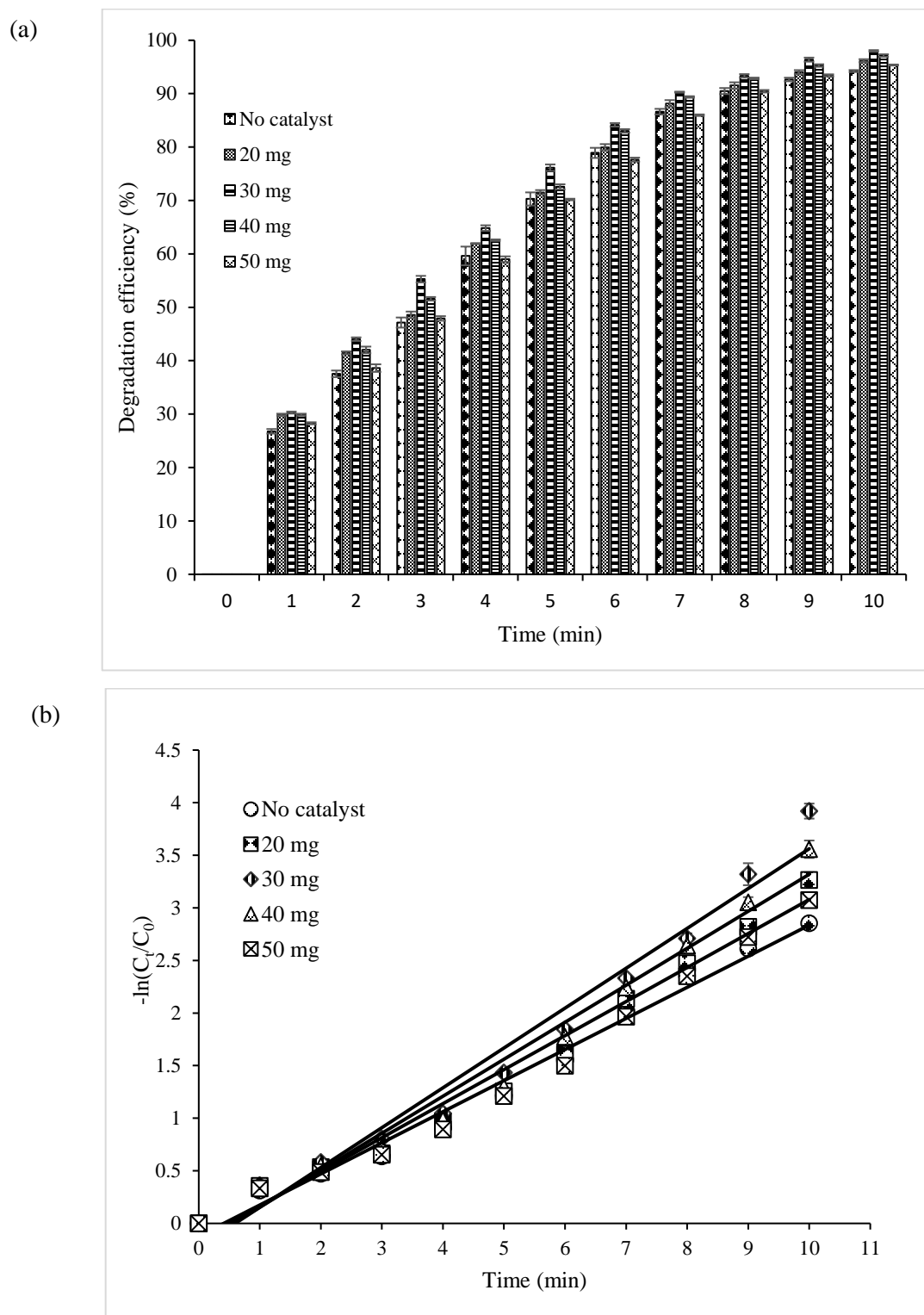


Figure 5.3. (a) Degradation efficiency of p-NP with different catalyst dosage of BiOI/C-BNQDs (3 mL) in EHPD system, (b) First order kinetics of BiOI/C-BNQDs (3 mL) catalyst dosage in EHPD system

5.3.3 Effect of initial p-NP concentration in EHPD-catalysis system

Based on influence of different operating parameters, the optimal catalyst BiOI/C-BNQDs (3mL) (BiCBN-3) and catalyst dosage (30 mg) were determined. These conditions were further used to investigate the effects of different initial p-NP concentrations (10 mg/L, 25 mg/L, 50 mg/L and 100 mg/L) in EHPD-catalysis system. Argon flow rate and power were same as the previous conditions. As shown in the Fig. 5.4 (a), at different initial p-NP concentrations (10 mg/L, 25 mg/L, 50 mg/L and 100 mg/L), the EHPD/BiCBN-3 system showed complete degradation efficiency for 10 mg/L within 7 min of treatment. While 25 mg/L was 100% degraded after 10 min of treatment. 50 mg/L and 100 mg/L showed almost 98.01% and 93.74 % p-NP degradation after 10 min treatment in EHPD/BiCBN-3 system. The complete degradation for 50 mg/L and 100 mg/L initial p-NP concentration was achieved after 11 min and 13 min, respectively.

Fig 5.4 (b) displays the results of kinetic constants, where it decreases with increase in concentration as follows: 0.6533 min^{-1} , 0.4702 min^{-1} , 0.3788 min^{-1} and 0.2528 min^{-1} for 10 mg/L, 25 mg/L, 50 mg/L and 100 mg/L, respectively. Increasing the initial p-NP concentration causes a decrease in p-NP degradation efficiency and kinetic constant. This might be due to active species produced which are insufficient to decompose all p-NP molecules at higher concentration, causing p-NP degradation efficiency to be inhibited. However, when compared with EHPD system (94.23%), EHPD/BiCBN-3 system showed an increase of 3.78% at initial p-NP concentration of 50 mg/L, indicating a better performance and effective degradation rate.

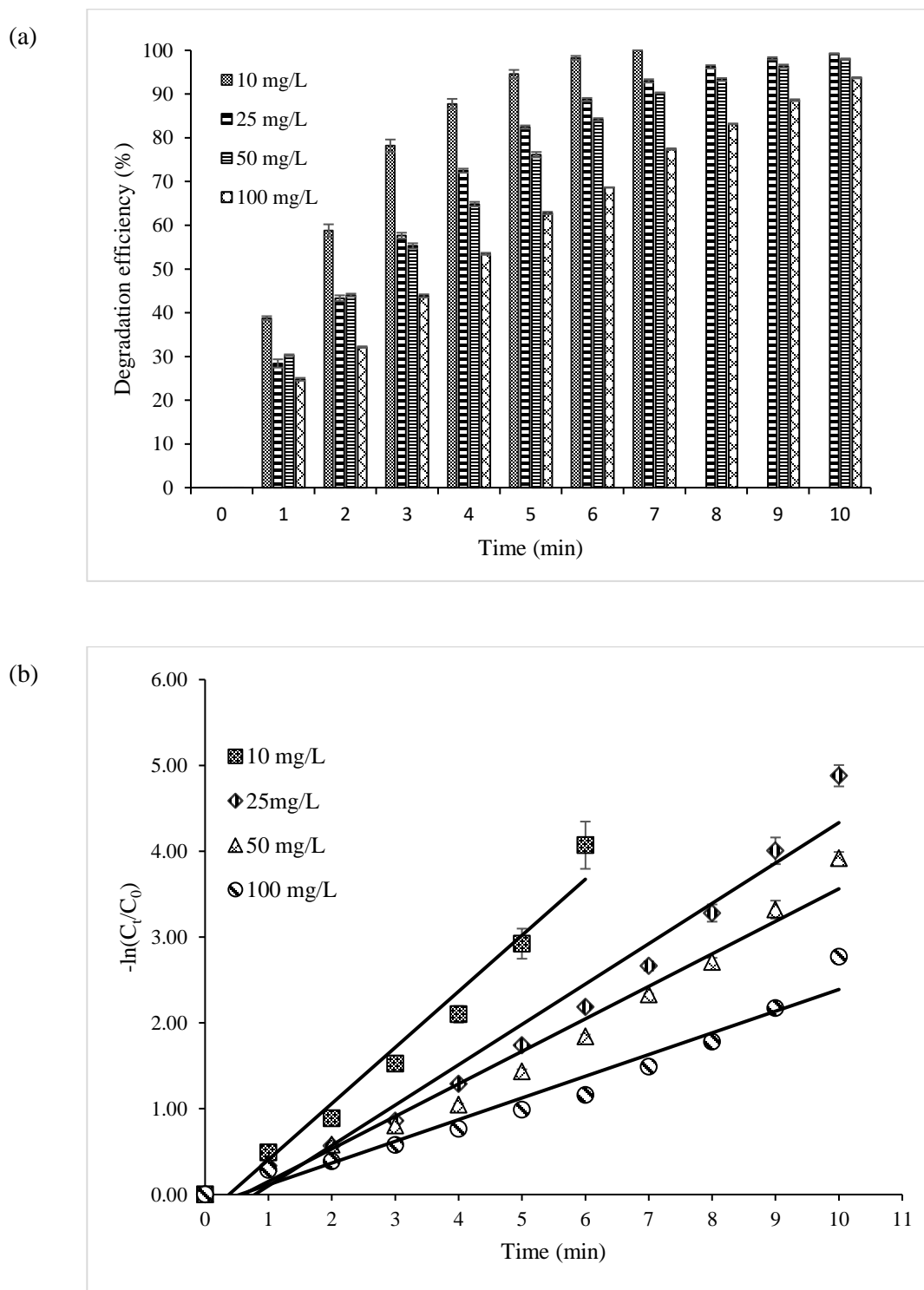


Figure 5.4. (a) Effect of initial p-NP concentrations degradation in EHPD/BiCBN-3 system and (b) First order kinetics of initial p-NP concentrations degradation in EHPD/BiCBN-3 system

5.3.4 Energy yield, TOC, pH, conductivity and H₂O₂

The energy yield of EHPD/BiCBN-3 system at different initial p-NP concentration under optimum conditions for 10 min treatment time were calculated by using eq (2). The results showed 0.07 g/kWh at 10 mg/L, 0.12 g/kWh at 25 mg/L, 0.23 g/kWh at 50 mg/L and 0.44 g/kWh at 100 mg/L, respectively. Therefore, the energy yield has an improved effect compared to the sole EHPD system.

The mineralization of p-NP in the aqueous solution was evaluated by measuring the total organic content (TOC) in EHPD/BiCBN-3 system. TOC was measured for different initial p-NP concentrations and mineralization efficiency was 86.77%, 80.55%, 78.08%, 67.40% after 10 min of treatment for 10 mg/L, 25 mg/L, 50 mg/L and 100 mg/L, respectively. When compared to EHPD process alone of 83.55%, 78.11%, 75.68% and 63.78% for corresponding 10 mg/L, 25 mg/L, 50 mg/L and 100 mg/L initial p-NP concentration, the mineralization efficiency increased in EHPD/BiCBN-3 showing synergistic effects of plasma-catalysis. As a result, BiOI/C-BNQDs (3 mL) could be said to contribute to the enhancement of mineralization. Furthermore, the TOC removal efficiency is lower than the degradation efficiency, indicating formation of intermediates during p-NP degradation.

Fig 5.5 depicts the changes in pH and conductivity of p-NP aqueous solution after EHPD-BiOI/C-BNQDs (3mL) treatment corresponding to initial p-NP concentrations of 10 mg/L, 25 mg/L, 50 mg/L, and 100 mg/L. In comparison to EHPD treatment (pH: 3.37-3.65 and conductivity: 184-245 μ S/cm), the presence of the catalyst in EHPD results in less acidification of the samples and a less pronounced increase in conductivity. In EHPD/BiCBN-3, final pH was in the range between 3.6 to 3.93. Whereas the final conductivity increased in proportion to the initial p-NP concentrations in the range of 175.2-228.9 μ S/cm. The above change may be attributed to the formation of acids and ions in p-NP degradation, as the reactive species of EHPD/BiCBN-3 breakdown the p-NP molecules.

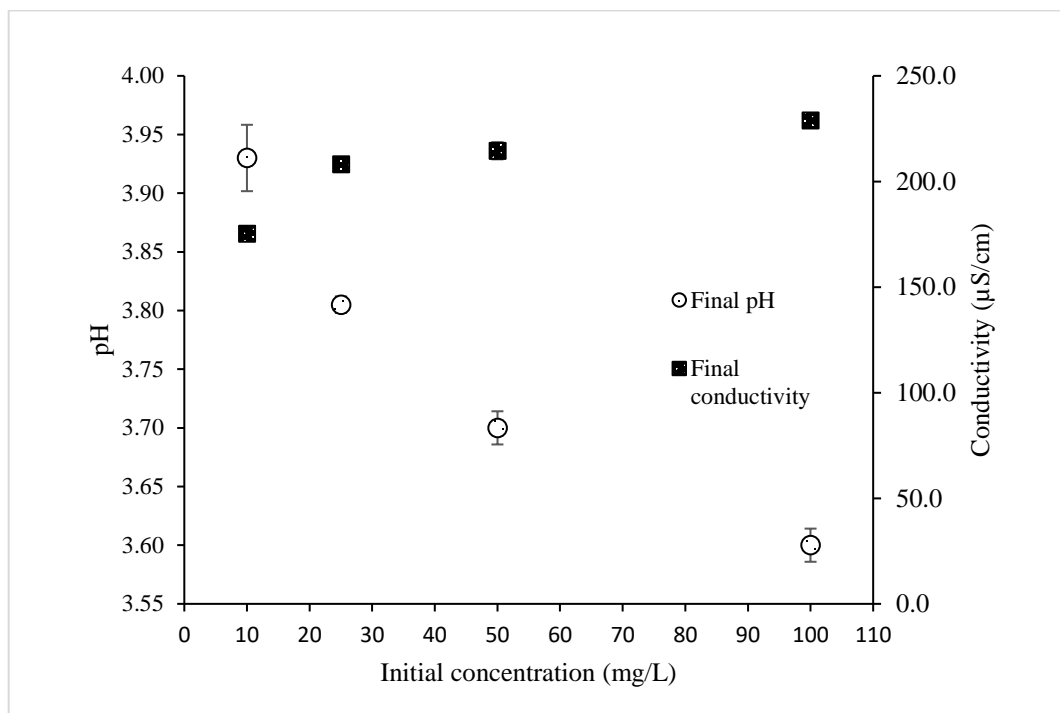


Figure 5.5. pH and conductivity for EHPD/BiCBN-3 system at different initial p-NP concentrations

H_2O_2 production of EHPD/BiCBN-3 system at different time intervals having an initial p-NP concentration of 50 mg/L and catalyst dosage of 30 mg was presented in Fig. 5.6. The concentration of H_2O_2 in p-NP solution in EHPD/BiCBN-3 was higher compared to EHPD system, indicating that H_2O_2 played a certain role for p-NP degradation. The H_2O_2 concentration after 10 min treatment was 229.03 mg/L. High amount of H_2O_2 , was due to the activation of photocatalyst surface by argon plasma would generate many holes (h^+) and electrons (e^-) that would react with water molecules to produce $\cdot OH$ radicals. Because of their short life, $\cdot OH$ radicals were quickly recombined to form H_2O_2 . Guo et al.[212], also reported that pulsed discharge plasma (PDP) combined with TiO_2/WO_3 composites showed high H_2O_2 production compared to sole PDP.

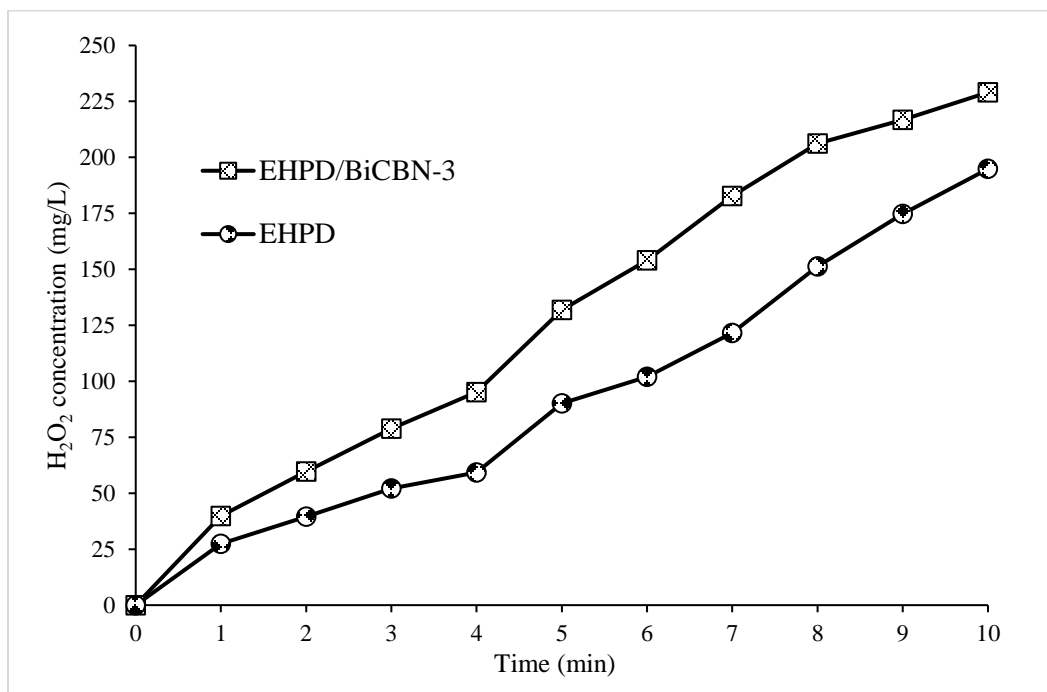


Figure 5.6. H_2O_2 concentration in EHPD/BiCBN-3 system at 50 mg/L p-NP concentration

5.3.5 Role of reactive species produced in EHPD/BiCBN-3 system

Optical emission spectroscopy was used to examine reactive species in EHPD/BiCBN-3 system. Fig 5.7. displays the OES spectra of EHPD/BiCBN-3 system under optimal conditions during the p-NP degradation. In the OES spectra, argon atomic (Ar I) system lines in the range of 690 to 965 nm were detected, corresponding to radiative de-excitations from the 4p and 4p' levels to the 4s levels. These gas-phase active species when interact with water molecules, it forms $\bullet\text{OH}$ and H. $\bullet\text{OH}$ radical species corresponding to the transition $\text{A}^2\Sigma^+ + (\nu''=0) - \text{X}^2\Pi(\nu''=0)$ were assigned to the emission line at 309.6 nm. Furthermore, atomic oxygen species at 777.03 and 844.13 nm as well as the H line of the Balmer series, H_α at 655.92 nm) and H_β at 486.16 nm have been identified [176, 179, 188, 189]. Compared to EHPD, emission peaks were similar, however the intensity of peaks was much higher in EHPD/BiCBN-3 system.

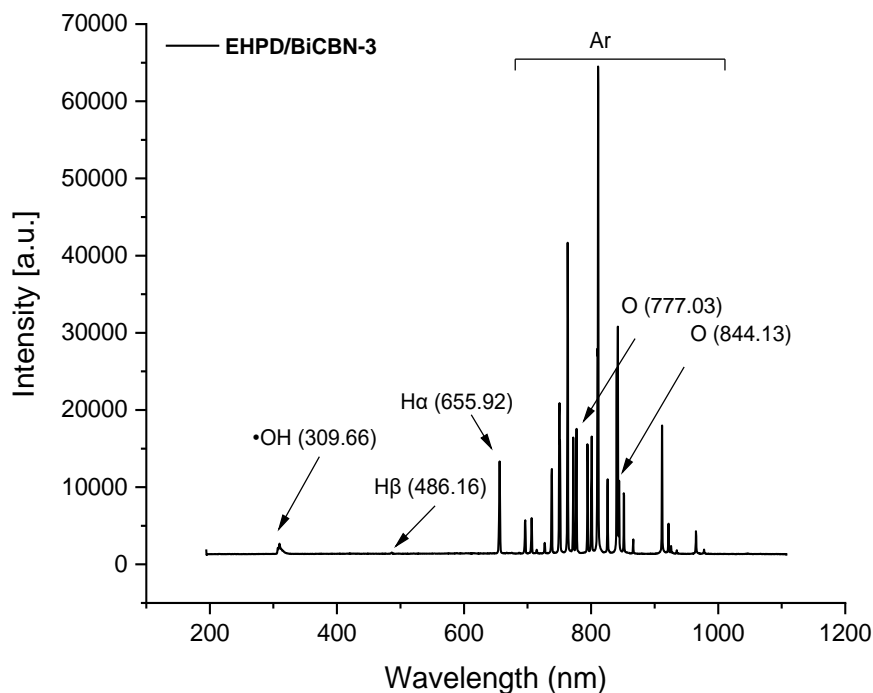


Figure 5.7. OES spectra of EHPD/BiCBN-3 system

In order to determine the role of various active species on p-NP degradation in the EHPD/BiCBN-3 system. Chemicals such as ammonium oxalate (AO), 2-propanol, ascorbic acid (AA) and sodium nitrate (NaNO_3) were used as scavengers for holes (h^+), hydroxyl radicals ($\cdot\text{OH}$), superoxide radicals ($\cdot\text{O}_2^-$) and hydrated electrons (e_{aq}^-), respectively. Scavenging agents were added to the EHPD/BiCBN-3 system and treated under optimal conditions such as 30 mg catalyst dosage, 2.73 L/min argon flow rate and 128.6W applied power at 50 mg/L initial p-NP concentration. When these scavenging agents were added, the p-NP degradation efficiency in EHPD/BiCBN-3 decreased compared to the no scavenger study. The degradation kinetics of the radical scavenging experiment were shown in Fig. 5.8. The results of degradation rate constants were in the order of $0.3788 > 0.2764 > 0.2236 > 0.1244 > 0.0822 \text{ min}^{-1}$ corresponding to the no scavenger $> \text{h}^+ > \text{e}_{\text{aq}}^- > \cdot\text{O}_2^- > \cdot\text{OH}$. Based on the results, $\cdot\text{OH}$ radicals were the main active species involved in EHPD/BiCBN-3 system for p-NP degradation. Moreover, $\cdot\text{O}_2^-$ radicals were the most second active, while the e_{aq}^- and h^+ showed little effect on p-NP degradation.

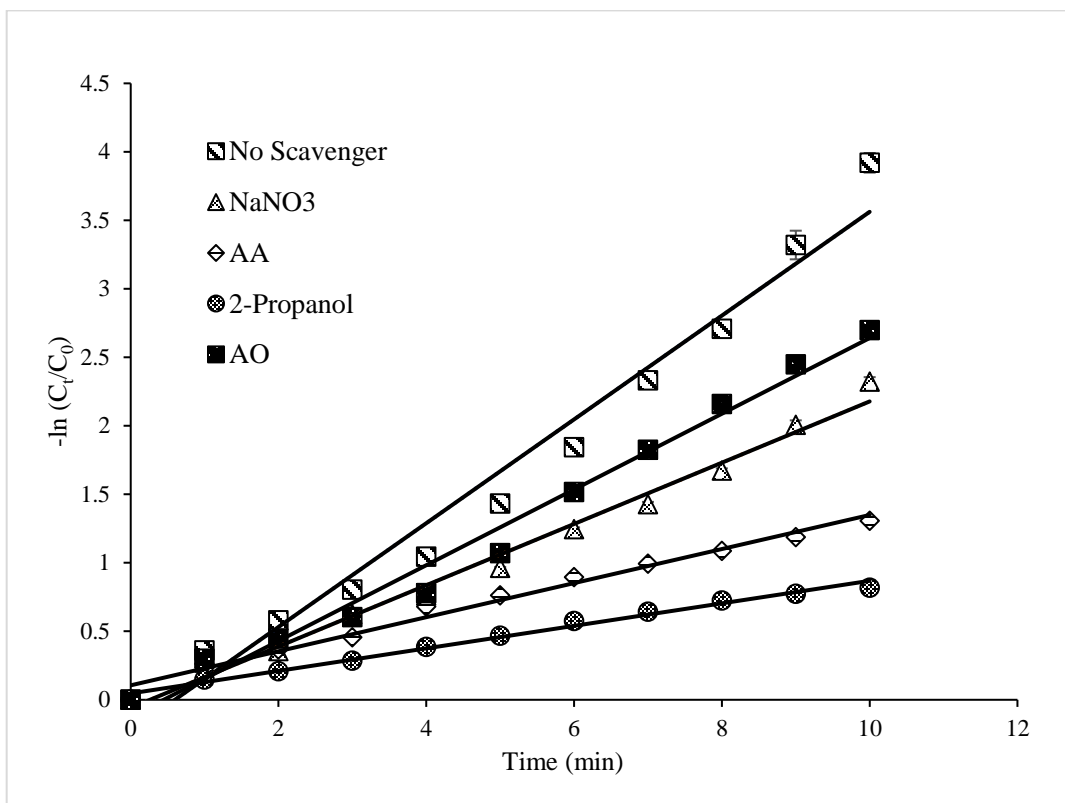
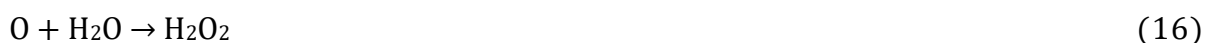
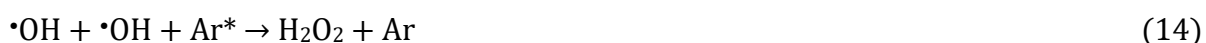
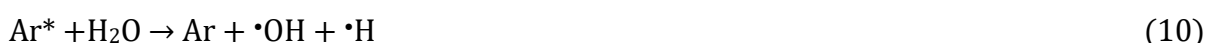


Figure 5.8. Role of active species by EHPD/BiCBN-3 at 50 mg/L p-NP initial concentration under 2.73 L/min and 128.6 W

5.3.6 Synergistic effects of EHPD/BiCBN-3 system

The addition of BiOI/C-BNQDs (3 mL) to the EHPD system showed effective increase in p-NP degradation. The photocatalyst was considerably accelerated by the EHPD process through a series of physical and chemical reactions. The BiOI/C-BNQDs (3 mL) photocatalyst may be efficiently activated by UV-vis irradiation and the heat created by the EHPD process, and electrons and reactive oxygen species in the plasma can also assist the photocatalyst in establishing electron transfer pathways that accelerate p-NP degradation. Here the electrons in BiOI valence band (VB) were excited and transferred to the conduction band (CB), leaving the corresponding holes behind in VB. The electrons generated on the CB of BiOI were transferred to the C-BNQDs, effectively separating photogenerated electron-hole pairs and limiting electron-hole pair recombination. The transferred electrons accumulated on the surface of C-BNQDs could reduce O_2 to generate $\cdot O_2^-$. Then, the $\cdot O_2^-$ and electrons react with the water to form hydrogen peroxide (H_2O_2), which undergoes further transformation to form $\cdot OH$ radicals. The holes in the VB can oxidize water, resulting in the

formation of $\cdot\text{OH}$ radicals. Furthermore, EHPD/BiCBN-3 system can result in lot of $\cdot\text{OH}$ production which helps in the faster and effective degradation of p-NP compared to sole EHPD system and photocatalyst. The synergistic mechanism of EHPD/BiCBN-3 system was stated in possible reaction pathway (eq: 4-18) [74, 215, 216].



5.3.7 Degradation pathway of p-NP using EHPD/BiCBN-3 system

The degradation intermediates generated during p-NP breakdown were analyzed using UPLC-MS/MS. The total ion chromatogram of p-NP degradation was illustrated in Fig. 5.9(a) and (b). The degradation pathway of p-NP treated under optimal conditions (30 mg catalyst dosage, 50 mg/L initial concentration, 2.73 L/min argon flow rate and 128.6 W power) in the EHPD/BiCBN-3 system was provided based on the identification results of p-NP degradation intermediates (Fig. 5.10). In EHPD/BiCBN-3 system, the intermediates were found to be 4-nitrocatechol and 4-nitropyrogallol. The primary reaction pathway was hydroxylation of p-NP through interaction of $\cdot\text{OH}$ via electrophilic reaction on the aromatic rings, which produces p-nitrocatechol ($m/z=154$). Here the phenolic ^-OH group contributes electrons to the electrophilic aromatic substitution, whereas the $^-\text{NO}_2$ group to electron-

withdrawing. Therefore, the electron-donating substituents increase the electron density in the ortho and para positions, whereas electron-withdrawing substituents are highly deactivating and meta-directing. When both substituents (-OH and -NO₂) are present, electrophilic attack prefers ortho and para positions relative to the -OH group [196, 217]. Therefore, subsequent [•]OH radicals attack on p-nitrocatechol transforms into p-nitropyrogallol (m/z=170). Further oxidation of p-nitropyrogallol results in the breakdown of aromatic ring openings and forms aliphatic acids like oxalic acid or acetic acid or formic acid [178, 197]. Finally, the intermediates of p-NP degradation mineralized to NO₂⁻, NO₃⁻, H₂O and CO₂ as end products. The large peak after 10 min of treatment around retention time 1.6 min in Fig 5.9 (b) was an inorganic material derived from sodium sulfate.

Ion chromatography analysis of 50 mg/L p-NP treated under optimal conditions in the EHPD/BiCBN-3 system revealed that nitrate, nitrite, and sulfate were present in trace amounts due to the breakdown of p-NP molecules. While the sulfate concentration was relatively high (40.2 mg/L), nitrate concentration was 13.9 mg/L and nitrite concentration was 1.2 mg/L after 10 min treatment time. Due to the addition of sodium sulfate to adjust the initial conductivity of the p-NP aqueous solution, the sulfate concentration was elevated.

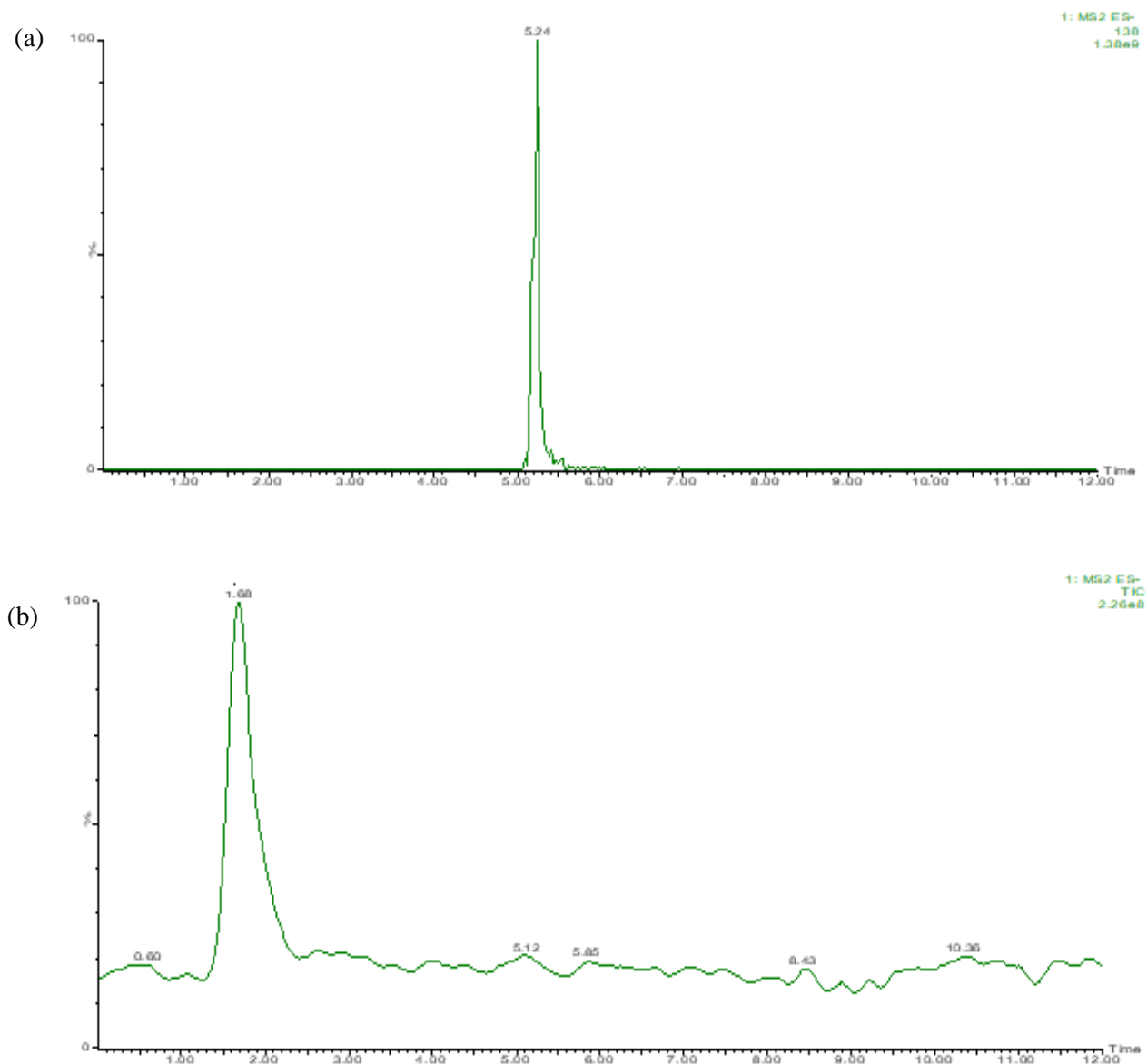


Figure 5.9. (a) Total ion chromatogram (TIC) of initial p-NP concentration 50 mg/L and (b) p-NP after 10 min treatment in EHPD/BICBN-3 system

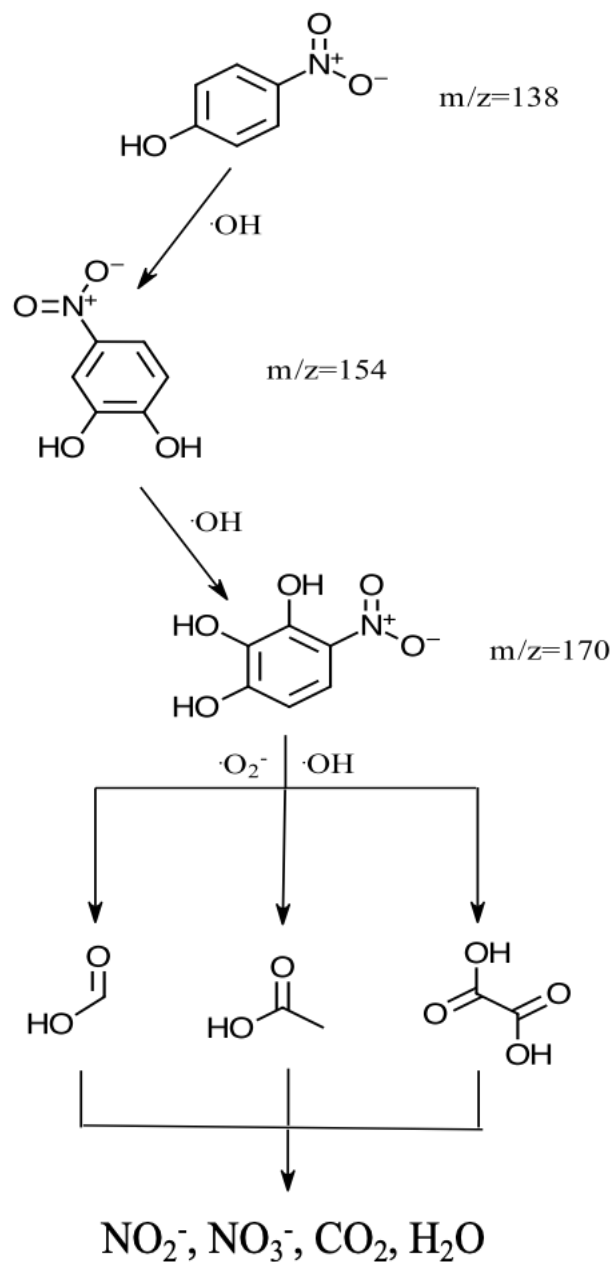


Figure 5.10. Degradation pathway of EHPD/BiCBN-3 system

5.4 Conclusions

In this study, EHPD combined with BiOI/C-BNQDs achieved synergistic degradation of p-NP in water. The optimal catalyst was found to be BiOI/C-BNQDs (3 mL) with a catalyst dosage of 30 mg, showing 98.01% p-NP degradation efficiency within 10 min of treatment for 50 mg/L initial concentration. The energy yield, TOC mineralization rate and

the H_2O_2 concentration were 0.23 g/kWh, 78.08%, and 229.03 mg/L, respectively. The OES spectra identified the reactive species such as $\cdot\text{OH}$ radicals, atomic oxygen species, argon atoms, and hydrogen lines of Balmer series to be present during the EHPD/BiCBN-3 treatment. Radical scavenging experiment confirmed $\cdot\text{OH}$ radicals as the main active species for p-NP degradation. The degradation efficiency, kinetic constant, H_2O_2 concentration, TOC removal and energy yield were all greater in the EHPD/BiCBN-3 system than in the EHPD system alone. The synergistic mechanism and degradation pathway of p-NP in EHPD/BiCBN-3 system was proposed. The presence of the BiOI/C-BNQDs (3mL) photocatalyst in the EHPD process can influence the role of the oxidizing species most responsible for the degradation of p-NP. Moreover, the catalyst needs shorter reaction time to activate in EHPD, resulting in formation of highly reactive species. Therefore, EHPD-catalysis technology is a promising approach for the degradation of organic pollutants in water.

CHAPTER 6 SUMMARY AND FUTURE PERSPECTIVES

The presented PhD dissertation was focused on the influence of continuous-flow electrohydraulic plasma discharge (EHPD) and EHPD-catalysis processes for the degradation of organic pollutants in water. Azo dye such as methylene blue (MB) and phenolic compound such as p-Nitrophenol (p-NP) were used as model organic pollutants. The effect of different operating parameters for both processes were evaluated and the best optimal conditions were determined to achieve maximum treatment efficiency. It was observed that both EHPD and EHPD-catalysis processes have shown efficient degradation and mineralization of MB and p-NP in water. The research was divided into four main parts and on basing of experimental results, the important findings may be summarized as follows:

In the first part, a novel BiOI/C-BNQDsX (X=1, 3 and 5 mL) photocatalyst was successfully prepared using a facile method. Under visible light irradiation, the BiOI/C-BNQDsX composites exhibits excellent photocatalytic activity for p-NP degradation. In comparison to pure BiOI and other weight contents, the photocatalytic activity of BiOI/C-BNQDs (3 mL) sample demonstrated a high degradation rate of 95.7% for p-NP and a TOC mineralization rate of 65.56% after 180 minutes of irradiation. Moreover, the BiOI/C-BNQDs (3 mL) catalyst showed good photostability for p-NP degradation under visible light irradiation. XPS analysis revealed the coexistence of BiOI and C-BN and HRTEM revealed that C-BNQDs were uniformly distributed across the surface of BiOI nanosheets. The results of active species trapping experiments revealed superoxide radicals played a major role followed by photogenerated holes and hydroxyl radicals in the photocatalytic degradation of p-NP. This study has developed a promising potential photocatalyst for the removal of organic pollutants under visible light.

The objective of second part was to investigate the operational parameters and explore the potential application of EHPD process for MB degradation. Air was used as carrier gas to initiate the plasma. The results showed a complete degradation of MB within 10 minutes of the treatment time. Evaluating operating parameters, such as liquid flow and air flow rates, revealed an optimum reactor conditions of 68 mL/min and 3L/min. Changes in initial dye concentration influenced degradation rate, indicating that degradation efficiency was higher at lower concentrations than at higher concentrations. Almost 90% of dye was degraded after 5 min of treatment even at higher concentrations. COD removal efficiency

showed 92.5% after 10 min of treatment for 100 mg/L initial MB concentration. The comparison experiments indicated that the EHPD treatment was preferable compared to other plasma processes. MB degradation followed first order kinetics and the energy yield at 50% conversion was range in between 0.16 g/kWh -0.81g/kWh for different operational parameters. Hydroxyl radicals were found to play significant role in degradation of MB based on radical scavenging experiment. The degradation intermediates were identified using UPLC-MS/MS and the degradation mechanism was proposed. Moreover, major production of nitrate and H₂O₂ were confirmed in the treated solution.

In the third part, argon gas was used to activate the EHPD process for p-NP degradation in aqueous solution. The most important operational factors of the EHPD process were screened using FFD. The FFD showed argon and power as significant factors for EHPD process. They were predicted and optimized using Response Surface Methodology (RSM) based on CCD. It was sufficient to model and optimize argon and power effects on degradation efficiency and energy yield. The degradation efficiency R² value was 0.9536 and the energy yield R² was 0.9982, which agreed with the adjusted R² values (0.9204 and 0.9970). It was found that 2.73 L/min argon flow rate and 128.6 W applied power yielded maximum degradation efficiency of 92.73% and energy yield of 0.212 g/kWh for this process. An optimized experiment was run to validate the model. Within 10 minutes of treatment, the model predicted 94.23 percent degradation efficiency and 0.22 g/kWh energy yield at 50 mg/L initial p-NP concentration. Increasing initial p-NP concentrations (10 mg/L, 25 mg/L, 50 mg/L, and 100 mg/L) slowed degradation rates. TOC mineralization efficiency was 75.68% for a 50 mg/L initial p-NP concentration of H₂O₂ concentration was 194.83 mg/L. Moreover, OES spectra and radical trapping experiments were conducted, and hydroxyl radicals were found to play a major role for p-NP degradation followed by other reactive species. On the basis of the intermediate products, electrophilic reactions by [•]OH radicals could degrade p-NP by oxidizing nitroaromatic rings and mineralizing them into inorganic ions (NO_x) or smaller organic compounds like CO₂. Thus, under optimal conditions, the results showed effective p-NP decomposition and better energy yield than previous studies, indicating EHPD as a potential wastewater treatment technology.

In the final part, the performance of the EHPD process for p-NP degradation was found to increase on addition of BiOI/C-BNQDs catalyst. The degradation results showed

that EHPD could induce BiOI/C-BNQDs photocatalysis successfully, and a synergetic effect was established in EHPD-catalysis system. The degradation efficiency, kinetic constant and energy yield were further improved with BiOI/C-BNQDs (3 mL) compared to BiOI and other weight content catalysts. The EHPD/BiCBN-3 showed the highest removal efficiency of p-NP enhanced from 94.23% to 98.01% within 10 min of treatment for 50 mg/L initial concentration under optimal conditions of 2.73 L/min argon flow rate and 128.6 W applied power. The degradation efficiency of p-NP increased firstly and then declined with increasing catalyst dosage, and the dosage was optimized as 30 mg. When compared with EHPD process, EHPD/BiCBN-3 system showed high H₂O₂ concentration and TOC mineralization efficiency. The high amount of H₂O₂ was due to the photocatalyst surface being activated by argon plasma, which produced many holes (h⁺) and electrons (e⁻) that reacted with water molecules to make [•]OH radicals. [•]OH radicals were swiftly recombined to create H₂O₂ due to their short life. Based on the active species trapping experiment, [•]OH radicals were the main active species involved in EHPD/BiCBN-3 system for p-NP degradation. Moreover, [•]O₂⁻ radicals were the most second active, while the e⁻_{aq} and h⁺ showed minimal effect on p-NP degradation. The degradation mechanism was similar to the EHPD process, where electrophilic reactions by [•]OH attack in conjunction with oxidative ring opening reactions and final mineralization into NO₂⁻, NO₃⁻, SO₄²⁻, H₂O and CO₂ as end products in order to achieve complete breakdown of the p-NP molecules. The presence of catalyst in EHPD system showed better performance compared to EHPD alone. However, the overall results indicated both EHPD and EHPD-catalysis system as the most promising technologies used for the degradation of organic pollutants in wastewater.

Future research should focus on the economic evaluation of these processes, as the operational costs of the EHPD and EHPD-catalysis limits its industrial development. As a result, determining operational costs is an important stage in the commercialization of the process. In addition, understanding the different interactions between plasma and catalyst are crucial, as both influence each other. To adjust these interactions, it is important to modify the parameters of both the plasma and the catalyst. Fluid dynamical effects are also necessary to understand the radical transport and production rates in plasma system. Further, catalyst arrangement should be improved, for easy separation and reusability of the catalyst in plasma system. Type of electrode material is another critical parameter that can influence the

performance of the plasma system. Therefore, role of different electrodes on system performance should be investigated.

The proposed EHPD, when combined with catalysis, could provide a cost-effective and energy-efficient wastewater cleanup solution. With further improvements to the reactor design, system optimization, and careful design and selection of catalysts, this EHPD process can be scaled up and extended into new applications such as nitrogen fixation, decontaminate or sterilize biofilms, cancer cells destruction induced by plasma activated media, microbial decontamination, virus inactivation and ready-to-eat food treatment and food packaging.

REFERENCES

1. Al-Khalid, T., R. Surkatti, and M.H. El-Naas, Organic Contaminants in Industrial Wastewater: Prospects of Waste Management by Integrated Approaches, in Combined Application of Physico-Chemical & Microbiological Processes for Industrial Effluent Treatment Plant, M. Shah and A. Banerjee, Editors. 2020, Springer Singapore: Singapore. p. 205-235.
2. Rashed, M.N., Adsorption technique for the removal of organic pollutants from water and wastewater. *Organic pollutants-monitoring, risk and treatment*, 2013: p. 167-194.
3. Al-Ghouti, M.A., et al., Produced water characteristics, treatment and reuse: A review. *Journal of Water Process Engineering*, 2019. **28**: p. 222-239.
4. Bharagava, R.N., G. Saxena, and S.I. Mulla, Introduction to Industrial Wastes Containing Organic and Inorganic Pollutants and Bioremediation Approaches for Environmental Management, in *Bioremediation of Industrial Waste for Environmental Safety: Volume I: Industrial Waste and Its Management*, G. Saxena and R.N. Bharagava, Editors. 2020, Springer Singapore: Singapore. p. 1-18.
5. Kucharzyk, K.H., et al., Novel treatment technologies for PFAS compounds: A critical review. *Journal of Environmental Management*, 2017. **204**: p. 757-764.
6. Rana, R.S., et al., A review on characterization and bioremediation of pharmaceutical industries' wastewater: an Indian perspective. *Applied water science*, 2017. **7**(1): p. 1-12.
7. Schwarzenbach, R.P., et al., Global Water Pollution and Human Health. *Annual Review of Environment and Resources*, 2010. **35**(1): p. 109-136.
8. Joel, E.B., et al., Peroxidase from waste cabbage (*Brassica oleracea capitata* L.) exhibits the potential to biodegrade phenol and synthetic dyes from wastewater. *Scientific African*, 2020. **10**: p. e00608.
9. Garg, S., et al., *Prosopis juliflora* peroxidases for phenol remediation from industrial wastewater—An innovative practice for environmental sustainability. *Environmental Technology & Innovation*, 2020: p. 100865.
10. Islam, M.R. and M.G. Mostafa, Textile Dyeing Effluents and Environment Concerns- A Review. *Journal of Environmental Science and Natural Resources*, 2018. **11**(1-2): p. 131-144.
11. Massima Mouele, E.S., et al., Spectroscopic Measurements of Dissolved O₃, H₂O₂ and OH Radicals in Double Cylindrical Dielectric Barrier Discharge Technology: Treatment of Methylene Blue Dye Simulated Wastewater. *Plasma*, 2020. **3**(2).
12. Safardoust-Hojaghan, H. and M. Salavati-Niasari, Degradation of methylene blue as a pollutant with N-doped graphene quantum dot/titanium dioxide nanocomposite. *Journal of Cleaner Production*, 2017. **148**: p. 31-36.
13. Kumar, M.S., S.H. Sonawane, and A.B. Pandit, Degradation of methylene blue dye in aqueous solution using hydrodynamic cavitation based hybrid advanced oxidation processes. *Chemical Engineering and Processing: Process Intensification*, 2017. **122**: p. 288-295.
14. Lei, Y., et al., Facile preparation of sulfonic groups functionalized Mxenes for efficient removal of methylene blue. *Ceramics International*, 2019. **45**(14): p. 17653-17661.

15. Nguyen, C.H., C.-C. Fu, and R.-S. Juang, Degradation of methylene blue and methyl orange by palladium-doped TiO₂ photocatalysis for water reuse: Efficiency and degradation pathways. *Journal of Cleaner Production*, 2018. **202**: p. 413-427.
16. Tchieno, F.M.M. and I.K. Tonle, p-Nitrophenol determination and remediation: an overview. *Reviews in Analytical Chemistry*, 2018. **37**(2).
17. Rodrigues, C.S.D. and L.M. Madeira, p-Nitrophenol degradation by activated persulfate. *Environmental Technology & Innovation*, 2020: p. 101265.
18. Luo, J., et al., Preparation of a Magnetic Molecularly Imprinted Graphene Composite Highly Adsorbent for 4-Nitrophenol in Aqueous Medium. *ACS Sustainable Chemistry & Engineering*, 2016. **4**(6): p. 3316-3326.
19. Research Watch: Nitrophenol toxicity. *Environmental Science & Technology*, 1997. **31**(6): p. 259A-259A.
20. Cao, H.-L., et al., Ultrafine silver nanoparticles supported on a conjugated microporous polymer as high-performance nanocatalysts for nitrophenol reduction. *ACS Applied Materials & Interfaces*, 2017. **9**(6): p. 5231-5236.
21. Yadav, V., et al., Photodegradation of 4-nitrophenol over B-doped TiO₂ nanostructure: effect of dopant concentration, kinetics, and mechanism. *Environmental Science and Pollution Research*, 2020. **27**(10): p. 10966-10980.
22. Hama Aziz, K.H., et al., Application of a planar falling film reactor for decomposition and mineralization of methylene blue in the aqueous media via ozonation, Fenton, photocatalysis and non-thermal plasma: A comparative study. *Process Safety and Environmental Protection*, 2018. **113**: p. 319-329.
23. Lai, B., et al., Removal of p-nitrophenol (PNP) in aqueous solution by the micron-scale iron–copper (Fe/Cu) bimetallic particles. *Applied Catalysis B: Environmental*, 2014. **144**: p. 816-830.
24. Papić, S., et al., Decolourization and mineralization of commercial reactive dyes by using homogeneous and heterogeneous Fenton and UV/Fenton processes. *Journal of Hazardous Materials*, 2009. **164**(2): p. 1137-1145.
25. Chandana, L., P. Manoj Kumar Reddy, and C. Subrahmanyam, Atmospheric pressure non-thermal plasma jet for the degradation of methylene blue in aqueous medium. *Chemical Engineering Journal*, 2015. **282**: p. 116-122.
26. Deng, Y. and R. Zhao, Advanced Oxidation Processes (AOPs) in Wastewater Treatment. *Current Pollution Reports*, 2015. **1**(3): p. 167-176.
27. Ikehata, K., M. Gamal El-Din, and S.A. Snyder, Ozonation and advanced oxidation treatment of emerging organic pollutants in water and wastewater. *Ozone: Science and Engineering*, 2008. **30**(1): p. 21-26.
28. Umar, M. and H.A. Aziz, Photocatalytic degradation of organic pollutants in water. *Organic pollutants-monitoring, risk and treatment*, 2013. **8**: p. 196-197.
29. Martins, R.C. and R.M. Quinta-Ferreira, Remediation of phenolic wastewaters by advanced oxidation processes (AOPs) at ambient conditions: Comparative studies. *Chemical Engineering Science*, 2011. **66**(14): p. 3243-3250.
30. Ceriani, E., et al., Complete mineralization of organic pollutants in water by treatment with air non-thermal plasma. *Chemical Engineering Journal*, 2018. **337**: p. 567-575.
31. Iervolino, G., V. Vaiano, and V. Palma, Enhanced removal of water pollutants by dielectric barrier discharge non-thermal plasma reactor. *Separation and Purification Technology*, 2019. **215**: p. 155-162.

32. Jiang, B., J. Zheng, and M. Wu, Chapter 13 - Nonthermal Plasma for Effluent and Waste Treatment, in *Cold Plasma in Food and Agriculture*, N.N. Misra, O. Schlüter, and P.J. Cullen, Editors. 2016, Academic Press: San Diego. p. 309-342.
33. Dobrin, D., et al., Degradation of diclofenac in water using a pulsed corona discharge. *Chemical Engineering Journal*, 2013. **234**: p. 389-396.
34. Shang, K., et al., Generation Characteristics of Long-Lived Active Species in a Water Falling Film DBD Reactor. *Plasma Chemistry and Plasma Processing*, 2020.
35. Murugesan, P., J.A. Moses, and C. Anandharamakrishnan, Water decontamination of using non-thermal plasma: Concepts, applications, and prospects. *Journal of Environmental Chemical Engineering*, 2020: p. 104377.
36. Locke, B.R., et al., Electrohydraulic Discharge and Nonthermal Plasma for Water Treatment. *Industrial & Engineering Chemistry Research*, 2006. **45**(3): p. 882-905.
37. Lukes, P., et al., Aqueous-phase chemistry and bactericidal effects from an air discharge plasma in contact with water: evidence for the formation of peroxyxynitrite through a pseudo-second-order post-discharge reaction of H₂O₂ and HNO₂. *Plasma Sources Science and Technology*, 2014. **23**(1): p. 015019.
38. Zeghioud, H., et al., Review on discharge Plasma for water treatment: mechanism, reactor geometries, active species and combined processes. *Journal of Water Process Engineering*, 2020. **38**: p. 101664.
39. Bansode, A.S., et al., Effective degradation of organic water pollutants by atmospheric non-thermal plasma torch and analysis of degradation process. *Chemosphere*, 2017. **167**: p. 396-405.
40. Huang, Q. and C. Fang, Degradation of 3,3',4,4'-tetrachlorobiphenyl (PCB77) by dielectric barrier discharge (DBD) non-thermal plasma: Degradation mechanism and toxicity evaluation. *Science of The Total Environment*, 2020. **739**: p. 139926.
41. Wang, J., et al., Degradation of phenolic compounds by dielectric barrier plasma: Process optimization and influence of phenol substituents. *Chemical Engineering Journal*, 2020. **385**: p. 123732.
42. Rodríguez-Padrón, D., et al., Environmental catalysis: present and future. *ChemCatChem*, 2019. **11**(1): p. 18-38.
43. Lee, S.-Y. and S.-J. Park, TiO₂ photocatalyst for water treatment applications. *Journal of Industrial and Engineering Chemistry*, 2013. **19**(6): p. 1761-1769.
44. Belver, C., et al., Chapter 22 - Semiconductor Photocatalysis for Water Purification, in *Nanoscale Materials in Water Purification*, S. Thomas, et al., Editors. 2019, Elsevier. p. 581-651.
45. Zhang, S., et al., In situ synthesis of water-soluble magnetic graphitic carbon nitride photocatalyst and its synergistic catalytic performance. *ACS Appl Mater Interfaces*, 2013. **5**(23): p. 12735-43.
46. Muid Julkapli, N., S. Bagheri, and S. Bee Abd Hamid, Recent advances in heterogeneous photocatalytic decolorization of synthetic dyes. *The Scientific World Journal*, 2014. **2014**.
47. Gao, C., et al., Coordination chemistry in the design of heterogeneous photocatalysts. *Chemical Society Reviews*, 2017. **46**(10): p. 2799-2823.
48. Astruc, D., Transition-metal nanoparticles in catalysis: from historical background to the state-of-the art. *Nanoparticles and catalysis*, 2008. **16**: p. 1-48.

49. Philippot, K. and P. Serp, Concepts in nanocatalysis. *Nanomaterials in Catalysis*, 2013. **1**: p. 1-54.
50. Yang, C.C. and Y.-W. Mai, Thermodynamics at the nanoscale: A new approach to the investigation of unique physicochemical properties of nanomaterials. *Materials Science and Engineering: R: Reports*, 2014. **79**: p. 1-40.
51. Neyts, E.C., et al., Plasma Catalysis: Synergistic Effects at the Nanoscale. *Chemical Reviews*, 2015. **115**(24): p. 13408-13446.
52. Wellia, D.V., et al., Introduction of Nanomaterials for Photocatalysis, in *Nanocomposites for Visible Light-induced Photocatalysis*, M.M. Khan, D. Pradhan, and Y. Sohn, Editors. 2017, Springer International Publishing: Cham. p. 1-17.
53. Liu, H., et al., Bismuth oxyiodide-graphene nanocomposites with high visible light photocatalytic activity. *Journal of colloid and interface science*, 2013. **398**: p. 161-167.
54. Prihod'ko, R.V. and N.M. Soboleva, Photocatalysis: oxidative processes in water treatment. *Journal of Chemistry*, 2013. **2013**.
55. Fosso-Kankeu, E., S. Pandey, and S.S. Ray, *Photocatalysts in Advanced Oxidation Processes for Wastewater Treatment*. 2020: Wiley Online Library.
56. Sarkar, S. and K.K. Chattopadhyay, Visible light photocatalysis and electron emission from porous hollow spherical BiVO₄ nanostructures synthesized by a novel route. *Physica E: Low-dimensional Systems and Nanostructures*, 2014. **58**: p. 52-58.
57. Huang, Z.-F., et al., Synergetic promotion on photoactivity and stability of W18O₄₉/TiO₂ hybrid. *Applied Catalysis B: Environmental*, 2014. **147**: p. 167-174.
58. Ibadon, A.O. and P. Fitzpatrick, *Heterogeneous Photocatalysis: Recent Advances and Applications*. *Catalysts*, 2013. **3**(1).
59. Cao, Y.Q., et al., TiO_xN_y Modified TiO₂ Powders Prepared by Plasma Enhanced Atomic Layer Deposition for Highly Visible Light Photocatalysis. *Sci Rep*, 2018. **8**(1): p. 12131.
60. Kim, T.H., et al., A Novel Synthetic Method for N Doped TiO₂ Nanoparticles Through Plasma-Assisted Electrolysis and Photocatalytic Activity in the Visible Region. *Frontiers in Chemistry*, 2018. **6**: p. 458.
61. Pitchaimuthu, S., et al., Solution Plasma Process-Derived Defect-Induced Heterophase Anatase/Brookite TiO₂ Nanocrystals for Enhanced Gaseous Photocatalytic Performance. *ACS omega*, 2018. **3**(1): p. 898-905.
62. Lang, X., X. Chen, and J. Zhao, Heterogeneous visible light photocatalysis for selective organic transformations. *Chemical Society Reviews*, 2014. **43**(1): p. 473-486.
63. Wetchakun, K., N. Wetchakun, and S. Sakulsermsuk, An overview of solar/visible light-driven heterogeneous photocatalysis for water purification: TiO₂- and ZnO-based photocatalysts used in suspension photoreactors. *Journal of Industrial and Engineering Chemistry*, 2019. **71**: p. 19-49.
64. Zhou, C., et al., Semiconductor/boron nitride composites: Synthesis, properties, and photocatalysis applications. *Applied Catalysis B: Environmental*, 2018. **238**: p. 6-18.
65. Duan, L., et al., Efficient Photocatalytic PFOA Degradation over Boron Nitride. *Environmental Science & Technology Letters*, 2020. **7**(8): p. 613-619.

66. Li, W., et al., Graphene-Analogue Boron Nitride Modified Bismuth Oxyiodide with Increased Visible-Light Photocatalytic Performance. *physica status solidi (a)*, 2018. **215**(18): p. 1800146.
67. Lei, W., et al., Porous boron nitride nanosheets for effective water cleaning. *Nature communications*, 2013. **4**(1): p. 1-7.
68. Jiang, X., et al., Cu Nanoparticles Supported on Oxygen-Rich Boron Nitride for the Reduction of 4-Nitrophenol. *ACS Applied Nano Materials*, 2018. **1**(12): p. 6692-6700.
69. Fu, X., et al., The role of ball milled h-BN in the enhanced photocatalytic activity: A study based on the model of ZnO. *Applied Surface Science*, 2013. **280**: p. 828-835.
70. Sheng, Y., et al., Sol-gel synthesized hexagonal boron nitride/titania nanocomposites with enhanced photocatalytic activity. *Applied Surface Science*, 2019. **465**: p. 154-163.
71. Wang, N., et al., Visible Light-Responsive Photocatalytic Activity of Boron Nitride Incorporated Composites. *Frontiers in Chemistry*, 2018. **6**: p. 440.
72. Liu, D., et al., A novel TiO₂-xN_x/BN composite photocatalyst: Synthesis, characterization and enhanced photocatalytic activity for Rhodamine B degradation under visible light. *Catalysis Communications*, 2014. **57**: p. 9-13.
73. Li, W., et al., Synthesis and characterization of BN/Bi₂WO₆ composite photocatalysts with enhanced visible-light photocatalytic activity. *RSC Advances*, 2015. **5**(108): p. 88832-88840.
74. Zhang, Q., et al., Bisphenol S-doped g-C₃N₄ nanosheets modified by boron nitride quantum dots as efficient visible-light-driven photocatalysts for degradation of sulfamethazine. *Chemical Engineering Journal*, 2021. **405**: p. 126661.
75. Lei, Z., et al., Facile preparation and multifunctional applications of boron nitride quantum dots. *Nanoscale*, 2015. **7**(45): p. 18902-18907.
76. Yang, K., et al., Innovative Dual-Emitting Ratiometric Fluorescence Sensor for Tetracyclines Detection Based on Boron Nitride Quantum Dots and Europium Ions. *ACS Sustainable Chemistry & Engineering*, 2020. **8**(46): p. 17185-17193.
77. Wang, J., et al., In situ preparation of p-n BiOI@Bi₅O₇I heterojunction for enhanced PFOA photocatalytic degradation under simulated solar light irradiation. *Chemical Engineering Journal*, 2020. **391**: p. 123530.
78. Li, T., et al., Highly efficient photocatalytic degradation toward perfluorooctanoic acid by bromine doped BiOI with high exposure of (001) facet. *Applied Catalysis B: Environmental*, 2020. **268**: p. 118442.
79. Hsu, C.-L., et al., Green synthesis of catalytic gold/bismuth oxyiodide nanocomposites with oxygen vacancies for treatment of bacterial infections. *Nanoscale*, 2018. **10**(25): p. 11808-11819.
80. Liu, G., et al., Band-structure-controlled BiO(ClBr)_(1-x)/2I_x solid solutions for visible-light photocatalysis. *Journal of Materials Chemistry A*, 2015. **3**(15): p. 8123-8132.
81. Xiao, X., et al., Oxygen-rich bismuth oxyhalides: generalized one-pot synthesis, band structures and visible-light photocatalytic properties. *Journal of Materials Chemistry*, 2012. **22**(43): p. 22840-22843.

82. Huang, Y., et al., Oxygen Vacancy Induced Bismuth Oxyiodide with Remarkably Increased Visible-Light Absorption and Superior Photocatalytic Performance. *ACS Applied Materials & Interfaces*, 2014. **6**(24): p. 22920-22927.
83. Neyts, E.C., Plasma-Surface Interactions in Plasma Catalysis. *Plasma Chemistry and Plasma Processing*, 2016. **36**(1): p. 185-212.
84. Manoj Kumar Reddy, P., et al., Degradation and mineralization of methylene blue by dielectric barrier discharge non-thermal plasma reactor. *Chemical Engineering Journal*, 2013. **217**: p. 41-47.
85. Neyts, E.C. and A. Bogaerts, Understanding plasma catalysis through modelling and simulation—a review. *Journal of Physics D: Applied Physics*, 2014. **47**(22): p. 224010.
86. Whitehead, J.C., Plasma-catalysis: the known knowns, the known unknowns and the unknown unknowns. *Journal of Physics D: Applied Physics*, 2016. **49**(24): p. 243001.
87. Kim, H.-H., et al., Plasma Catalysis for Environmental Treatment and Energy Applications. *Plasma Chemistry and Plasma Processing*, 2016. **36**(1): p. 45-72.
88. Chen, G., et al., Progress in Plasma-Assisted Catalysis for Carbon Dioxide Reduction, in *Plasma Chemistry and Gas Conversion*. 2018, IntechOpen.
89. Snoeckx, R. and A. Bogaerts, Plasma technology – a novel solution for CO₂ conversion? *Chemical Society Reviews*, 2017. **46**(19): p. 5805-5863.
90. Reddy, P.M.K., et al., Mineralization of Phenol in Water by Catalytic Non-Thermal Plasma Reactor—An Eco-Friendly Approach for Wastewater Treatment. *Plasma Processes and Polymers*, 2013. **10**(11): p. 1010-1017.
91. Shang, K., et al., Degradation of p-nitrophenol by DBD plasma/Fe²⁺/persulfate oxidation process. *Separation and Purification Technology*, 2019. **218**: p. 106-112.
92. Benetoli, L.O.d.B., et al., Pyrite-enhanced methylene blue degradation in non-thermal plasma water treatment reactor. *Journal of Hazardous Materials*, 2012. **237-238**: p. 55-62.
93. Yan, X., et al., Multi-catalysis of nano-zinc oxide for bisphenol A degradation in a dielectric barrier discharge plasma system: Effect and mechanism. *Separation and Purification Technology*, 2020. **231**: p. 115897.
94. Liu, X., et al., Synergistic degradation of acid orange 7 dye by using non-thermal plasma and g-C(3)N(4)/TiO(2): Performance, degradation pathways and catalytic mechanism. *Chemosphere*, 2020. **249**: p. 126093.
95. Iervolino, G., et al., Degradation of Acid Orange 7 Azo Dye in Aqueous Solution by a Catalytic-Assisted, Non-Thermal Plasma Process. *Catalysts*, 2020. **10**(8).
96. Nian, P., et al., Aqueous methylparaben degradation by dielectric barrier discharge induced non-thermal plasma combined with ZnO-rGO nanosheets. *Separation and Purification Technology*, 2019. **211**: p. 832-842.
97. Pandiyaraj, K.N., et al., Dye wastewater degradation by the synergetic effect of an atmospheric pressure plasma treatment and the photocatalytic activity of plasma-functionalized Cu-TiO₂ nanoparticles. *Journal of Hazardous Materials*, 2020: p. 124264.
98. Tarkwa, J.-B., et al., Highly efficient degradation of azo dye Orange G using laterite soil as catalyst under irradiation of non-thermal plasma. *Applied Catalysis B: Environmental*, 2019. **246**: p. 211-220.

99. Younis, S.A., E. Amdeha, and R.A. El-Salamony, Enhanced removal of p-nitrophenol by β -Ga₂O₃-TiO₂ photocatalyst immobilized onto rice straw-based SiO₂ via factorial optimization of the synergy between adsorption and photocatalysis. *Journal of Environmental Chemical Engineering*, 2021. **9**(1): p. 104619.
100. Zeng, L., et al., Novel visible light enhanced Pyrite-Fenton system toward ultrarapid oxidation of p-nitrophenol: Catalytic activity, characterization and mechanism. *Chemosphere*, 2019. **228**: p. 232-240.
101. Truong, T.K., et al., Insight into the degradation of p-nitrophenol by visible-light-induced activation of peroxydisulfate over Ag/ZnO heterojunction. *Chemosphere*, 2021. **268**: p. 129291.
102. Muersha, W. and G.S. Pozan Soylu, Effects of metal oxide semiconductors on the photocatalytic degradation of 4-nitrophenol. *Journal of Molecular Structure*, 2018. **1174**: p. 96-102.
103. Li, M., et al., Aerobic biodegradation of p-nitrophenol in a nitrifying sludge bioreactor: System performance, sludge property and microbial community shift. *Journal of Environmental Management*, 2020. **265**: p. 110542.
104. Hashimi, A.S., et al., Rapid Catalytic Reduction of 4-Nitrophenol and Clock Reaction of Methylene Blue using Copper Nanowires. *Nanomaterials (Basel, Switzerland)*, 2019. **9**(7): p. 936.
105. Kudlek, E., Decomposition of contaminants of emerging concern in advanced oxidation processes. *Water*, 2018. **10**(7): p. 955.
106. Stefan, M.I., *Advanced oxidation processes for water treatment: fundamentals and applications*. 2017: IWA publishing.
107. Ishchenko, O.M., et al., TiO₂-and ZnO-based materials for photocatalysis: material properties, device architecture and emerging concepts. *Semiconductor Photocatalysis-Materials, Mechanisms and Applications*, 2016: p. 3-30.
108. Pant, B., et al., Synthesis and Characterization of ZnO-TiO₂/Carbon Fiber Composite with Enhanced Photocatalytic Properties. *Nanomaterials (Basel)*, 2020. **10**(10).
109. Chang, C.-J., et al., AgI-BiOI-graphene composite photocatalysts with enhanced interfacial charge transfer and photocatalytic H₂ production activity. *Applied Surface Science*, 2019. **469**: p. 703-712.
110. Yosefi, L. and M. Haghghi, Fabrication of nanostructured flowerlike p-BiOI/p-NiO heterostructure and its efficient photocatalytic performance in water treatment under visible-light irradiation. *Applied Catalysis B: Environmental*, 2018. **220**: p. 367-378.
111. Arthur, R.B., J.C. Ahern, and H.H. Patterson, Application of BiOX Photocatalysts in Remediation of Persistent Organic Pollutants. *Catalysts*, 2018. **8**(12).
112. Wang, X., et al., Iodine-Deficient BiOI Nanosheets with Lowered Valence Band Maximum To Enable Visible Light Photocatalytic Activity. *ACS Sustainable Chemistry & Engineering*, 2019. **7**(8): p. 7900-7907.
113. Contreras, D., et al., Selective oxidation of cyclohexane to cyclohexanol by BiOI under visible light: Role of the ratio (1 1 0)/(0 0 1) facet. *Applied Catalysis B: Environmental*, 2019. **251**: p. 17-24.
114. Sharma, K., et al., Recent advances in enhanced photocatalytic activity of bismuth oxyhalides for efficient photocatalysis of organic pollutants in water: A review. *Journal of Industrial and Engineering Chemistry*, 2019. **78**: p. 1-20.

115. Ye, L., et al., Recent advances in BiOX (X= Cl, Br and I) photocatalysts: synthesis, modification, facet effects and mechanisms. *Environmental Science: Nano*, 2014. **1**(2): p. 90-112.
116. Meng, S., et al., Room-temperature fabrication of bismuth oxybromide/oxyiodide photocatalyst and efficient degradation of phenolic pollutants under visible light. *Journal of hazardous materials*, 2018. **358**: p. 20-32.
117. Song, Z., et al., Efficient photocatalytic defluorination of perfluorooctanoic acid over BiOCl nanosheets via a hole direct oxidation mechanism. *Chemical Engineering Journal*, 2017. **317**: p. 925-934.
118. Song, Z., et al., Improved photocatalytic degradation of perfluorooctanoic acid on oxygen vacancies-tunable bismuth oxychloride nanosheets prepared by a facile hydrolysis. *Journal of hazardous materials*, 2019. **377**: p. 371-380.
119. Xu, T., et al., Enhanced photocatalytic degradation of perfluorooctanoic acid using carbon-modified bismuth phosphate composite: Effectiveness, material synergy and roles of carbon. *Chemical Engineering Journal*, 2020. **395**: p. 124991.
120. Jiang, W., et al., Enhanced visible-light-induced photocatalytic degradation of tetracycline using BiOI/MIL-125 (Ti) composite photocatalyst. *Journal of Alloys and Compounds*, 2021. **854**: p. 157166.
121. Wang, J., et al., Decomposition of highly persistent perfluorooctanoic acid by hollow Bi/BiOI_{1-x}F_x: Synergistic effects of surface plasmon resonance and modified band structures. *Journal of Hazardous Materials*, 2021. **402**: p. 123459.
122. Yang, Y., et al., Construction of iodine vacancy-rich BiOI/Ag@AgI Z-scheme heterojunction photocatalysts for visible-light-driven tetracycline degradation: Transformation pathways and mechanism insight. *Chemical Engineering Journal*, 2018. **349**: p. 808-821.
123. Zhong, S., et al., Rationally designed a g-C₃N₄/BiOI/Bi₂O₂CO₃ composite with promoted photocatalytic activity. *Journal of Alloys and Compounds*, 2021. **853**: p. 157307.
124. Guo, Y., et al., Enhanced photoactivity and oxidizing ability simultaneously via internal electric field and valence band position by crystal structure of bismuth oxyiodide. *Applied Catalysis B: Environmental*, 2020. **262**: p. 118262.
125. Di, J., et al., Carbon quantum dots in situ coupling to bismuth oxyiodide via reactable ionic liquid with enhanced photocatalytic molecular oxygen activation performance. *Carbon*, 2016. **98**: p. 613-623.
126. Mohanta, M.K., et al., Hexagonal Boron Nitride Quantum Dots as a Superior Hole Extractor for Efficient Charge Separation in WO₃-Based Photoelectrochemical Water Oxidation. *ACS Applied Energy Materials*, 2019. **2**(10): p. 7457-7466.
127. Guo, W., et al., Boron nitride quantum dots loading red phosphorus for efficient visible-light-driven photocatalytic degradation of organic pollutants. *Journal of Materials Science: Materials in Electronics*, 2021.
128. Yang, Y., et al., Boron nitride quantum dots decorated ultrathin porous g-C₃N₄: Intensified exciton dissociation and charge transfer for promoting visible-light-driven molecular oxygen activation. *Applied Catalysis B: Environmental*, 2019. **245**: p. 87-99.

129. Jerome, R. and A.K. Sundramoorthy, Hydrothermal synthesis of boron nitride quantum dots/poly (luminol) nanocomposite for selective detection of ascorbic acid. *Journal of The Electrochemical Society*, 2019. **166**(9): p. B3017.
130. Thangasamy, P., M. Santhanam, and M. Sathish, Supercritical Fluid Facilitated Disintegration of Hexagonal Boron Nitride Nanosheets to Quantum Dots and Its Application in Cells Imaging. *ACS Applied Materials & Interfaces*, 2016. **8**(29): p. 18647-18651.
131. Lin, L., et al., Fabrication and Luminescence of Monolayered Boron Nitride Quantum Dots. *Small*, 2014. **10**(1): p. 60-65.
132. Liu, D., et al., Graphene-analogue BN-modified microspherical BiOI photocatalysts driven by visible light. *Dalton Transactions*, 2016. **45**(6): p. 2505-2516.
133. Jung, J.-H., et al., Defect engineering route to boron nitride quantum dots and edge-hydroxylated functionalization for bio-imaging. *RSC Advances*, 2016. **6**(77): p. 73939-73946.
134. Bai, J., et al., Enhancement of Solar-Driven Photocatalytic Activity of BiOI Nanosheets through Predominant Exposed High Energy Facets and Vacancy Engineering. *Small*, 2020. **16**(5): p. 1904783.
135. Asadzadeh-Khaneghah, S., A. Habibi-Yangjeh, and D. Seifzadeh, Graphitic carbon nitride nanosheets coupled with carbon dots and BiOI nanoparticles: boosting visible-light-driven photocatalytic activity. *Journal of the Taiwan Institute of Chemical Engineers*, 2018. **87**: p. 98-111.
136. Ahmad, P., et al., Fabrication of hexagonal boron nitride quantum dots via a facile bottom-up technique. *Ceramics International*, 2019. **45**(17): p. 22765-22768.
137. Wang, X., et al., Hydroxyl-regulated BiOI nanosheets with a highly positive valence band maximum for improved visible-light photocatalytic performance. *Applied Catalysis B: Environmental*, 2020. **268**: p. 118390.
138. Yola, M.L. and N. Atar, A novel detection approach for serotonin by graphene quantum dots/two-dimensional (2D) hexagonal boron nitride nanosheets with molecularly imprinted polymer. *Applied Surface Science*, 2018. **458**: p. 648-655.
139. Yola, M.L., Electrochemical activity enhancement of monodisperse boron nitride quantum dots on graphene oxide: Its application for simultaneous detection of organophosphate pesticides in real samples. *Journal of Molecular Liquids*, 2019. **277**: p. 50-57.
140. Liu, B., et al., One-step synthesis of boron nitride quantum dots: simple chemistry meets delicate nanotechnology. *Chem. Eur. J*, 2016. **22**: p. 18899-18907.
141. Li, W., et al., Carbon-quantum-dots-loaded ruthenium nanoparticles as an efficient electrocatalyst for hydrogen production in alkaline media. *Advanced Materials*, 2018. **30**(31): p. 1800676.
142. Saleh, D.A. and A. Sosnik, Enhanced photoluminescence of boron nitride quantum dots by encapsulation within polymeric nanoparticles. *Nanotechnology*, 2021. **32**(19): p. 195104.
143. Ma, N., et al., In situ synthesis of a cadmium sulfide/reduced graphene oxide/bismuth Z-scheme oxyiodide system for enhanced photocatalytic performance in chlorinated paraben degradation. *Chemical Engineering Journal*, 2019. **359**: p. 530-541.

144. Wang, P., et al., One-step synthesis of easy-recycling TiO₂-rGO nanocomposite photocatalysts with enhanced photocatalytic activity. *Applied Catalysis B: Environmental*, 2013. **132-133**: p. 452-459.
145. Jiang, B., et al., Degradation of azo dye using non-thermal plasma advanced oxidation process in a circulatory airtight reactor system. *Chemical Engineering Journal*, 2012. **204**: p. 32-39.
146. Katheresan, V., J. Kannedo, and S.Y. Lau, Efficiency of various recent wastewater dye removal methods: A review. *Journal of Environmental Chemical Engineering*, 2018. **6**(4): p. 4676-4697.
147. Ganzenko, O., et al., Electrochemical advanced oxidation and biological processes for wastewater treatment: a review of the combined approaches. *Environmental Science and Pollution Research*, 2014. **21**(14): p. 8493-8524.
148. Cuerda-Correa, E.M., M.F. Alexandre-Franco, and C. Fernández-González, Advanced Oxidation Processes for the Removal of Antibiotics from Water. An Overview. *Water*, 2020. **12**(1): p. 102.
149. Wu, S. and A. Krosuri, A novel continuous-flow electrohydraulic discharge process for handling high-conductivity wastewaters. *International Journal of Environmental Science and Technology*, 2020. **17**(2): p. 615-624.
150. Bruggeman, P. and C. Leys, Non-thermal plasmas in and in contact with liquids. *Journal of Physics D: Applied Physics*, 2009. **42**(5): p. 053001.
151. Gao, L., et al., Degradation kinetics and mechanism of emerging contaminants in water by dielectric barrier discharge non-thermal plasma: The case of 17 β -Estradiol. *Chemical Engineering Journal*, 2013. **228**: p. 790-798.
152. Tichonovas, M., et al., Degradation of various textile dyes as wastewater pollutants under dielectric barrier discharge plasma treatment. *Chemical Engineering Journal*, 2013. **229**: p. 9-19.
153. Wang, B., et al., Degradation of methylene blue using double-chamber dielectric barrier discharge reactor under different carrier gases. *Chemical Engineering Science*, 2017. **168**: p. 90-100.
154. Czapka, T., I. Maliszewska, and J. Olesiak-Bańska, Influence of Atmospheric Pressure Non-thermal Plasma on Inactivation of Biofilm Cells. *Plasma Chemistry and Plasma Processing*, 2018. **38**(6): p. 1181-1197.
155. Wu, L., et al., Degradation of methylene blue by dielectric barrier discharge plasma coupled with activated carbon supported on polyurethane foam. *RSC Advances*, 2019. **9**(45): p. 25967-25975.
156. Shang, K., J. Li, and R. Morent, Hybrid electric discharge plasma technologies for water decontamination: a short review. *Plasma Science and Technology*, 2019. **21**(4): p. 043001.
157. Bruggeman, P.J., et al., Plasma–liquid interactions: a review and roadmap. *Plasma Sources Science and Technology*, 2016. **25**(5): p. 053002.
158. Vanraes, P., A.Y. Nikiforov, and C. Leys, Electrical discharge in water treatment technology for micropollutant decomposition. *Plasma science and technology—progress in physical states and chemical reactions*, 2016. **429**.
159. Cao, Y., et al., Review on reactive species in water treatment using electrical discharge plasma: formation, measurement, mechanisms and mass transfer. *Plasma Science and Technology*, 2018. **20**(10): p. 103001.

160. Liu, J., et al., Direct synthesis of hydrogen peroxide from plasma-water interactions. *Scientific Reports*, 2016. **6**(1): p. 38454.
161. Magureanu, M., et al., Pulsed Corona Discharge for Degradation of Methylene Blue in Water. *Plasma Chemistry and Plasma Processing*, 2013. **33**(1): p. 51-64.
162. Rauf, M.A., et al., Photocatalytic degradation of Methylene Blue using a mixed catalyst and product analysis by LC/MS. *Chemical Engineering Journal*, 2010. **157**(2): p. 373-378.
163. Li, J., M. Sato, and T. Ohshima, Degradation of phenol in water using a gas-liquid phase pulsed discharge plasma reactor. *Thin Solid Films*, 2007. **515**(9): p. 4283-4288.
164. Magureanu, M., et al., Decomposition of methylene blue in water using a dielectric barrier discharge: optimization of the operating parameters. *Journal of applied physics*, 2008. **104**(10): p. 103306.
165. Huang, F., et al., Analysis of the degradation mechanism of methylene blue by atmospheric pressure dielectric barrier discharge plasma. *Chemical Engineering Journal*, 2010. **162**(1): p. 250-256.
166. Wu, L., et al., Degradation of Methylene Blue via Dielectric Barrier Discharge Plasma Treatment. *Water*, 2019. **11**(9): p. 1818.
167. Xin, L., et al., Degradation of triclosan in aqueous solution by dielectric barrier discharge plasma combined with activated carbon fibers. *Chemosphere*, 2016. **144**: p. 855-863.
168. Groele, J. and J. Foster, Hydrogen Peroxide Interference in Chemical Oxygen Demand Assessments of Plasma Treated Waters. *Plasma*, 2019. **2**(3).
169. Wang, H., R.J. Wandell, and B.R. Locke, The influence of carrier gas on plasma properties and hydrogen peroxide production in a nanosecond pulsed plasma discharge generated in a water-film plasma reactor. *Journal of Physics D: Applied Physics*, 2018. **51**(9): p. 094002.
170. Locke, B.R. and K.-Y. Shih, Review of the methods to form hydrogen peroxide in electrical discharge plasma with liquid water. *Plasma Sources Science and Technology*, 2011. **20**(3): p. 034006.
171. Poulsen, C.J., C. Tabor, and J.D. White, Long-term climate forcing by atmospheric oxygen concentrations. *Science*, 2015. **348**(6240): p. 1238.
172. Peng, P., et al., Plasma in situ gas-liquid nitrogen fixation using concentrated high-intensity electric field. *Journal of Physics D: Applied Physics*, 2019. **52**(49): p. 494001.
173. Thirumdas, R., et al., Plasma activated water (PAW): Chemistry, physico-chemical properties, applications in food and agriculture. *Trends in food science & technology*, 2018. **77**: p. 21-31.
174. Benetoli, L.O.d.B., et al., Effect of temperature on methylene blue decolorization in aqueous medium in electrical discharge plasma reactor. *Journal of the Brazilian Chemical Society*, 2011. **22**: p. 1669-1678.
175. Rezaei, F., et al., Applications of Plasma-Liquid Systems: A Review. *Materials (Basel, Switzerland)*, 2019. **12**(17): p. 2751.
176. García, M.C., et al., Microwave atmospheric pressure plasma jets for wastewater treatment: Degradation of methylene blue as a model dye. *Chemosphere*, 2017. **180**: p. 239-246.

177. Tesema, T.E., et al., Plasmon-Enhanced Resonant Excitation and Demethylation of Methylene Blue. *The Journal of Physical Chemistry C*, 2017. **121**(13): p. 7421-7428.
178. Wang, T.C., et al., Plasma-TiO₂ Catalytic Method for High-Efficiency Remediation of p-Nitrophenol Contaminated Soil in Pulsed Discharge. *Environmental Science & Technology*, 2011. **45**(21): p. 9301-9307.
179. Zhao, C., et al., A microwave atmospheric plasma strategy for fast and efficient degradation of aqueous p-nitrophenol. *Journal of Hazardous Materials*, 2020: p. 124473.
180. Tugba Saka, E. and K. Tekintas, Light driven photodegradation of 4-nitrophenol with novel Co and Cu phthalocyanine in aqueous media. *Journal of Molecular Structure*, 2020. **1215**: p. 128189.
181. Wang, N., et al., New insight into photodegradation mechanisms, kinetics and health effects of p-nitrophenol by ozonation in polluted water. *J Hazard Mater*, 2021. **403**: p. 123805.
182. Borges, K.A., et al., Characterization of a highly efficient N-doped TiO₂ photocatalyst prepared via factorial design. *New Journal of Chemistry*, 2016. **40**(9): p. 7846-7855.
183. Krosuri, A., et al., Efficient degradation and mineralization of methylene blue via continuous-flow electrohydraulic plasma discharge. *Journal of Water Process Engineering*, 2021. **40**: p. 101926.
184. De Coninck, J., et al., Factorial designs: an efficient approach to choosing the main factors influencing growth and hydrolase production by *Tetrahymena thermophila*. *Journal of Industrial Microbiology and Biotechnology*, 2004. **31**(5): p. 204-208.
185. Wu, S., et al., Optimization of a novel liquid-phase plasma discharge process for continuous production of biodiesel. *Journal of Cleaner Production*, 2019. **228**: p. 405-417.
186. Wu, S. and A. Krosuri, Removing methylene blue contained in dye wastewater using a novel liquid-phase plasma discharge process. *Journal of Environmental Science and Health, Part A*, 2020. **55**(8): p. 1032-1039.
187. Hamdan, A., J.-L. Liu, and M.S. Cha, Microwave Plasma Jet in Water: Characterization and Feasibility to Wastewater Treatment. *Plasma Chemistry and Plasma Processing*, 2018. **38**(5): p. 1003-1020.
188. Chandana, L. and C. Subrahmanyam, Degradation and mineralization of aqueous phenol by an atmospheric pressure catalytic plasma reactor. *Journal of Environmental Chemical Engineering*, 2018. **6**(3): p. 3780-3786.
189. Pandiyaraj, K.N., et al., Evaluation of influence of cold atmospheric pressure argon plasma operating parameters on degradation of aqueous solution of Reactive Blue 198 (RB-198). *Plasma Science and Technology*, 2020. **22**(5): p. 055504.
190. Lamichhane, P., et al., Control of hydrogen peroxide production in plasma activated water by utilizing nitrification. *Journal of Physics D: Applied Physics*, 2019. **52**(26): p. 265206.
191. Joshi, A.A., et al., Formation of hydroxyl radicals, hydrogen peroxide and aqueous electrons by pulsed streamer corona discharge in aqueous solution. *Journal of Hazardous Materials*, 1995. **41**(1): p. 3-30.
192. Malik, M.A., A. Ghaffar, and S.A. Malik, Water purification by electrical discharges. *Plasma Sources Science and Technology*, 2001. **10**(1): p. 82-91.

193. Navaneetha Pandiyaraj, K., et al., Evaluation of influence of cold atmospheric pressure argon plasma operating parameters on degradation of aqueous solution of Reactive Blue 198 (RB-198). *Plasma Science and Technology*, 2020. **22**(5): p. 055504.
194. Wang, T., et al., Organic acids enhanced decoloration of azo dye in gas phase surface discharge plasma system. *Journal of Hazardous Materials*, 2016. **302**: p. 65-71.
195. Zheng, H., et al., p-Nitrophenol Enhanced Degradation in High-Voltage Pulsed Corona Discharges Combined with Ozone System. *Plasma Chemistry and Plasma Processing*, 2013. **33**(6): p. 1053-1062.
196. Di Paola, A., et al., Heterogeneous photocatalytic degradation of nitrophenols. *Journal of Photochemistry and Photobiology A: Chemistry*, 2003. **155**(1): p. 207-214.
197. Wang, T., et al., Evaluation of the potential of p-nitrophenol degradation in dredged sediment by pulsed discharge plasma. *Water Research*, 2015. **84**: p. 18-24.
198. Sun, S.-P. and A.T. Lemley, p-Nitrophenol degradation by a heterogeneous Fenton-like reaction on nano-magnetite: Process optimization, kinetics, and degradation pathways. *Journal of Molecular Catalysis A: Chemical*, 2011. **349**(1): p. 71-79.
199. Li, J., et al., Degradation of p-nitrophenol by Fe⁰/H₂O₂/persulfate system: Optimization, performance and mechanisms. *Journal of the Taiwan Institute of Chemical Engineers*, 2017. **80**: p. 686-694.
200. Kitagawa, W., N. Kimura, and Y. Kamagata, A novel p-nitrophenol degradation gene cluster from a gram-positive bacterium, *Rhodococcus opacus* SAO101. *Journal of bacteriology*, 2004. **186**(15): p. 4894-4902.
201. Yu, S., J. Hu, and J. Wang, Gamma radiation-induced degradation of p-nitrophenol (PNP) in the presence of hydrogen peroxide (H₂O₂) in aqueous solution. *Journal of Hazardous Materials*, 2010. **177**(1): p. 1061-1067.
202. Mishra, K.P. and P.R. Gogate, Intensification of sonophotocatalytic degradation of p-nitrophenol at pilot scale capacity. *Ultrasonics Sonochemistry*, 2011. **18**(3): p. 739-744.
203. Samuel, M.S., A. Sivaramakrishna, and A. Mehta, Bioremediation of p-Nitrophenol by *Pseudomonas putida* 1274 strain. *Journal of Environmental Health Science and Engineering*, 2014. **12**(1): p. 53.
204. Oturan, M.A. and J.-J. Aaron, Advanced oxidation processes in water/wastewater treatment: principles and applications. A review. *Critical Reviews in Environmental Science and Technology*, 2014. **44**(23): p. 2577-2641.
205. Li, J., et al., Heterogeneous catalytic oxidation for the degradation of p-nitrophenol in aqueous solution by persulfate activated with CuFe₂O₄ magnetic nano-particles. *Chemical Engineering Journal*, 2017. **324**: p. 63-73.
206. Stratton, G.R., et al., Plasma-Based Water Treatment: Efficient Transformation of Perfluoroalkyl Substances in Prepared Solutions and Contaminated Groundwater. *Environmental Science & Technology*, 2017. **51**(3): p. 1643-1648.
207. Saleem, M., et al., Comparative performance assessment of plasma reactors for the treatment of PFOA; reactor design, kinetics, mineralization and energy yield. *Chemical Engineering Journal*, 2020. **382**: p. 123031.
208. Singh, R.K., et al., Breakdown Products from Perfluorinated Alkyl Substances (PFAS) Degradation in a Plasma-Based Water Treatment Process. *Environmental Science & Technology*, 2019. **53**(5): p. 2731-2738.

209. Lewis, A.J., et al., Rapid degradation of PFAS in aqueous solutions by reverse vortex flow gliding arc plasma. *Environmental Science: Water Research & Technology*, 2020. **6**(4): p. 1044-1057.
210. Radhika, N.P., et al., Recent advances in nano-photocatalysts for organic synthesis. *Arabian Journal of Chemistry*, 2019. **12**(8): p. 4550-4578.
211. Jiao, H.-P., et al., One-pot synthesis of heterostructured Bi₂S₃/BiOBr microspheres with highly efficient visible light photocatalytic performance. *RSC Advances*, 2015. **5**(21): p. 16239-16249.
212. Guo, H., et al., Degradation of antibiotic chloramphenicol in water by pulsed discharge plasma combined with TiO₂/WO₃ composites: mechanism and degradation pathway. (1873-3336 (Electronic)).
213. Guo, H., et al., Degradation of flumequine in water by pulsed discharge plasma coupled with reduced graphene oxide/TiO₂ nanocomposites. *Separation and Purification Technology*, 2019. **218**: p. 206-216.
214. Guo, H., et al., Multi-catalysis induced by pulsed discharge plasma coupled with graphene-Fe₃O₄ nanocomposites for efficient removal of ofloxacin in water: Mechanism, degradation pathway and potential toxicity. *Chemosphere*, 2021. **265**: p. 129089.
215. Cubas, A.L.V., et al., Effect of chemical species generated by different geometries of air and argon non-thermal plasma reactors on bacteria inactivation in water. *Separation and Purification Technology*, 2019. **222**: p. 68-74.
216. Katal, R., M.H. Davood Abadi Farahani, and H. Jiangyong, Degradation of acetaminophen in a photocatalytic (batch and continuous system) and photoelectrocatalytic process by application of faceted-TiO₂. *Separation and Purification Technology*, 2020. **230**: p. 115859.
217. Lukes, P. and B.R. Locke, Degradation of Substituted Phenols in a Hybrid Gas-Liquid Electrical Discharge Reactor. *Industrial & Engineering Chemistry Research*, 2005. **44**(9): p. 2921-2930.